LOW FREQUENCY ACOUSTIC INTERACTIONS

IN SUPERCONDUCTORS

By

GARY WAYNE GOODRICH

Bachelor of Science
University of Texas
Austin, Texas
1966

Bachelor of Arts
University of Texas
Austin, Texas
1966

Master of Science
Oklahoma State University
Stillwater, Oklahoma
1968

Submitted to the Faculty of the Graduate College
of the Oklahoma State University
in partial fulfillment of the requirements
for the Degree of
DOCTOR OF PHILOSOPHY
May, 1971

LOW FREQUENCY ACOUSTIC INTERACTIONS

IN SUPERCONDUCTORS

Thesis Approved:

James Lange
Thesis Adviser

J. Paul Hershey

E. F. Thurber

D. D. Dunham
Dean of the Graduate College

ACKNOWLEDGMENTS

The author is grateful to the National Science Foundation for financial support during this investigation. The guidance, assistance, and discussion time of Professor James Lange is appreciated. Also, Professors Elton Kohnke, George Thurston, and Thomas Winter contributed by lending equipment necessary to conduct this investigation. The physics and chemistry instrument shop and the glass shop were very helpful in the design and construction of the experimental apparatus. The assistance, encouragement, and understanding of my wife, Patti, is appreciated.

TABLE OF CONTENTS

Chapter		Page
I.	INTRODUCTION	1
	Scope of Study	1
	Materials	2
	History of Superconductivity	4
II.	THEORETICAL BACKGROUND	8
	Elasticity	8
	Normal State Theory	12
	Superconductivity	14
	Dislocation Theory	18
III.	APPARATUS	22
	Types of Measurement	22
	Longitudinal Mode	23
	Torsional Mode	31
	Other Apparatus and Measurements	40
IV.	RESULTS AND DISCUSSION	44
	Normal State	44
	Superconducting State	57
	Resistivity	78
	Alloys	86
V.	CONCLUSIONS	91
	Normal State Behavior	91
	Superconducting State Behavior	91
	Suggestions for Further Work	94
BIBLIOGRAPHY		97
APPENDIX A.	COMPUTER PROGRAMS	105
APPENDIX B.	SYMBOLS	114

LIST OF TABLES

Table		Page
I.	Material Properties.	3
II.	Single Crystal Elastic Constants of Nb	10
III.	Modulus Coefficient of Longitudinal B^2 Term.	46
IV.	Loss Factor Coefficient of Longitudinal B^2 Term.	50
V.	Modulus Coefficient of Torsional B^2 Term	50
VI.	Loss Factor Coefficient of Torsional B^2 Term	53
VII.	Features of Longitudinal Mode of Type II Materials	64
VIII.	Features of Torsional Mode of Type II Materials.	73
IX.	Comparison of Resistivity Data	83
X.	Least-Squares-Fit Program.	106
XI.	Vortex Interactions Program.	108
XII.	Data Reduction Program	111
XIII.	Symbols.	114

LIST OF FIGURES

Figure		Page
1.	Sample Mount.	24
2.	Block Diagram of Apparatus.	26
3.	Change in Elasticity as a Function of H	28
4.	Elasticity at $3f_o$	29
5.	Effect of Electrode Separation.	32
6.	Torsional Drives.	35
7.	Effect of Removing Mass From End of Sample.	37
8.	Effect of Removing Mass Along Length of Sample.	38
9.	Torsional-Drive Fit to H^2	39
10.	Longitudinal Modulus Changes.	45
11.	Longitudinal Loss Factor Changes.	47
12.	Torsional Modulus Changes	49
13.	Torsional Loss Factor Changes	52
14.	Dislocation Lobes Originally.	54
15.	Dislocation Lobes After Deformation	55
16.	Magnetization at the Superconducting Transition	58
17.	Type I Longitudinal Modulus Transition.	60
18.	Internal Friction Peak.	61
19.	Type II Longitudinal Modulus Transition	62
20.	Decreasing Loss Factor Above H_{c2}.	66
21.	Total Modulus Change Versus Conductivity.	67
22.	The Electronic Transition	69

LIST OF FIGURES (Continued)

Figure		Page
23.	Type I Torsional Modulus Transition.	70
24.	Type II Torsional Modulus Transition	72
25.	Number of Vortices in the Mixed State for Nb	75
26.	Dislocation Effect in the Loss Factor.	77
27.	Amplitude Dependence of Loss Factor.	79
28.	Fluctuation Effect as a Function of Deformation.	80
29.	Longitudinal Dislocation Effect.	81
30.	Resistivity at $4^{\circ}K$	82
31.	Magnetoresistance.	84
32.	Resistivity Versus Temperature	85
33.	Resistivity of Alloys.	87
34.	Alloy Sound Velocities	88
35.	Pb Transition.	90
36.	Magnetic Fluctuations.	93
37.	Ferromagnetic Saturation of Ni	96
38.	Fractional Change in Size of Vortex Versus Separation. .	113
39.	Expansion of Vortices in Mixed State	113
40.	Number of Vortices in Mixed State.	113

CHAPTER I

INTRODUCTION

Scope of Study

The Bardeen-Cooper-Schrieffer (BCS) microscopic theory[1] of superconductivity has given an excellent explanation of the electronic properties of Type I superconductivity, but no single coherent theory exists for superconductors of the second kind. Thus, much effort has been put forth to better understand the Type II occurrence of superconductivity. It was the scope of this work to use acoustical measurement techniques to observe the transition from the superconducting state to the normal state of both Type I and Type II materials, comparing and contrasting as similiarities and differences appeared. Parameters such as the moduli of elasticity, the acoustic attenuation or loss factor, and the magnetization were used to study the vortex or mixed state during the superconducting transition. The mixed state was observed by studying the magnetic field dependence of the elastic moduli of a superconducting material below its critical temperature. To better understand the superconducting state, a detailed study of the normal state magnetic field dependence was necessary. This normal state field dependence served as a reference point for the superconducting data. A better description of the magnetic field effects on the elasticity, attenuation, and dislocation motion in Type II materials was sought.

Materials Investigated

Only two pure elements exhibit Type II superconductivity: Nb and V. For comparison with a better understood Type I material, Ta was studied along with the Type II materials. Nb, V, and Ta are all body-centered-cubic (b.c.c.) crystals and are found in the same column in the periodic table. Impurities generally cause Type I materials to become Type II, and only recently has Ta been sufficiently purified to exhibit Type I behavior.[2,3] B.c.c. crystals exhibit a principle slip direction along the (111) direction[4] and the effects of dislocations in samples with this orientation was investigated. Materials with high acoustic quality factors (Q), or high ratios of energy stored per cycle to energy lost per cycle, were necessary to allow sufficient accuracy in the elastic measurement for observing the small changes in the elastic moduli at the superconducting transition. The fractional change in volume at the transition has been shown to be considerably smaller than the fractional change in the elastic constants, so that no correction is made for the volume effect.[5-7] Nb, V, and Ta have been the subject of many superconducting investigations and have been used in pure and alloy form in commercial applications.[8] The purity of the samples is indicated directly by the residual resistance ratio (RRR), the ratio of resistivity at room temperature to that at $4^{\circ}K$. The electronic mean free path (ℓ) is the average distance an electron travels between collisions in a crystal and can be calculated by knowledge of the conductivity and Fermi velocity. Table I gives the pertinent material properties for the samples studied in this investigation and the measured elastic constants, Young's modulus (Y) and the modulus of rigidity (μ).

TABLE I

MATERIAL PROPERTIES

Sample	RRR	$\rho(4^{\circ}K)$ ($\mu\,\Omega$ cm)	$\ell(4^{\circ}K)$ (10^{-5} cm)	$v_2(77^{\circ}K)$ (10^5 cm/sec)	$v_3(77^{\circ}K)$ (10^5 cm/sec)	p (gm/cm^3)	$Y(77^{\circ}K)$ (10^{11} dynes/cm^2)	$\mu(77^{\circ}K)$ (10^{11} dynes/cm^2)
Nb (100) #1	30	0.64	1.58	4.10	2.12	8.76	----	----
Nb (110) #2	86	0.17	5.83	4.16	----	8.76	----	----
Nb (111) #4	55	0.34	2.98	4.75	2.36	8.76	----	----
Nb (100) #5	2500	0.0063	163.	4.41	2.01	8.76	----	----
Nb (111) #6	2500	0.0075	136.	3.57	2.38	8.76	----	----
Nb (poly) #1	47	0.33	3.05	3.38	2.37	8.76	10.1	4.88
Nb (poly) #4	31	0.55	1.86	4.01	2.05	8.76	14.1	3.69
V (poly) #1	17	1.33	.619	4.81	2.85	6.02	14.0	4.95
Ta (poly)	20	0.75	1.41	3.32	2.16	16.6	18.3	7.73
Ta (100)	147	0.96	1.11	3.18	1.66	16.6	----	----

History of Superconductivity

Superconductivity was discovered in 1911 by Kamerlingh-Onnes,[9,10] while studying the low temperature resistivity of mercury, some three years after he first liquified helium. The resistivity of mercury suddenly dropped below the measuring capability of his apparatus and was believed to be zero below a certain critical temperature. The next significant step in the understanding of superconductivity was in 1932 when Keesom, et al.[11,12] observed a discontinuous jump in the electronic specific heat at the superconducting critical temperature, T_c. Meissner and Ochsenfeld[13] realized that a superconductor exhibited perfect diamagnetism, i.e., inside a superconductor there exists total magnetic flux expulsion for low magnetic fields. At the critical magnetic field superconductivity is destroyed and the normal resistance is regained.

Keesom, Rutgers, and Gorter[14-17] applied classical thermodynamics to the superconducting transition and were able to explain some of the experimental anomalies. A phenomenological explanation of the second order phase transition at T_c was proposed by Gorter and Casmir[18,19] via a two-fluid model in analogy with superfluidity. Mendelssohm[20] proposed a sponge model of superconducting and normal regions to explain superconductivity. The superconducting sponge shorted all of the normal regions and caused zero electrical resistivity in the bulk sample.

H. and F. London[21,22] put forth a phenomenological theory to explain the electromagnetic properties of superconductors. They proposed that an external magnetic field would penetrate into a superconductor only a small distance, λ. Thus, a thin surface sheath around the superconductor did contain a reduced magnetic field and, therefore, a small elec-

trical resistance. The superconducting state can be pictured as a distinct thermodynamic phase below a critical temperature, T_c, a critical field, H_c, and a critical current density, J_c. A plot of T_c, H_c, and J_c yields a superconducting ellipsoid centered at the origin and surrounded by the normal state. F. London[23] made the first microscopic attempt to explain the diamagnetic properties by use of quantum mechanics. Measurements[24-27] of the magnetization and penetration depth were done by Pontius on thin Pb wires, by Shoenberg on mercury colloids, by Lock on thin films, and by Laurmann and Shoenberg on bulk materials.

Landau and London's[28,29] laminar structure for the intermediate state of Type I superconductors gave a new insight into a model for explaining many of the experimental facts. The model proposed was one of alternate layers of superconducting and normal layers of volumes proportional to the amount of total material in the respective states. This model was experimentally confirmed by Meshkovsky and Shalnikov.[30,31] Other methods for the direct observation[32,33] of the lamina further confirmed this model. Surface resistance measurements at microwave frequencies by H. London and A. Pippard[34,35] showed that the change in surface resistance at the critical temperature was not discontinuous.

A phenomenological extension of the London theory by Ginzberg and Landau[36] revealed the importance of the boundary energies between normal and superconducting phases in determining a model for the types of superconductors. Positive surface energies at phase boundaries cause lamina as in Type I materials, and negative surface energies imply a cylindrical vortex model[37,38] for Type II materials.

The discovery of the isotope effect by Maxwell[39] gave a first insight into the dependence of the critical temperature on isotopic mass.

The lighter isotopes had higher critical temperatures. However, no explanation of what limits the critical temperature to less than $20^{\circ}K$[40] has been found.

A start on a microscopic explanation of the isotope effect was begun by Frohlich and Bardeen[41,42] by considering the electron-phonon interaction. The spatial coherence introduced by Pippard[43] connected any local perturbation of the superconducting order parameter caused by the magnetic field to a spreading out over a distance of the order of ξ, the range of coherence, from the center of the disturbance. Pippard[44] further showed the relation of ξ to λ determined the sign of the surface energy and, thus, the type of superconductivity. $\xi > \lambda$ implied a positive surface energy and Type I behavior. $\xi < \lambda$ implied a negative surface energy and Type II behavior. Bardeen[45] showed that the coherence length concept implied an energy gap model for superconductors. Much experimental evidence[46] of an energy gap was found by 1958. Meanwhile, Matthias[47] had demonstrated that many alloys exhibited Type II properties with Nb and V remaining as the only two pure metals that exhibit a Type II behavior.

Cooper's[48] proof of the existence of a possible attractive interaction in the Fermi sea aroused more interest in a microscopic explanation. Finally, in 1957 many years after the discovery of superconductivity, a microscopic theory was derived by Bardeen, Cooper, and Schrieffer.[1] The BCS wavefunction utilized a quasi-particle (boson-like) composed of two electrons (fermions), coupled through opposite momenta and spin. The BCS theory predicted generally all of the observed phenomena of Type I materials. The BCS theory is not completely acceptable in explaining Type II behaviors. Boguliubov, et. al.[49] showed that

Bose-Einstein statistics could be applied and the BCS results obtained. Suggestions of a similar pairing of Fermi particles to form quasi-bosons have been made for nucleii[50] and elementary particles.[51]

Among the predictions of the BCS theory was the energy gap separating the multi-degenerate superconducting ground state from the Fermi level. Although the gap is very small, it has been well defined. One of the most descriptive experiments on the energy gap was the tunneling experiment by Giaever.[52] The experiment directly measures the voltage necessary to jump the energy gap.

More recent developments include the empirical confirmation of London's factor-of-two prediction in flux quantization by Doll and Nabaur and independently by Deaver and Fairbank,[53,54] furthering the understanding of flux penetration and expulsion in superconductors. Also, the Josephson[55] junction between two superconducting thin films separated by an oxide layer is thought to have commercial application in computers. The anisotropic behavior of certain properties of superconductors has been explained by overlapping bands,[57] although little correlation has been found between electronic properties and Type II superconducting properties. This is just an extension of the BCS theory to more than one energy gap. These have been the major steps in the development of superconductivity.

CHAPTER II

THEORETICAL BACKGROUND

Elasticity

The normal state behavior of the velocity of sound or elastic moduli[58-60] in a magnetic field has been shown to vary as the square of the external field. In a field comparable to the upper critical field of the samples under study, the normal state change in longitudinal modulus is two orders of magnitude smaller than the observed change in elasticity at the superconducting transition. Also, the reported[5] fractional change in volume at the transition is several orders of magnitude less than the associated fractional change in elasticity. Theoretically, the change in elastic constants at the superconducting transition is founded in a classical thermodynamic argument, as is the approach of all elastic moduli to absolute zero of temperature with zero slope.[61,62] A phenomenological theory of strain and stress effects in Ginzburg-Landau superconductors is given by Labusch.[63] Particular experimental arrangements utilize effective elastic moduli, which are specific combinations of the elastic stiffness or compliance constants. The effective elastic constants for the principle bcc crystal directions are given below in terms of the longitudinal and transverse components.[64]

(100)	(110)	(111)
L: C_{11}	L: $\frac{1}{2}(C_{11} + C_{12} + 2C_{44})$	L: $(1/3)(C_{11} + 2C_{12} + 4C_{44})$

T: C_{44} $\quad$ T_1: C_{44} $\quad$ T: $(1/3)(C_{11} - C_{12} + C_{44})$

T_2: $\frac{1}{2}(C_{11} - C_{12})$

The measured values of the moduli of elasticity for the set of Nb single crystals are given in Table II. All three constants could not be determined for one sample by this technique, since three independent measurements were necessary, and a pure transverse mode could not be generated by a resonant method. Only the (110) orientation is suited for acoustical determination of all three elastic constants within one sample, since the two transverse modes are degenerate for the (100) and (111) orientations. The effect of thermal quenching and mechanical deformation is also noted for these samples. For the polycrystalline samples Young's modulus is defined[65] in terms of the Lame constant (Λ) and shear modulus (μ) as:

$$Y = \mu(3\Lambda + 2\mu)/(\Lambda + \mu) .$$

Four basic experimental procedures have been used to study the change in elastic constants at the superconducting transition. A high frequency (~10 MHz) ultrasonic pulse technique is used to study both the normal and superconducting effective elastic stiffness coefficients. Alers and Waldorf[66,67] have done the only sufficiently accurate work[68,69] using this technique to see the change of parts per million in the elastic constants at the transition. The shear modulus undergoes the largest change at the transition. A second method utilizes the change in damping of a torsion pendulum[70] to observe changes in elastic constants. This is an extremely low frequency method and lacks the accuracy of the following methods. A composite oscillator[71-77] composed of

TABLE II

SINGLE CRYSTAL ELASTIC CONSTANTS OF Nb

Sample (77°K)	C_{11}	C_{44}	$\frac{1}{2}(C_{11} + C_{12} + 2C_{44})$	$\frac{1}{3}(C_{11} + 2C_{12} + 4C_{44})$	$\frac{1}{3}(C_{11} - C_{12} + C_{44})$
Nb (100) #1	14.6	3.90	----	----	----
Nb (110) #2	----	----	15.2	----	----
Nb (111) #4					
Original	----	----	----	21.4	2.63
Quenched	----	----	----	19.7	2.63
Deformed 0.7%	----	----	----	18.7	4.75
Nb (100) #5					
Original	16.8	5.32	----	----	----
Deformed 5.0%	16.4	5.12	----	----	----
Nb (111) #6					
Original	----	----	----	10.9	4.85
Quenched	----	----	----	----	4.91
Deformed 0.3%	----	----	----	----	4.87
Deformed 1.8%	----	----	----	10.8	4.68

Moduli are given in units of 10^{11} dynes/cm^2.

a quartz rod with the sample material bonded on one end is frequently used to observe the change in Young's modulus at the transition. While the accuracy is sufficient with this apparatus, the problem of bonding the sample to the quartz transducer is always present. Kramer and Bauer[76,77] have made measurements using this technique. They concentrated on validifying their measurements by comparing the change in modulus curve with a magnetization curve. They also observed an internal friction peak around 3° K in Nb. A more direct way of measuring the changes in Young's modulus is by a resonating beam technique.[78-80] The changes in velocity and modulus are measured directly via the fundamental resonant frequency,

$$v = fx$$

$$v = M/p$$

While several measurements have been made of the change in elastic constants at the superconducting transition, little interpretation has been given to the structure of the curve in the mixed state region. Although Type I materials obey a linear transition, Type II materials do show a non-linear response in the fractional change of modulus with magnetic field.[81] The capacitive drive technique utilizes a frequency around 50 KHz associated with a wavelength the order of five centimeters. This measurement is truly a bulk measurement compared to the ultrasonic measurements.

In connection with the capacitive drive technique, the loss factor, or attenuation can be measured by the free decay method.[71-80] Much experimental[82-93] and theoretical[94,95] work has been devoted to ultrasonic attenuation, since the higher frequency selects the electronic

component of the attenuation over the lattice component. Superconductivity depends on the number of superconducting electron pairs relative to the number of normal electrons. The low frequency attenuation selects the lattice part primarily and sees only a small electronic component. Previous measurements of changes in attenuation at these frequencies have yielded little or no significant results.[78-80] However, when the losses due to support of the sample and the imperfections of the crystal are minimized, the small electronic component is observed to be similar to the ultrasonic attenuation measurements.[81]

The elastic modulus and acoustic loss factor exhibit the different nature of the harmonic and anharmonic components of the complex elastic modulus of the crystal lattice. The longitudinal and torsional modes are studied to show the effect of the different stresses on the microscopic level. Thus, the accurate determination of the details in the change in elasticity throughout the superconducting transition can yield much information concerning the intermediate state of Type II superconductors.

Normal State

The normal state elastic properties were investigated by observing the acoustic velocity and attenuation as a function of external magnetic field.[47] The actual parameters measured were the adiabatic stiffness constant and the acoustic loss factor, which may be related through the complex notation as $M^* = M_o(1 + i\eta)$. A low frequency wave was propagated with a wavelength much greater than the atomic parameters so that $q\ell << 1$. The wavelengths were determined by twice the sample length at the fundamental resonants frequency and were typically 10 cm. The ob-

servation of a magnetic field dependence of the elastic properties implied an interaction of the lattice ions and electrons with the magnetic field and with each other. A direct interaction was calculated[60] by considering the Lorentz force due to the magnetic field in the fundamental elastic equations. This calculation utilized a self-consistent electric field produced by the ion motion among the electrons. The lattice was pictured as a charged elastic continuum moving periodically with the amplitude of the applied acoustic wave. The magnetic field added an additional restoring force above the ion-displacement-from-equilibrium force which is inherently present due to the acoustic wave. The magnetic stress is dependent on the propagation direction and the polarization of the wave. It was shown[60] that the lattice ion interaction with the magnetic field was much smaller than the observed magnetic dependence and did not yield a major contribution to this effect. The magnetic field did alter the electron reaction with the displaced ions and led to a major contribution of the changes observed in the complex stiffness. The calculated fractional changes in stiffness and loss factor are given below:

$$\frac{\Delta Y}{Y} = \frac{B^2}{4\pi\, p\, v_L^{\,2}}$$

and,

$$\frac{\Delta \eta}{\eta} = \frac{e^2 c^2 B^2}{8\pi^2 \sigma^2 m_e^{\,2} v_F^{\,2} v_L^{\,2}}$$

A quadratic field dependence was found and the magnitude of these terms agreed well with the empirical longitudinal measurements. The torsional measurements demonstrated the expected B^2 dependence, but the magnitude

of the fractional changes did not fit this theory, and no suitable explanation has been found to date. Also, the Fermi velocity, a fundamental electronic parameter, was calculated using the theoretical equation and the experimental data, yielding a reasonable result for Nb. Although this was a low frequency measurement through which one would not usually observe electronic changes, the accuracy of these measurements was sufficient to allow observation of electronic interactions.

Superconducting State

The superconducting state is reached when both the temperature and magnetic field are adjusted to the proper values for that material. Type I superconducting materials undergo a second order phase change at the critical temperature, while all other temperature transition points in non-zero magnetic fields are first order phase changes. The order of the phase change is defined to be the order of the derivative of the gibbs function which is discontinuous.[96] Another phenomenon occurring at the critical temperature is the sudden drop of the electrical resistivity to zero.[9,10] In Type I materials this discontinuity is rather abrupt and occurs within a few millidegrees temperature-width. Physically, a true discontinuity is seldom, if ever, observed due to non-ideal conditions or small fluctuations. The first order phase change in the magnetization of Type I materials could not be a true discontinuity because the magnetic field could not be made perfectly parallel to all faces of a sample which is necessary to reduce the demagnetization effect to zero. The demagnetization factor, or effective magnetization portion of the total magnetization possible for a particular geometry, for a cylindrical sample in a perpendicular magnetic field is ½.[97]

This is the case exclusively in this investigation.

A model of Type I superconductivity that includes all of the observed changes at the transition is the lamina structure model,[64] a model of alternating superconducting and normal state layers. The normal state may be assumed as the basis and nucleate superconducting regions in the normal state, but it is customary to choose the more ordered superconducting phase as the basis and nucleate the less ordered normal regions in it. The lamina model assumes an intermediate state, or width to the transition, so that the transition can occur in small increments. The lamina of normal material are formed at the initial departure from total superconductivity, or the Meissner state. The lamina grow in thickness during the transition until all material is normal. The interfaces between the superconducting and normal regions have associated with them a positive surface energy which is characteristic of Type I materials.

Type II materials have associated with them inherently a mixed state which exists between two magnetic critical fields.[64] Below H_{c1}, all material is superconducting; above H_{c2} all material is normal; and between these two magnetic fields the material is in the mixed state. A single thermodynamic critical field, H_c, may be calculated by setting the area under a magnetization versus magnetic field intensity curve equal to $H_c^2/2$, the change in free energy across the transition. Type II materials typically have a different transition of resistivity due to a thin surface sheath of superconductivity which is not destroyed until a third critical magnetic field, $H_{c3} = 1.7\ H_{c2}$.[64]

Abrikosov[37] proposed a model of vortices to explain the mixed state of Type II superconductors. This was an offspring of the vortices found

in superfluid helium.[98] The principle difference[100] was that superfluid helium was a neutral liquid, while a superconductor was a charged sea of particles within a solid. This model includes the negative surface energy aspect as well as the $\xi < \lambda$ condition. It has been extended to include a quantized unit of flux in each normal state[101] flux tube.[102] Observations of vortices in Type I materials at very low fields prior to the formation of lamina have been reported.[103] The idea that the vortices must be in some regular array led to a most stable configuration of a two dimensional triangular lattice.[104] Recently direct evidence[105] of this lattice has been found by depositing small ferromagnetic particles on the surface of a superconductor and observing the resulting patterns in an electron microscope by means of a replica technique. However, a rectangular vortex lattice has also been observed.[106]

The existence of a parameter to differentiate between the types of superconductivity seemed plausible. The Type I materials with $\xi > \lambda$ showed long-range order, while the Type II materials had a shorter coherence length $\xi < \lambda$. A new parameter[36] $K = \lambda(T)/\xi(T)$ is known as the superconducting Landau-Ginsburg parameter. $K < \sqrt{2}$ defines Type I and $K > \sqrt{2}$ defines Type II behavior. This parameter is also defined in other ways from the thermodynamic quantities. For Type materials $K^{I} = 2\sqrt{2}\ (\frac{e}{hc})\ H_c(T)\ \lambda^2(T)$, and Type II materials as $K^{II} = H_{c2}/\sqrt{2}\ H_c$. It is interesting to note that for Type I materials with $H_{c2} \leq H_c$, $K^{II} \leq 1/\sqrt{2}$. Also, the critical field for surface superconductivity is defined as $H_{c3} = 2.4\ KH_c = 1.7\ H_{c2}$. Theoretically, the Landau-Ginsburg equations give a prediction of K, as demonstrated by DeGennes.[107]

The existence of a filamentary or sponge model for superconductors

in zero external magnetic field has been suggested[108] to explain the temperature dependence of superconducting properties. The size of these normal state regions shrinks to zero as the temperature goes to zero. In comparison, the size of a vortex due to magnetic fields is determined by the thickness of films (< 2000 Å) and is nearly constant in a bulk material.[109] Rocher and Renard[110] suggested the existence of several quanta flux lines near the surface in the region where the penetration of the external magnetic field must be considered. The possibility of expanding vortices and a density of vortices depending on the vortex size is presently under consideration.[81] Nucleation of vortices at H_{c1} is thought to occur near the surface and move inward.[111] Conversely, some work[112] has been done on the nucleation of superconducting regions near H_{c2} in a decreasing magnetic field. Also, the rate at which flux enters or leaves various materials, when the magnetic field is changed suddenly, has been measured,[113] and the results used to determine the flux flow resistivity.

The motion of vortices within a superconductor has given rise to many experiments.[114-118] The charge density in the superconducting region near the vortex must be considered when flux is moving throughout the superconductor.[119] A surface barrier[120,121] excludes the magnetic flux from the inside of the superconductor until the critical field is reached. Differences in this surface barrier, or surface condition, may affect H_{c1}, similar to supercooling a liquid. Once the flux penetrates at H_{c1}, the diffusion of flux throughout the sample has been measured[122] to take a few seconds for the maximum diffusion rate and approximately a hundred seconds for equilibrium. While the surface barrier may inhibit the initial motion of vortices, there are ways to

produce flux motion internally. The motion may be increased by physical stresses or by thermal gradients, which cause entropy transport via the flow of vortices.[123-126] A "Peltier" effect[127] has been observed in Type II superconductors due to flux flow. A change in magnetic field in the mixed state will cause a transient of flux entities crossing the superconductor and may be observed in D.C. noise level measurements.[128] Flux motion has been recorded, also, as flux jumps, i.e., a substantial amount of flux moving simultaneously, causing a jump in the measured parameters.[129,130] Associated with flux motion are dissipative mechanisms and an inertial mass.[131] Apart from the electrical resistance in the normal core of vortices,[101] there is also a viscosity to flux flow.[133,134] Radiation from moving vortices has also been shown to exist.[135] Dislocations in a crystal exert a force[136,137] on vortices and cause flux to be trapped or pinned[138-140] when the external field is removed. The amount of trapped flux gives an indication of the number of imperfections within the crystal.

Dislocations may also exist in the lattice of vortices itself.[141,142] Theoretically the vortex lattice should have elastic moduli[143,144] and be able to support a new type of wave propagation[145,146] a compressional wave with the wave vector perpendicular to the magnetic field. Measurements[147] have shown the existence of a shear constant for this lattice, but no new compressional mode was observed. Thus, the vortex model is a well-substantiated model for Type II superconductors with many refinements yet to be made in the details of the model.

Dislocations

Dislocations are important in crystalline materials because they

allowed easy plastic deformation. Dislocations and impurities composed the larger subject of imperfections. While impurities are divided into substitutional and interstitual replacements of lattice atoms, dislocations are divided into edge and screw type inhomogenities in the lattice structure itself. A fundamental quantity in dislocation theory is the Burgess vector.[148] This vector is defined in terms of a Burgess circuit which encompasses the dislocation line. A Burgess circuit including a dislocation is compared to a Burgess circuit containing only perfect crystal and differing by the Burgess vector. This vector defines the direction and magnitude of slip.

Dislocations are often found as lines through a crystal or lines forming closed loops within a crystal. Edge dislocations are defined by the Burgess vector being perpendicular to the dislocation line, while screw dislocations have the dislocation line parallel to the Burgess vector.[148] A mixed dislocation is some combination of edge and screw type dislocations and has a Burgess vector which is neither parallel nor perpendicular to the dislocation line. Edge dislocations have a slip plane which includes both the dislocation line vector $\vec{g}$, and the Burgess vector $\vec{w}$. The normal to this plane is given by $\vec{g} \times \vec{w}$. The slip plane for screw dislocations contains $\vec{w}$, but it is not uniquely defined, as for edge dislocations.

Nb, V, and Ta are body centered cubic (b.c.c.) metals with primary slip directions along a [111] direction.[4] The dislocation lines lie in a plane perpendicular to this for edge dislocations. Although b.c.c. crystals have exhibited (110), (112), and (123) planes, a (110) slip plane is the preferred plane.[4] Slip in the other planes is apparently attributed to a resultant of slip along several (110) planes. This would

mean that the dislocation lines are in a [112] direction, perpendicular to a (110) slip plane, and perpendicular to the [111] slip direction. Dislocation motion is most easily excited by a shearing force on the dislocation line. A shear wave propagation with the propagation vector along a [111] direction should easily excite dislocation motion in a b.c.c. crystal.[4]

The effect of impurities on dislocation motion is not within the scope of this investigation, but it is believed that impurities effect dislocation motion by adding pinning points. Thus, impurities add to the lattice attenuation at low temperatures, but do not effect other bulk properties substantially.

The radiation of dislocation effects to superconducting phenomenon has been suggested in only a few previous works. Kramer and Bauer[76] reported a relaxation peak around $3^{o}K$ in Nb, and was also observed in this investigation. This suggests a lattice phenomenon, possibly associated with dislocations, since the absorption maximum shifts in temperature between the superconducting state and field induced normal state. The dislocation can be considered[149,150] a vibrating string, pinned by impurities, and damped by viscous motion through the sea of normal electrons. The attenuation due to dislocations is amplitude dependent and reflects the release of the dislocation line from the pinning points at large stress amplitudes. This amplitude dependence of the attenuation in the superconducting state is shown for high purity lead[151-154] where the temperature dependence of the BCS electron-phonon interaction can be completely suppressed below T_c by dislocation motion. Changes in the plastic flow characteristics below T_c have been interpreted in terms of dislocation motion.[155-157]

Recent measurements on superconductors immediately above T_c have indicated contributions due to transient Cooper pairs, observed as excess conductivity in the normal state.[158-161] This enhancement of transport properties is attributed to thermodynamic fluctuations of the Cooper pairs.[162-164] In this investigation we are interested in the magnetic field dependence of transient Cooper pairs above H_{c2} or above the stable superconducting state. Hake[165] has observed magnetic fluctuations in D.C. conductivity. The acoustic parameters are used to correlate a magnetic fluctuation effect to the viscous damping of oscillating dislocation lines in this work.[166]

CHAPTER III

APPARATUS

Types of Measurement

There are several basic ways to make dynamic acoustical measurements, depending primarily on the frequency range of interest.[4] Low frequency measurements generally use a torsion pendulum method from 0.1-10. Hz. The attenuation measurements for this method are limited to a sensitivity, or $Q^{-1} = 10^{-4}$. At intermediate frequdncies, a resonance method is commonly used from 100. Hz - 300 kHz. The sensitivity of attenuation measurements is $Q^{-1} = 10^{-7}$. For ultrasonic frequencies, a pulse technique is generally used from 1.0 - 1000.MHz. The sensitivity of this method is generally limited by scattering of the waves to a $Q^{-1} = 10^{-4}$.

The choice of the resonance method for kHz range measurements was because of its lack of use in the superconducting state, and its extreme use at higher temperatures to study dislocation relaxations of the Bordoni Peak[78] and other internal friction phenomena.[4] The acoustic parameters studied using the method were the elastic modulus and the acoustic loss factor. The longitudinal mode, or Young's modulus, and the torsional mode, or shear modulus, were investigated, as well as the associated single crystal elastic constants. Other measurements that were made included the electrical resistivity, the magnetization, and the temperature and magnetic field dependences of the complex elasticity.

Some explanation of the relation between the experimentally observed quantities and these parameters is needed. The elastic modulus (M) is determined via the fundamental resonant frequency (f) of the sample. It has been shown[79] that the fractional changes are related by

$$\frac{\Delta M}{M} \doteq \frac{2\Delta f}{F} .$$

The acoustic loss factor (η) is observed via the decay time (t) of the freely decaying oscillation amplitude of the sample's resonant frequency and is related through

$$\eta = \frac{(\#\text{db decay})}{8.68\ \pi\ ft} .$$

The magnetization is directly proportional to the induced voltage measured in the coils and is, therefore, in arbitrary units. It can be calibrated with reference to the applied field value at the critical points. The other parameters have an obvious relationship to the observable.

Longitudinal Mode

The complex elasticity (stiffness and attenuation) of a superconductor is determined by a standing wave technique, involving a capacitive transducer with the sample used as one plate of the capacitor. The electronic driving signal is terminated in a brass electrode of approximately the same diameter as the sample and alligned coaxially with it (Figure 1). The spacing between the electrode and the sample is adjustable in order to insure sufficient driving power to transduce the electrical signal into an acoustic wave in the sample. The varying electrode voltage causes a varying force on the end of the sample, exciting the

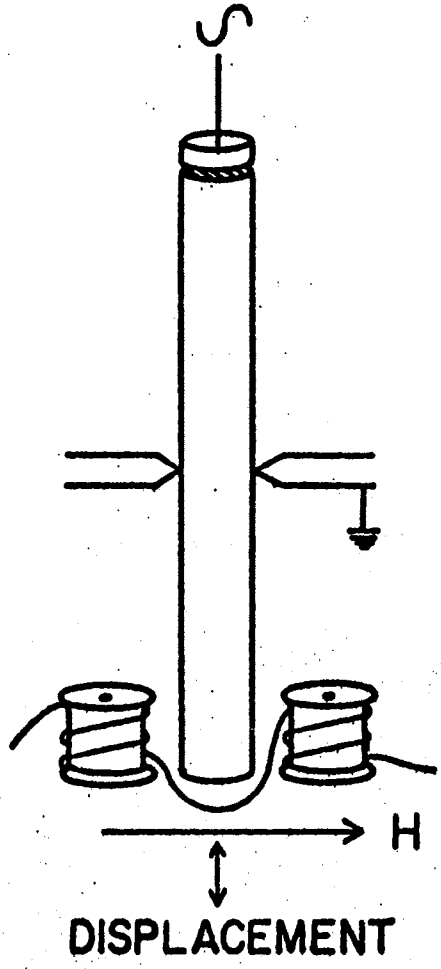

Figure 1. Sample Mount

acoustic wave. The longitudinal mode is excited by using the parallel plate capacitor transducer, which is also a part of the tank circuit in an FM detector. The principles of this method of measurement are described elsewhere[167] and depicted in a block diagram in Figure 2.

For the longitudinal mode the real part of the complex elasticity is the stiffness, or Young's modulus, monitored by observing the fundamental resonant frequency of the cylindrical sample. Usually in this investigation the fractional change in modulus is studied as a function of magnetic field, but some measurements as a function of temperature and amplitude were also made. The imaginary part of the complex elasticity reflects the losses, or gives the acoustic loss factor. The resolution of the resonant frequency is determined by the width of the resonant peak which in turn indicates the attenuation of the entire system. Extraneous attenuation is minimized through reducing sound radiation from the specimen by operating at ambient pressures of 500μ and by using a suspension system consisting of four rigidly mounted pins which support the specimen in a nodal plane. This reduces the relative motion between the specimen and mount and minimizes its contribution to the attenuation. Further reductions in attenuation result from acid etching which removes imperfections and impurities from the sample surface. Annealing at temperatures much below the melting point decreases the attenuation in niobium substantially without changing the critical fields or the resistivity ratio. A very small attenuation is observed in niobium after being subjected to these procedures, yielding a decrease in vibration amplitude over 60 db of a few minutes. The resulting bandwidth at half power points is the order of five thousandths of a cycle at 50 kHz, allowing a resolution of better than one half part per million

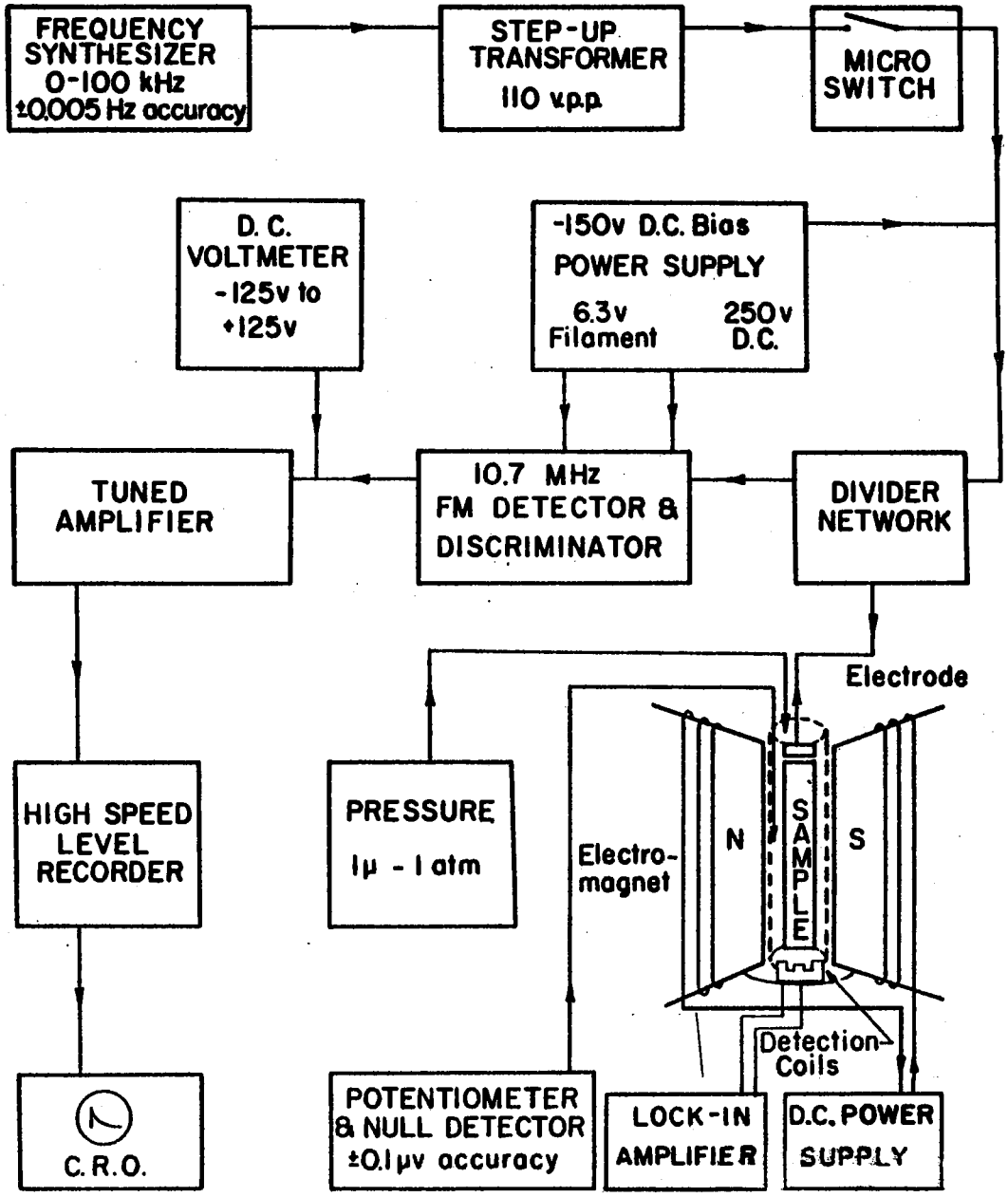

Figure 2. Block Diagram of Apparatus

change in elasticity (Figure 3).

The effect of the 10 Mhz frequency of the FM detector on the sample has been considered. Since the attenuation increases with frequency, any contribution of attenuation due to this higher frequency would be damped out in a time very short compared to the relaxation time associated with the 50 kHz frequency and leads to no significant changes in the measured attenuation. Figure 4 shows an enhanced attenuation at three times the fundamental frequency of the sample compared to the attenuation at the fundamental frequency. The dynamic modulus, however, is only slightly lowered at the higher frequency. Unless the 10 MHz happened to be precisely an odd multiple of the fundamental frequency, no effect would be observed. If an odd effect should be encountered and associated with this higher frequency, a slight change in length, such as by an acid etch, would offset the fundamental wavelength so that the higher frequency would no longer be on resonance. This has not been observed and any effect due to the higher frequency excitation is disregarded.

The calculation of the strain amplitudes used during this investigation is necessary for comparison with other data. The acoustic driving stress (Σ) is given in terms of the velocity (v) and impedance (Z) as

$$\Sigma = vZ.$$

At resonance conditions the impedance reduces to the resistance (R) and the velocity may be written as the product of the maximum strain amplitude (τ^{max}) and the angular frequency (ω). Thus, the strain amplitude is given by

$$\tau^{max} = \Sigma/\omega R .$$

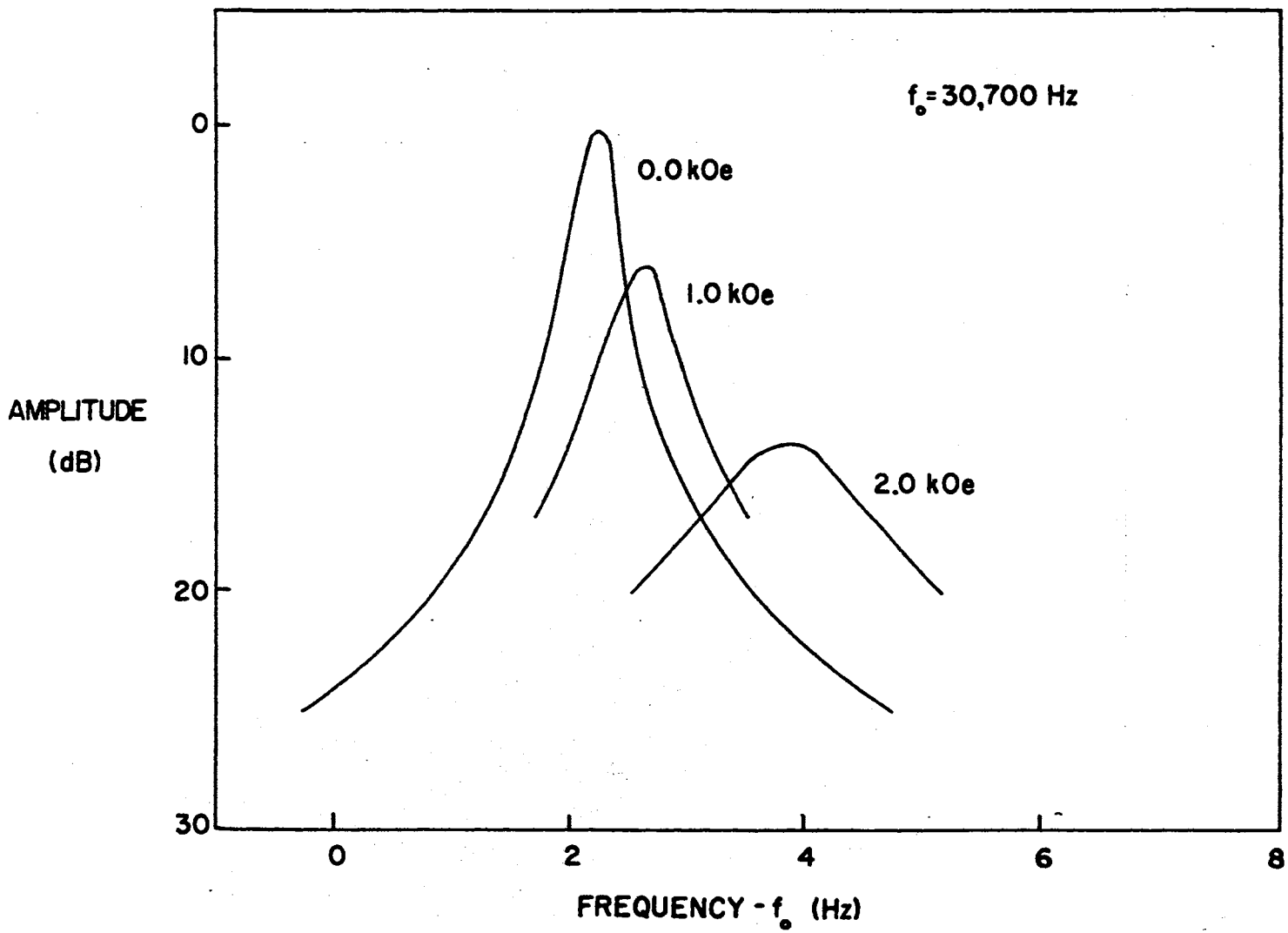

Figure 3. Change in Elasticity as a Function of H

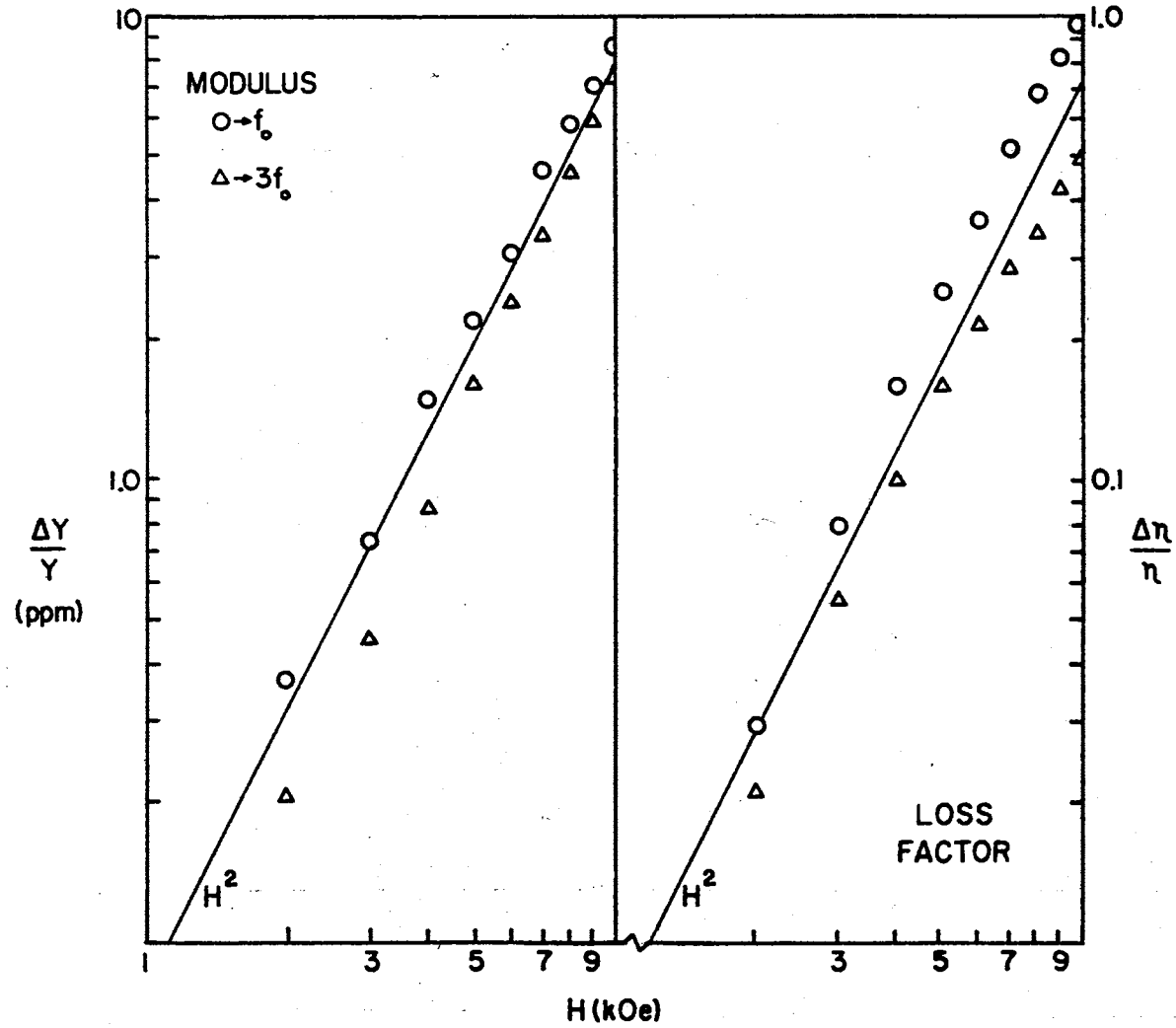

Figure 4. Elasticity at $3f_o$

The quality factor is defined as

$$Q = \omega I/R ,$$

and

$$\tau^{max} = \Sigma Q/4\pi^2 f^2 I ,$$

where f is the frequency and I is the mass per unit area, or inertia. Since Σ/I reduces to a force (F) per unit mass (ρV), this equation becomes

$$\tau^{max} = FQ/4\pi^2 f^2 \rho V .$$

The force for this parallel plate capacitor arrangement has been given by Guess and Thurston[167] as

$$F = E_o E_{ac} A\varepsilon_o / d_o^2 .$$

The strain amplitudes can then be calculated from experimentally measurable parameters as

$$\tau^{max} = E_o E_{ac} A\varepsilon_o Q/d_o^2 4\pi^2 f^2 \rho V .$$

Typical values for these parameters are E_o = 150 volts, E_{ac} = 10-100 volts, A = 3.18×10^{-5} meters^2, $\varepsilon_o = 8.85 \times 10^{-12}$ farads/meter, Q = 10^6, $d_o = 2 - 10 \times 10^{-6}$ meters, f = 5×10^4 Hz, $\rho = 8.57 \times 10^3$ kilograms/cubic meter for Nb, and $V = 0.5 - 2.0 \times 10^{-6}$ cubic meters. This yields a strain amplitude of $10^{-9} - 10^{-6}$ meter/meter. The area of the torsional drive heads is about 1/3 that of the longitudinal and thus reduces the strain amplitude, but the resonant frequency is also lowered by about 2/3 and causes no net order of magnitude change on the strain amplitude.

The separation distance of the drive head from the sample was meas-

ured by calibrating the dial position of the tuning capacitor in the tank circuit of the FM detector. As the drive electrode was moved away from the sample's end, the capacitance of the system decreased and the tuning capacitor was adjusted to make up the difference in capacitance. The dial position of the capacitor was plotted as the sample was moved away, and the voltage output on the oscilloscope was noted for each position. The sample was then replaced with an open-ended micrometer, and the separation (d) measured at each dial position of capacitance (Figure 5). It should be noted at this point, that when the drive head was too close ($d < 0.0005$ inches), spurious results appeared, such as additional resonances, shifts in resonances, and increased attenuation at all frequencies. This may be corrected by backing the drive head away until the frequency no longer changes with separation.

Torsional Mode

The capacitive drive method of exciting longitudinal modes has been used previously, but this is the first application of the method used to excite torsional modes. A different torsional mode generation in the kilohertz frequency range was described by Wegel and Walther.[168] Their torsional oscillations were generated electromagnetically by the eddy currents induced at one end of the specimen via an attached armature, and the amplitude was measured by the current induced in a coil which vibrated in a stationary magnetic field at the other end of the specimen. The new method described herein is particularly useful for measuring small changes in elastic moduli and changes in the acoustic attenuation via the free decay method, since the sample has no transducer attached to it. The fractional change in elastic modulus as a function

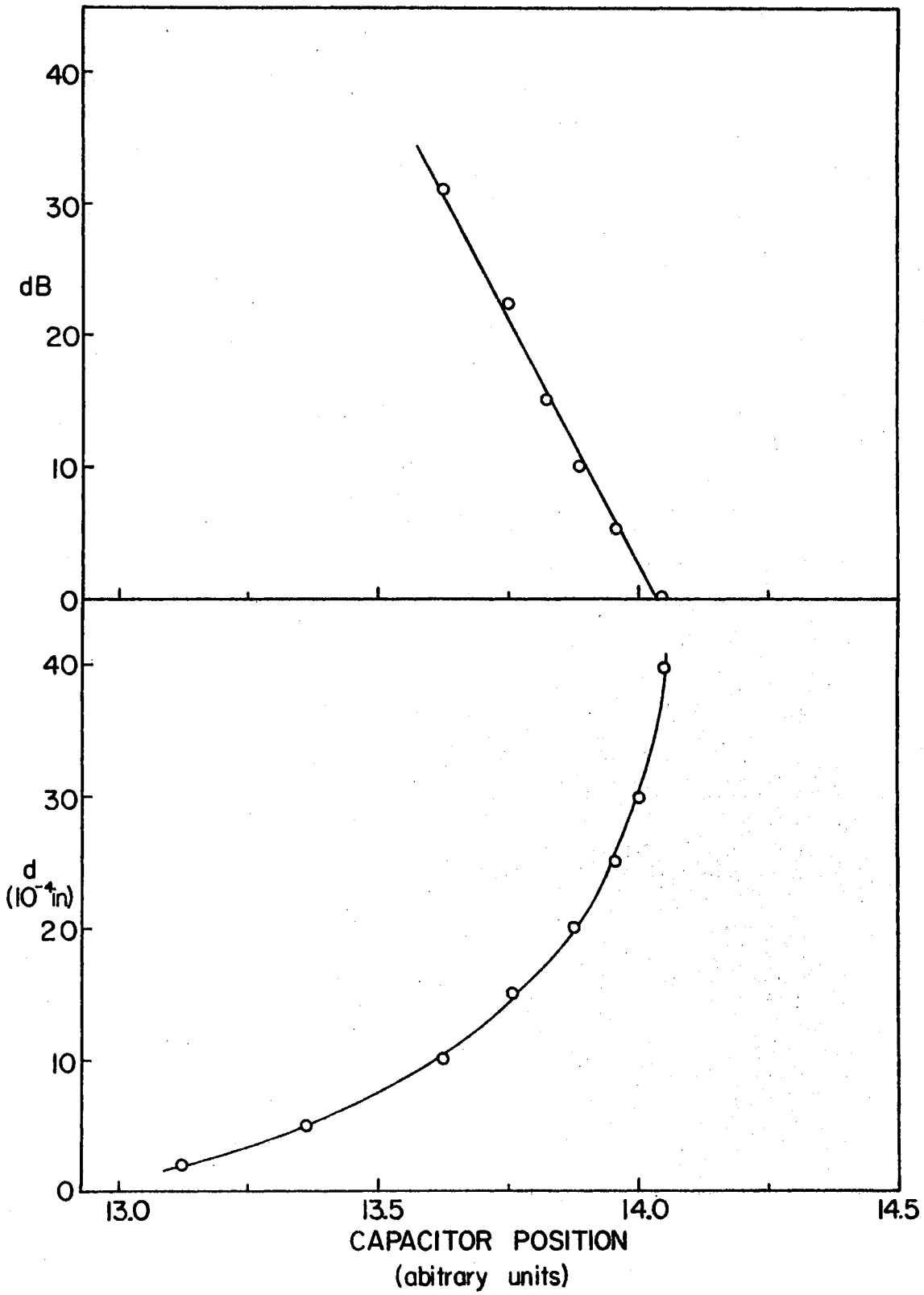

Figure 5. Effect of Electrode Separation

of magnetic field as predicted[60] has been used to determine the optimum capacitor design for the torsional mode.

The theory of elasticity has shown that the shear modulus and Young's modulus are defined in terms of the Lame constants. The determination of Young's modulus by eigher the extensional or flexual modes and the modulus of rigidity by the torsional mode will define both of the Lame constants for isotropic materials.[65] The method described below defines a way to determine both the Lame constants simultaneously via the longitudinal and torsional modes. Interpretation of torsional mode generation in single crystals is more difficult, since the orientation of the long axis of the sample determines the wave propagation direction and the particular elastic constant observed. For example,[64] in cubic single crystals oriented along a [100] direction, the longitudinal mode is simply a measure of c_{11}, while the torsional mode measures c_{44}. Some cubic orientations do not support torsional modes, e.g., the [110] direction does not have degenerate shear modes and cannot support a simple torsional mode. The combination of longitudinal and torsional modes also defines Poisson's ratio (ν), the ratio between the lateral contraction and the longitudinal extension of the specimen,

$$\nu = \frac{Y}{2\mu} - 1 = \frac{f_L^2}{f_T^2} - 1 .$$

The simple parallel plate geometry used for longitudinal mode excitation must be modified to excite torsional modes. The design idea was to produce a dynamic torque on the sample and via a suitable capacitor, and was accomplished in several different ways. One way was to cut the sample in the form of a long cylinder with a fin extending from one end along a diameter and of minimum machinable thickness. The

driving electrode was cut so as to form a capacitor with the fin in two places. The torque action was applied by driving the fin dynamically on opposite ends and opposite sides (Figure 6a). This design had several problems. A fin length of approximately 1/8 inch also was a characteristic resonance of the fin itself. Changing this fin length showed that the change in resonant frequency of the entire rod was quite large. Also, it was noted that the fractional changes in modulus with this fin design was anisotropic when in a magnetic field. This is attributed to additional eddy cuttents in the fins, since tests were made on isotropic polycrystalline samples. Cutting out the center part of the fin, because it contributed very little to the torque action, did not solve the characteristic fin length problem or did it solve the additional eddy current problem.

Another design utilized moment arm fins (Figure 6b), but proved to be very difficult to prepare and maintain one continuous sample. Since the capacitor spacing between electrode and fin was very critical to the driving power, the allignment of spacing became a problem due to the difficulty of machining the sample precisely.

A design using only a component of the torsional and a component of the longitudinal mode was investigated. The sample end was cut at a 45° angle to the cylinder axis and wedge-shaped in appearance (Figure 6c). The electrode was cut with the fins offset to produce the torque action. The signal level was greatly reduced, as would be expected, due to only a part of the applied signal being torsional in magnitude.

The best design was realized by notching the sample end and putting the fins on the driving electrode (Figure 6d). This design deleted the eddy current losses in the fins of the above types. The effect of the

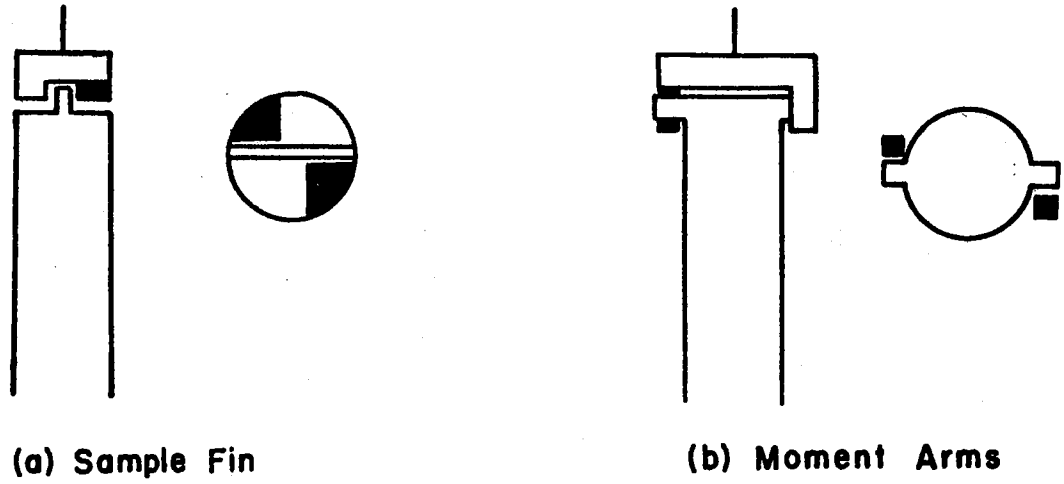

(a) Sample Fin

(b) Moment Arms

(side and top views)

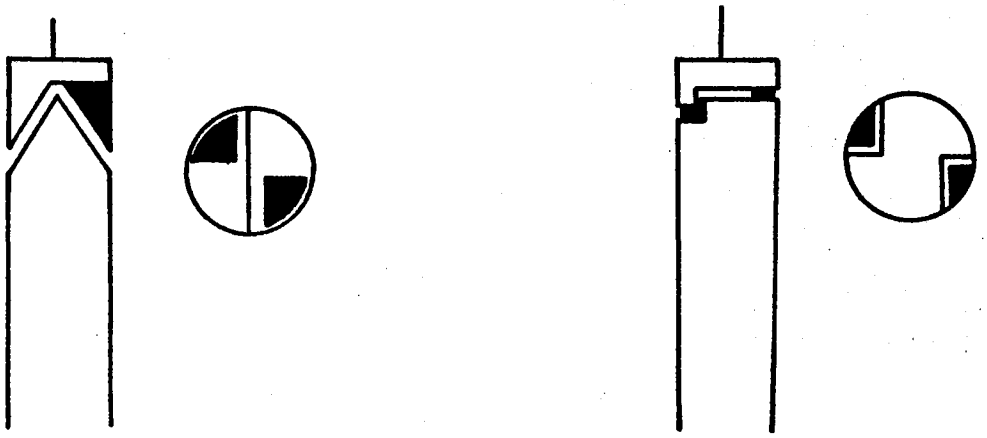

(c) Wedge Top

(d) Electrode Fins

Figure 6. Torsional Drives

small amount of mass removed at the sample end was not noticeable. Approximately 1% of the total mass was removed to form the notches for the driving electrode fins. A study on the effect of removed mass was conducted by removing different amounts of mass from the ends of the rod. This study showed that the resonant frequency of the rod was increased as mass was removed, but the fractional change exhibited a repeated dependence on the square of the magnetic field (Figure 7). Also, the effect of removing mass along the length by notching a series of grooves at regular intervals was checked and found that the frequency was lowered, similar to a series of springs and point masses (Figure 8). The additional convenience of driving both the torsional and longitudinal modes simultaneously was also noted. When the bulk of the electrode is placed near the sample end and the electrode fins extend into the notches on the sample, both modes are driven. The bulk of the electrode may be placed further away and only the torsional mode driven, or the electrode fins may be deleted and only the longitudinal mode excited. This capacitor design was, therefore, the optimum design of those tested.

The various electrodes were tested at $300^{\circ}K$ and $77^{\circ}K$ by measuring the fractional change in modulus of commercial Al over a 10 kOe magnetic field range (Figure 9). The isotropic behavior of the modulus change for various magnetic field orientations in a plane perpendicular to the long axis of the cylindrical sample was important. The design using the fins on the electrode showed no anisotropic behavior with magnetic field orientation. The fractional change in elastic modulus and attenuation also demonstrated a dependence on the square of the magnetic field, as predicted by the existing theories.

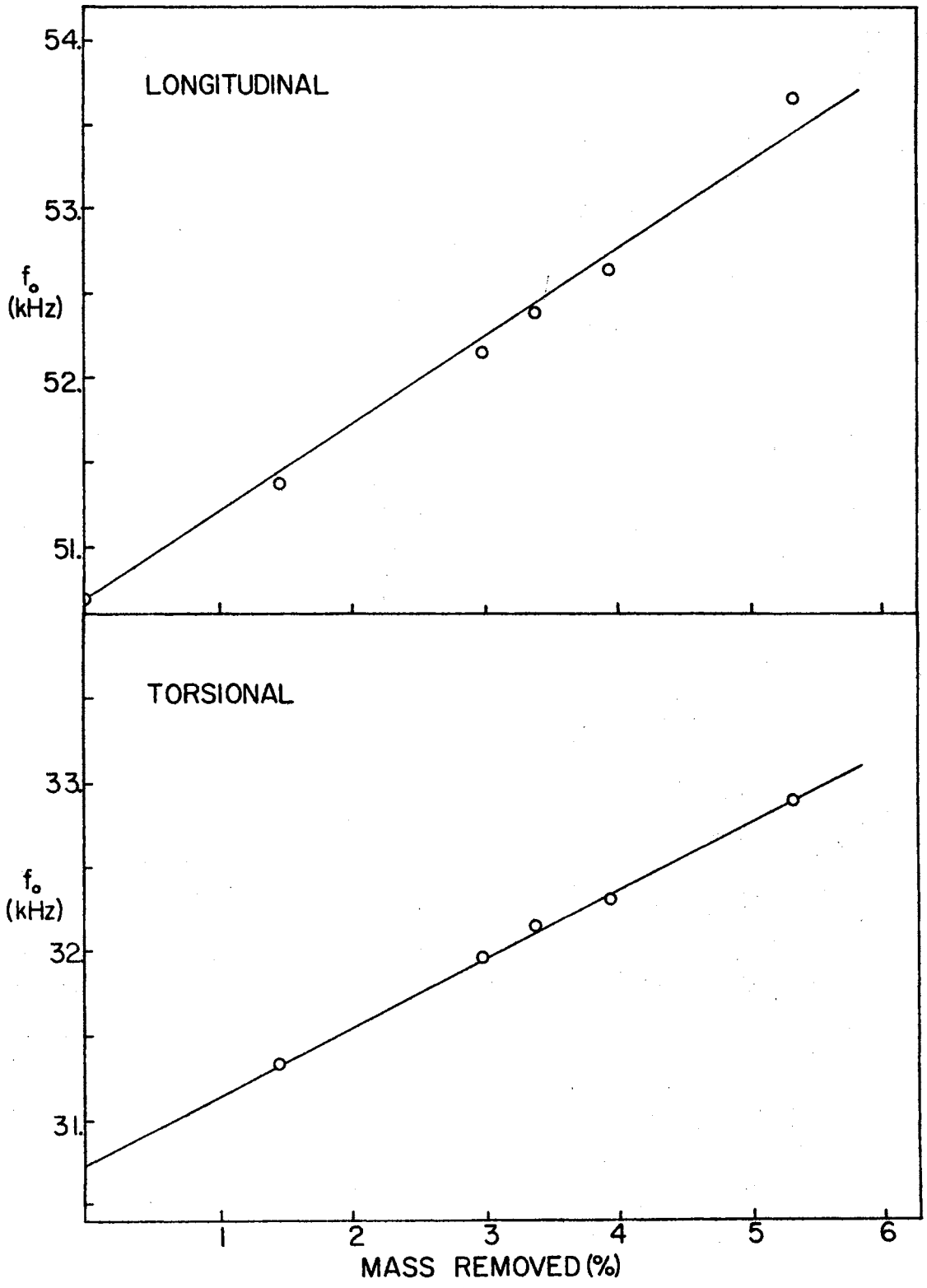

Figure 7. Effect of Removing Mass From End of Sample

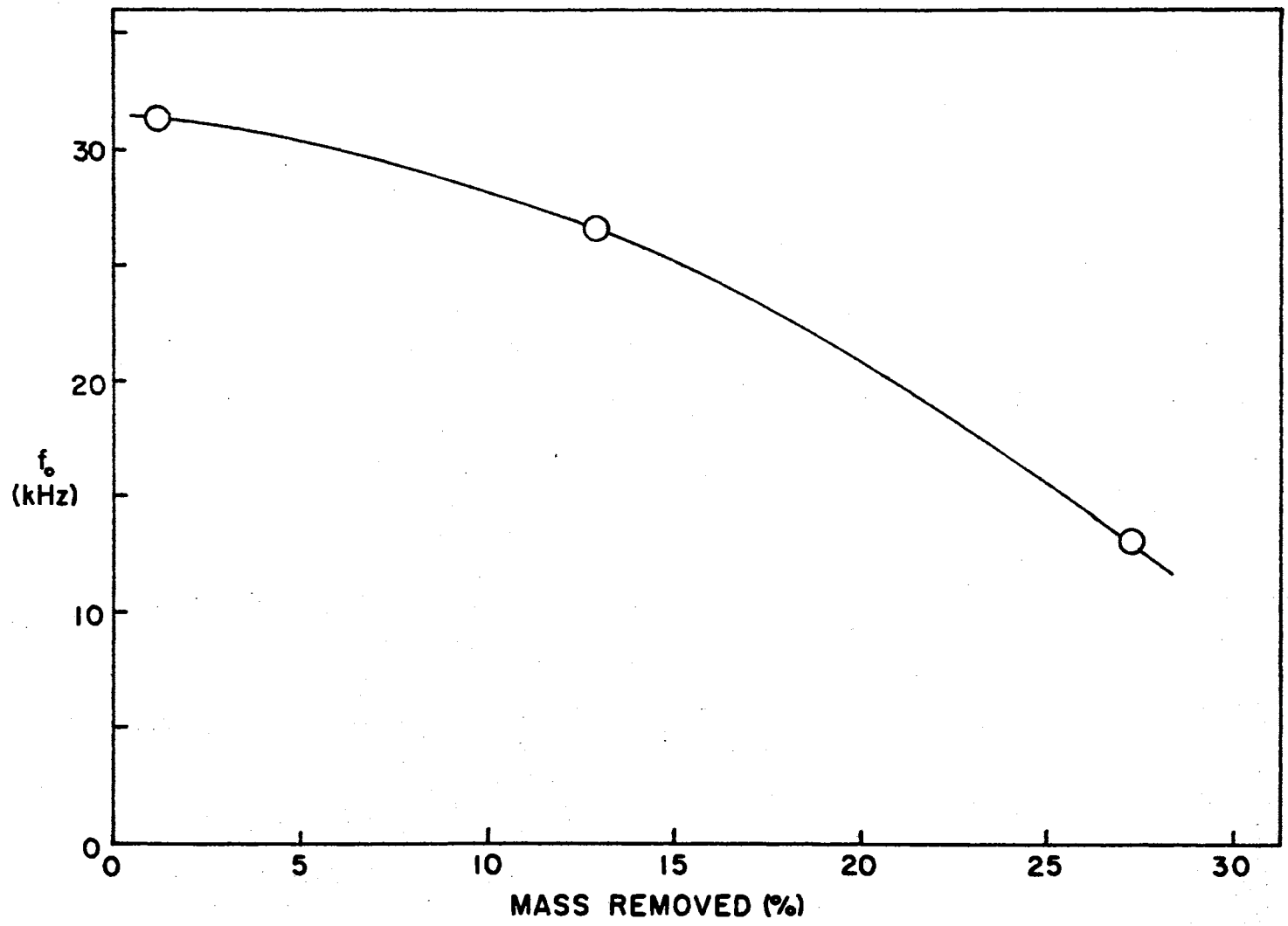

Figure 8. Effect of Removing Mass Along Length of Sample

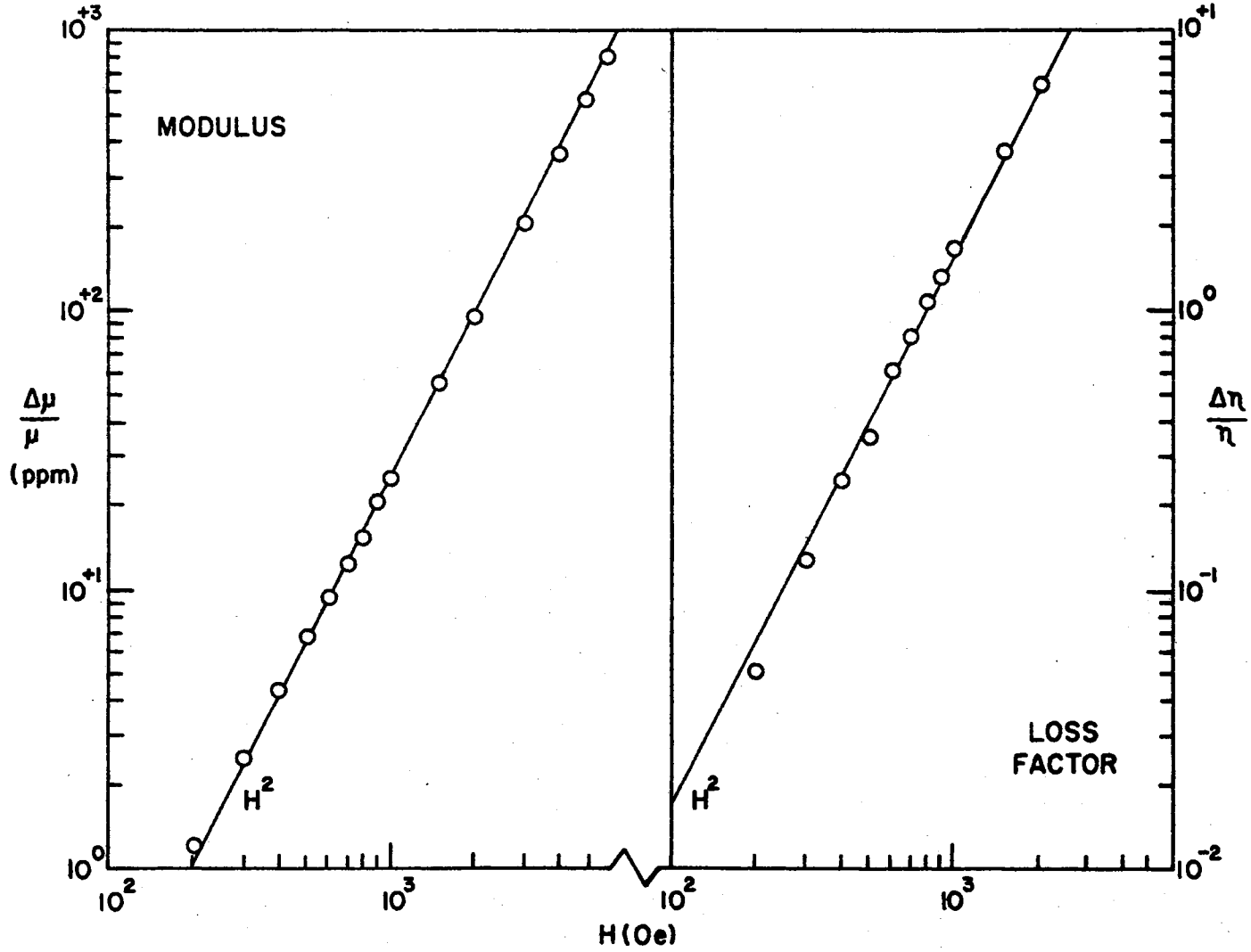

Figure 9. Torsional Drive Fit to H^2

Other Apparatus and Measurements

Since theory and experiment have shown agreement in demonstrating a dependence on the square of the magnetic field for the acoustic parameters under consideration, this dependence was used to check other effects. The magnetic field measurement was accurate to ±1% using a rotating coil gaussmeter and was the limitation of the accuracy in general. Control experiments[79] were conducted to find the effect of the tightness of the pins on the sample and the position of the pins relative to the center of the sample length, the predicted nodal plane. An ambient pressure of less than 1000μ showed no effects on the measurements, while a greater pressure added to the losses of the system. Although the acoustic parameters showed an amplitude dependence of their magnitude, the fractional changes showed no amplitude dependence. The chosen orientation of the sample length being perpendicular to the magnetic field added a demagnetization factor of 1/2 in agreement with the theoretical prediction. Some earlier work was performed using a magnet with a field less homogeneous than 1% over the length of the sample and caused some difficulties near the critical fields. All of the presently reported work was performed using a magnetic field homogeneity of 0.1% along the length and 0.01% across the diameter of the sample, leading to no interpretation problems near the critical field points.

Some magnetization measurements were made to correlate the elastic parameters to the better known magnetic parameter.[169] The magnetization was measured simultaneously with the elastic parameters by placing a set of pick-up coils near the end of the oscillating sample and recording the voltage induced in the coils by the oscillating dipole field in this region. The magnetization was for the longitudinal mode only,

since the orientation of the pick-up coils relative to the maximum displacement of the sample's end was easily achieved for maximum sensitivity. A phase sensitive detector was used for this voltage measurement and indicated a 180° phase change between the diamagnetic and paramagnetic states.

Temperature measurements were made above and below liquid helium temperature. Below $4^{\circ}K$ the vapor pressure of the liquid helium was used to indicate the temperature to $\pm 0.1^{\circ}K$. Above $4^{\circ}K$ a gold-cobalt versus silver-normal thermocouple was used and calibrated to within $\pm 0.5^{\circ}K$. A better thermocouple was the resonant frequency of the sample as changes of $10^{-4}\ ^{\circ}K$ could be detected, but the reproducibility from run to run of the absolute value was only $\pm 2^{\circ}K$.

The electrical resistivity of all samples was measured using a standard four probe technique with a sensitivity of 5×10^{-9} ohm-cm.[170] The resistivity ratio of the resistivity at room temperature compared to that at $4^{\circ}K$ gives an indication of the sample's purity, since the electronic mean free path is affected by impurities. Kittel[64] gives the relation between the electrical conductivity and the electronic mean free path. For Nb this reduces to

$$\ell(\text{cm}) = 1.02 \times 10^{-11}\ (\text{ohm-cm}^2)\sigma\ (\text{ohm-cm})^{-1}.$$

Since Nb is superconducting at $4^{\circ}K$, the measurement of the resistivity is not straightforward. The superconducting state may be destroyed by application of a magnetic field at $4^{\circ}K$. Recording of the magnetoresistance of the superconductor above its critical field allows extrapolation of the high field data back to zero field. Then the residual resistnace ratio (RRR) may be formed and the electronic mean free path

at $4^{o}K$ calculated.

Although the samples were not produced in this laboratory, some sample preparation apparatus is necessary to make the samples suitable for data taking. The samples were either purchased from Materials Reserach Corporation (MRC) or on loan from Oak Ridge National Laboratory (ORNL)[171] in the form of right circular cylinders. The samples of Nb from MRC had a typical mass spectrograph with them indicating the major impurities were dissolved gases and were found to have a RRR less than 100. The ORNL samples were annealed near the melting point ($2000^{o}C$) for 50 hours at a pressure of 10^{-10} mm Hg. removing most of the gaseous impurities and yielding a RRR of 2500. As each sample was received, a short piece was cut from one end to use at ultrasonic frequencies and the longer pieces to be used in this investigation. Some samples were cut on a spark-erosion machine[172] and others on a string saw. After cutting, the samples were severly etched in 50% HF - 50% HNO_3 solution diluted with distilled water to the desired etching strength, approximately 1/3 water in the final etchant. No difference between the two cutting methods could be detected in surface damage, x-rays, or other measurements of this investigation. A Laue back-reflection x-ray technique was used to determine the orientation of the long axis of the single crystals and the direction of the magnetic field perpendicular to this axis. While the x-ray technique was accurate to better than $1/2^{o}$, the magnetic field vector relative to a sample direction was reproduced to only ±5%, because the transfer of the sample from the x-ray machine to the sample mount.

The MRC samples were annealed at $1100^{o}C$ in a vacuum of 10^{-6} torr overnight to improve the Q of the sample. The rate of cooling the sample

after annealing determines the equilibrium number of dislocations. A slow cooling process results in fewer dislocations than a quench. To study the effect of dislocations the sample was tested as originally received, after quenching from 1100°C to room temperature in a silicon oil bath, after subjected to a 1000 Curie cobalt radiation source for 10 hours, and after compressional deformation up to 5% along specimen diameters.

An attempt was made to prepare some alloy samples of Pb, Sn, and In by a co-worker in this laboratory.[173] The attempt was a crude one performed principally to test the difficulty associated with sample preparation for the elastic measurements. The alloys were mixed by percentage weight of granular or sheet metals, heated in a vacuum of 10 microns to the melting point of both metlas, and then cooled below the freezing temperature while under external agitation. It was hoped that the agitation would mix the alloy evenly and free most of the dissolved gases. The metals of Pb, Sn, and In were chosen because the melting temperatures were easily attained by the Hoskins FH303A furnace, because some previous superconductor work had been done on these alloy systems,[174,175] and because these metals were readily available to us in granular and sheet form.

CHAPTER IV

RESULTS AND DISCUSSION

Normal State

For a more complete understanding of the phenomena associated with the transition from the superconducting to normal state, an understanding of the normal state behavior must first be obtained. Most of this work was performed at constant temperature and as a function of magnetic field. The normal state measurements were made at 300°K, 77°K, and above the superconducting critical field at 4°K. Measurements as a function of temperature in Nb indicated an internal friction peak at 3°K and the Bordoni internal friction peak[79] at 35°K in agreement with other such measurements.

In sequel to the previous work, the theory[60] for the longitudinal mode elasticity is further verified in Figure 10. The fractional change in elastic modulus demonstrates a dependence on the square of magnetic field for four different materials: Al, V, Nb, and Ta. From this plot it is also evident that the mass density contributes to the difference between samples, since the least dense material, Al, demonstrates the largest fractional changes and each greater density material shows less change in modulus. The theory predicts the changes at any one magnetic field value should scale inversely with the product of the density and square of the sound velocity in Gaussian units. The velocity of sound in these materials differs only slightly, and, thus, the above product sup-

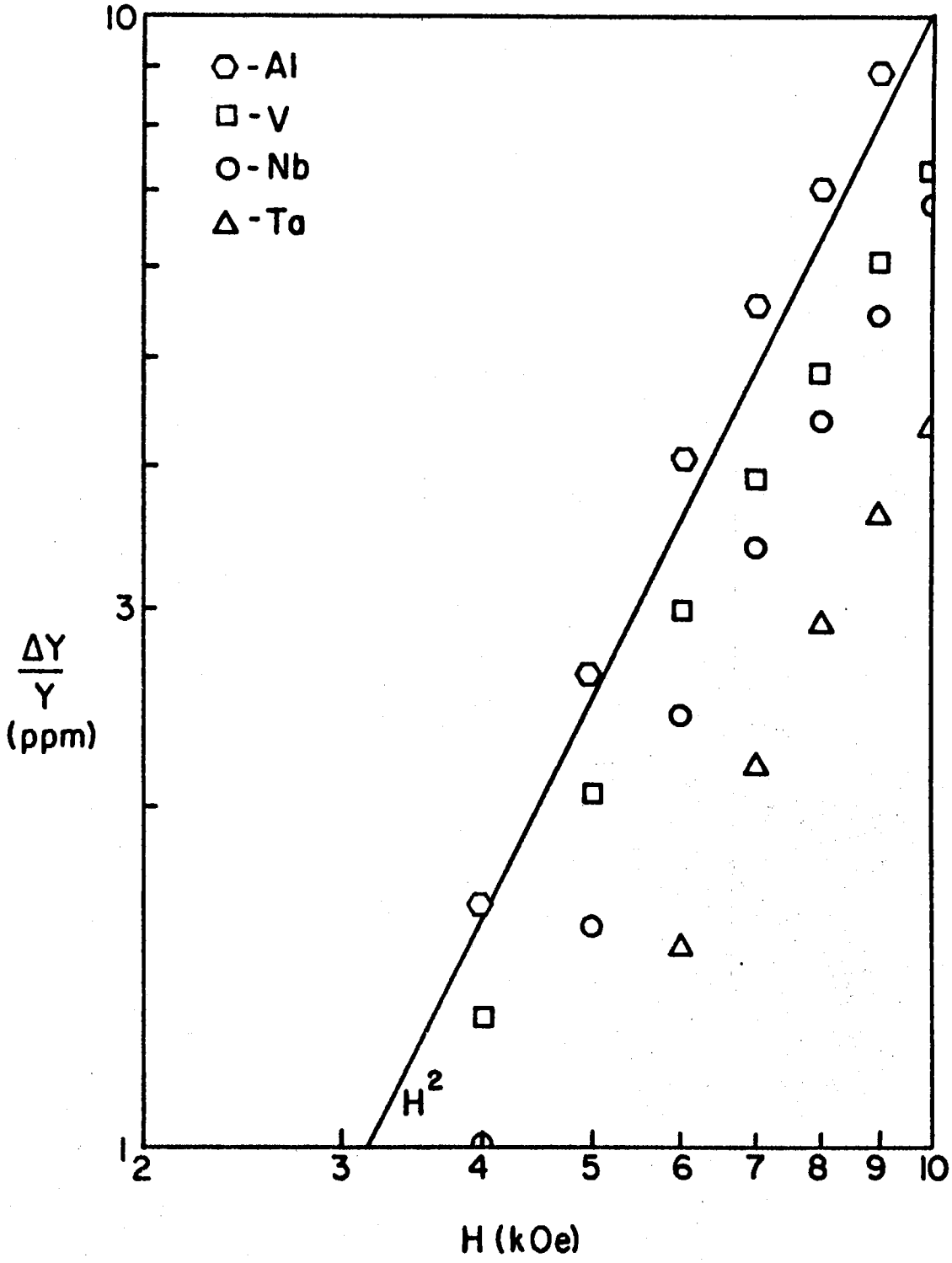

Figure 10. Longitudinal Modulus Changes

ports the theory. Also, the magnitude of the calculated change in modulus using the other parameters is in excellent agreement with experiment (Table III). Since the fractional change in modulus is proportional to B^2, the coefficients of proportionality are tabulated.

The fractional change in loss factor (Figure 11) does not appear dependent on density, but it does demonstrate a dependence on the square of the magnetic field as predicted.[60] The theory predicts an inverse dependence of the change in loss factor on the product of the conductivity and square of the sound velocity and Fermi velocity. This is in agreement with the scaling of the respective data at any one field value, within the uncertainty of the Fermi velocity for that material. A calculation of the predicted fractional change in loss factor using the other parameters is in reasonable agreement with the experimental data (Table IV). Only the polycrystalline data has been presented here for a comparison between different materials to bypass the problems associated with single crystal orientations and their associated elastic constants.

TABLE III

MODULUS COEFFICIENT OF LONGITUDINAL B^2 TERM

Material	Theoretical (10^{-14} Oe^{-2})	Experimental (10^{-14} Oe^{-2})
Al	8.7	10.1
V	5.8	7.5
Nb	5.4	6.8
Ta	4.3	4.5

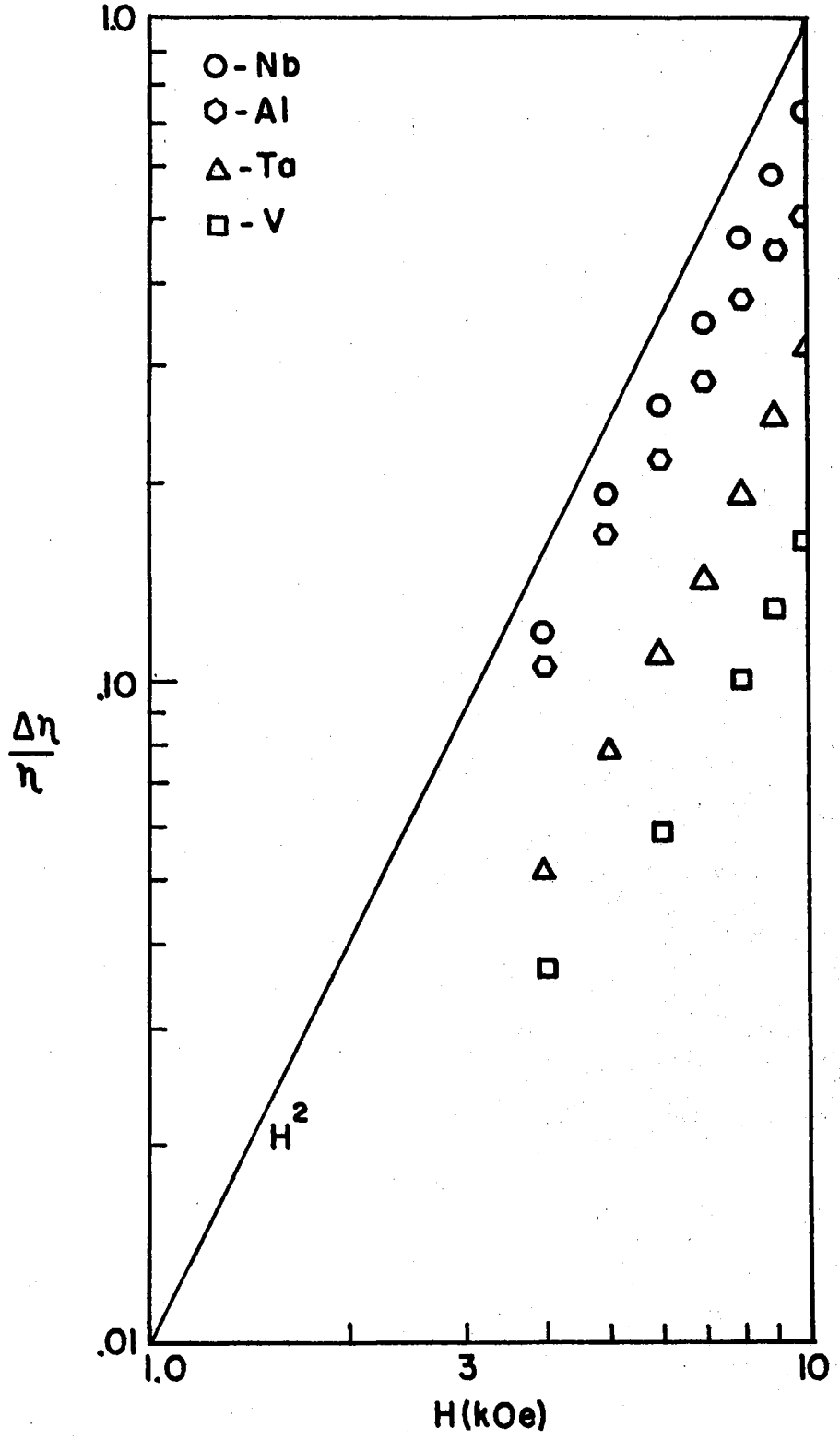

Figure 11. Longitudinal Loss Factor Changes

The polycrystals should give an average value for each material for all parameters.

Other materials (Pb, Sn, and some PbSn and PbIn alloys) were investigated, but did not exhibit a sufficiently high Q to have an accuracy of measurement comparable to the samples mentioned above in either the longitudinal or the torsional modes. Also, measurements made at 300°K and above the superconducting state in magnetic field at 4°K were not sufficiently different to merit separate attention. While the Q increased with decreasing temperature causing better resolution with a smaller loss factor, the relation between samples was unchanged. The conductivity did increase with decreasing temperature and led to a smaller fractional change in loss factor, but little difference in the fractional change in modulus was noted. This is in agreement with the theory and points out the fundamental differnce of the harmonic and anharmonic components of the complex elasticity.

The torsional mode data is consistent with existing theory in form, but not in magnitude.[58,60] The fractional change in modulus varies as the square of the magnetic field and inversely as the density as seen in Figure 12. A similar theoretical dependence to the longitudinal mode is suggested by experiment, but is found to be two orders of magnitude below the observed data. The functional dependence is well substantiated, and only the proportionality constant needs modification. An empirical equation fitting the data to the functional dependence suggest

$$\frac{\Delta\mu}{\mu} = E\frac{B^2}{\rho v^2} .$$

where E is a dimensionalless quantity in Gaussian units found empirically

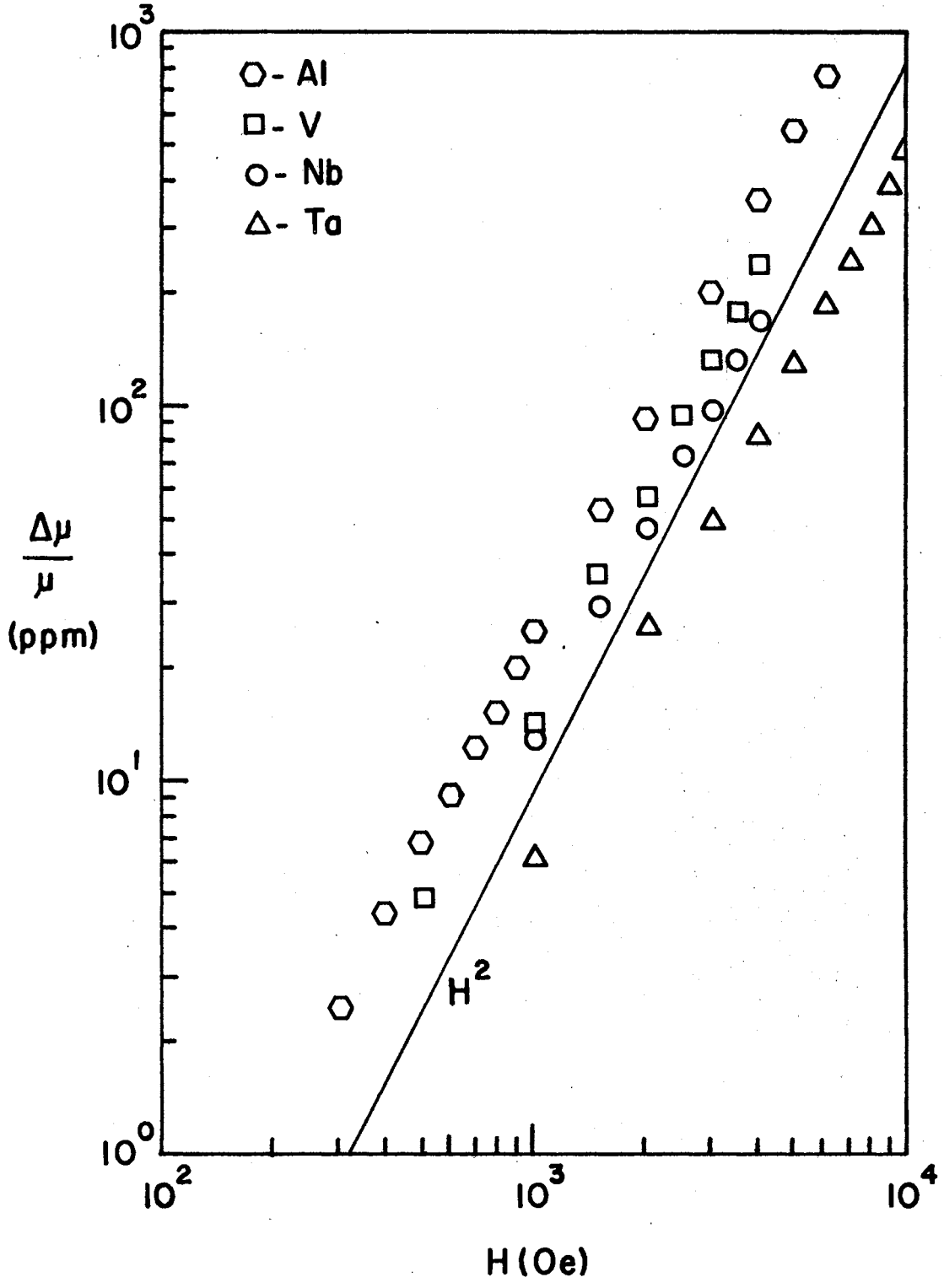

Figure 12. Torsional Modulus Changes

as given in Table V. Also noted in this table is a scaling between

TABLE IV

LOSS FACTOR COEFFICIENT OF LONGITUDINAL B^2 TERM

Material	Experimental (10^{-9} Oe^{-2})	v_F Calculated (10^8 cm/sec)
Nb	7.2	1.67
Al	5.4	1.53
Ta	3.2	3.52
V	1.6	4.00

TABLE V

MODULUS COEFFICIENT OF TORSIONAL B^2 TERM

Material	E	f/σ (Hz-ohm-cm)	Epv^2 (10^{-6} Oe^{-2})
Ta	4.1	0.85	4.9
Nb	5.5	0.80	12.5
Al	6.8	0.99	17.0
V	7.3	1.05	24.0

samples for the frequency divided by the conductivity. However, substituting this into the equation for the shear velocity dependent on the square of the magnetic field leads to a gross error in magnitude, compared to the experimental data,

$$\frac{\Delta\mu}{\mu} = \frac{fB^2}{8\pi\sigma pv^2} .$$

The theory of Rodriguez[59] indicates a negligible contribution due to conductivity and otherwise agrees with the longitudinal prediction. This is at least one order of magnitude below the experimental results. Later in this section it will be shown that dislocations can contribute to the elastic changes under consideration. This difference between theory and experiment is attributed to dislocations.

The fractional change in loss factor for the torsional mode also retains a dependence on the square of the magnetic field (Figure 13). These values are approximately one order of magnitude higher than the longitudinal changes, but the torsional values seem to scale with frequency, which was not noted by the longitudinal theory. Assuming a form for the fractional changes,

$$\frac{\Delta\eta}{\eta} = D\,B^2 ,$$

then the D for each material may be compared (Table VI). Since there is no existing theory for the loss factor of the torsional mode, the empirical constant above cannot be computed theoretically for comparison. The similar behavior of the torsional and longitudinal data indicates an analogous calculation to the longitudinal is needed for the torsional and is left to the theoriticians.

Only the polycrystalline data has been presented here for comparison to alleviate the problems connected with single crystal anisotropy. One interesting anisotropic behavior did occur in single crystals of Nb in the normal state at 300°K, 77°K, and 4°K. The orientation dependence of the magnetic field on the fractional changes in elasticity over a 3 KOe field increment was studied for single crystals oriented with the

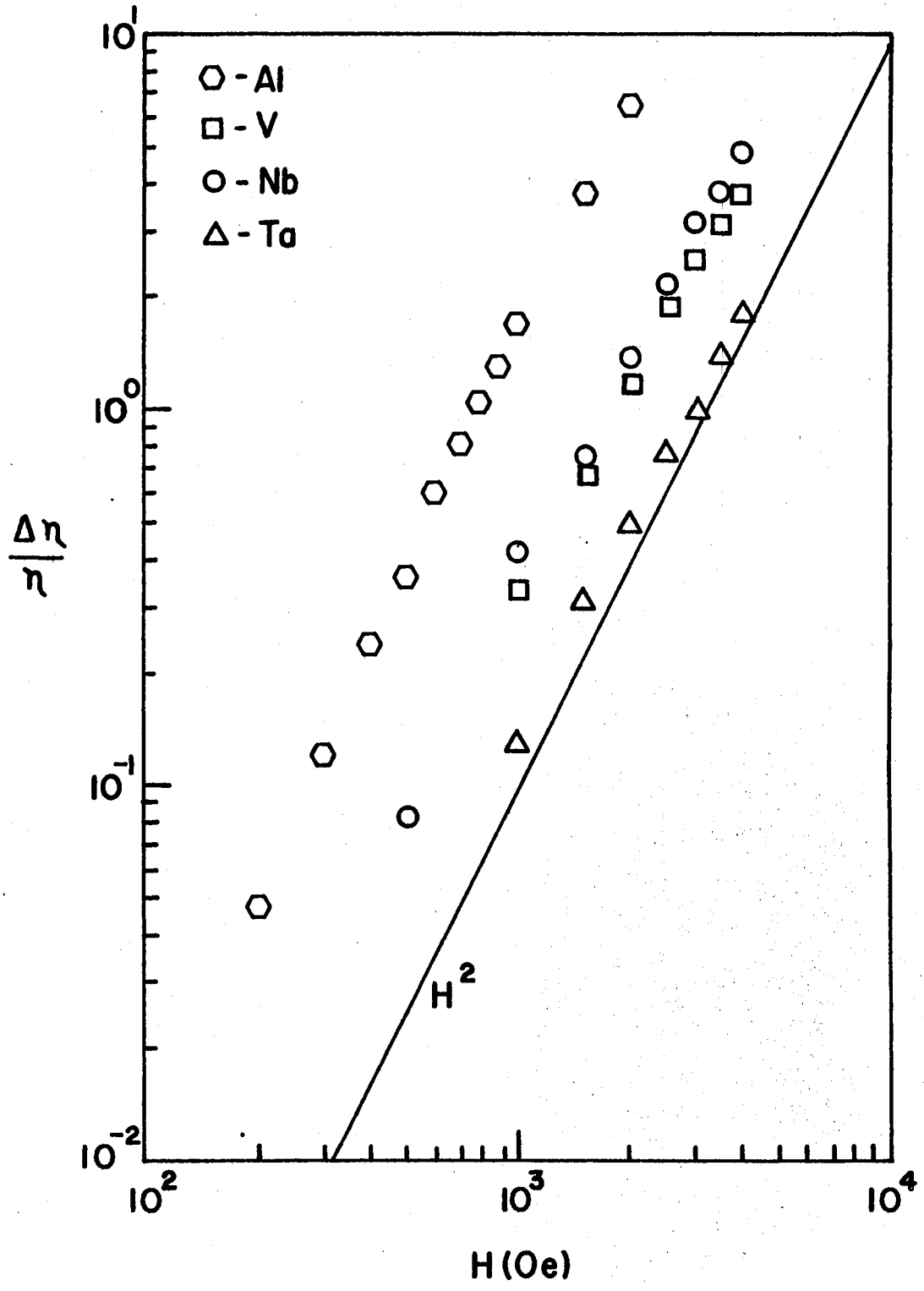

Figure 13. Torsional Loss Factor Changes

major slip direction [111] along the long axis of the cylinder and parallel to the propagation direction. The anisotropy occurred in the shape of two major lobes for each mode of propagation (Figure 14).

TABLE VI

LOSS FACTOR COEFFICIENT FOR TORSIONAL B^2 TERM

Material	$D(10^{-7}\ Oe^{-2})$	f(kHz)
Ta	1.25	26.3
V	2.93	28.0
Nb	3.50	29.1
Al	16.1	33.3

Several possible explanations were investigated. The torsional mode electrode drive system causing the anistropic behavior was the original assumption, but this was proven incorrect, since only the (111) oriented samples demonstrated this property, and the orientation of the torsional notches was in no way related to the position of the lobes from one sample to the other. It was also noted that the longitudinal anisotropy was detected prior to the notching of the sample for the torsional mode excitation. The anisotropic behavior in the sample of low purity (RRR = 55) was removed by deforming the surface of the specimen, while the longitudinal anisotropic behavior remained (Figure 15). This suggest that the torsional mode senses surface effects dominantly, since the torque is greatest there and the damage was most severe in that region. The longitudinal mode sensed all of the cross-sectional area and sensed the anisotropy even after surface damage was incurred.

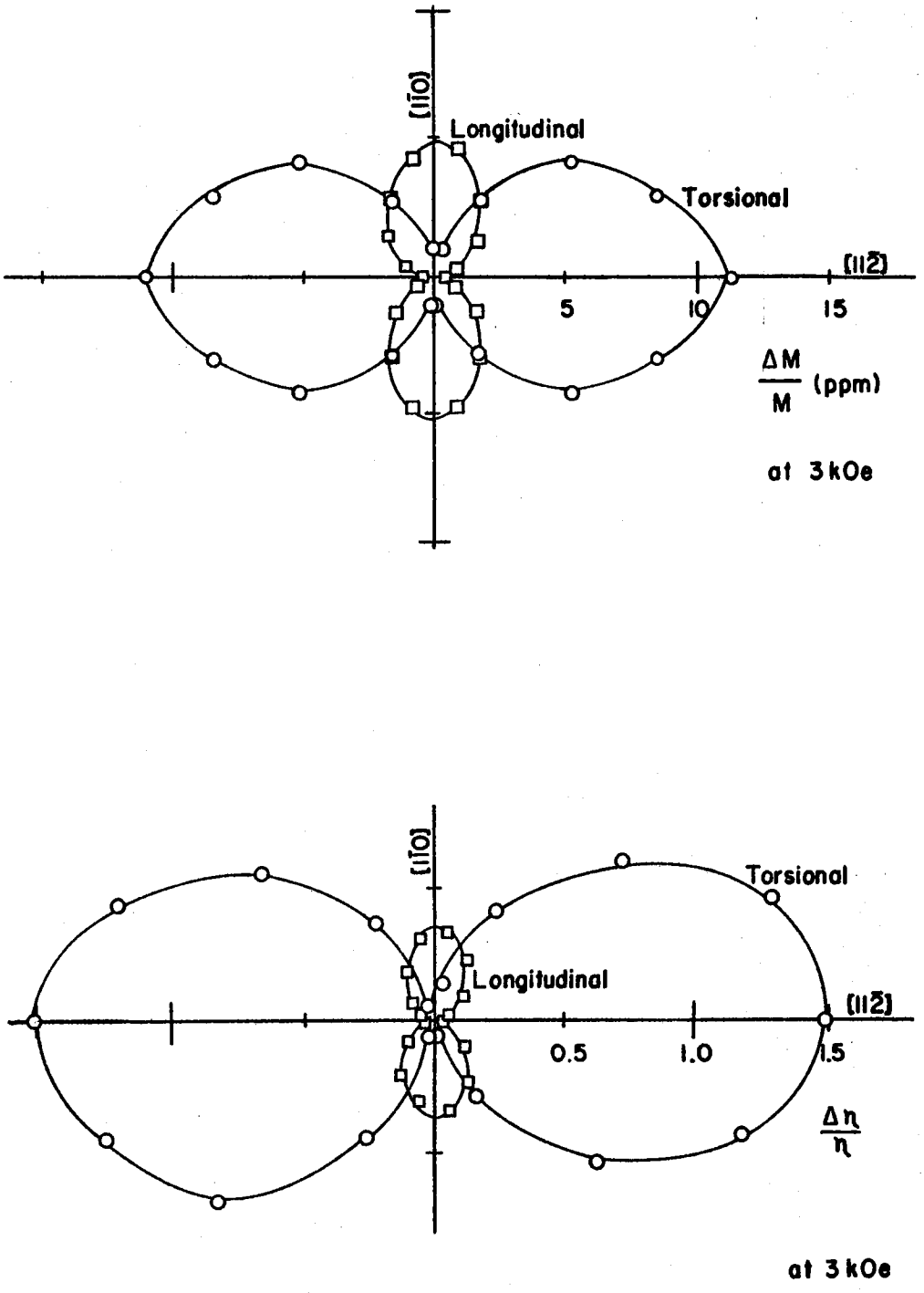

Figure 14. Dislocation Lobes Originally

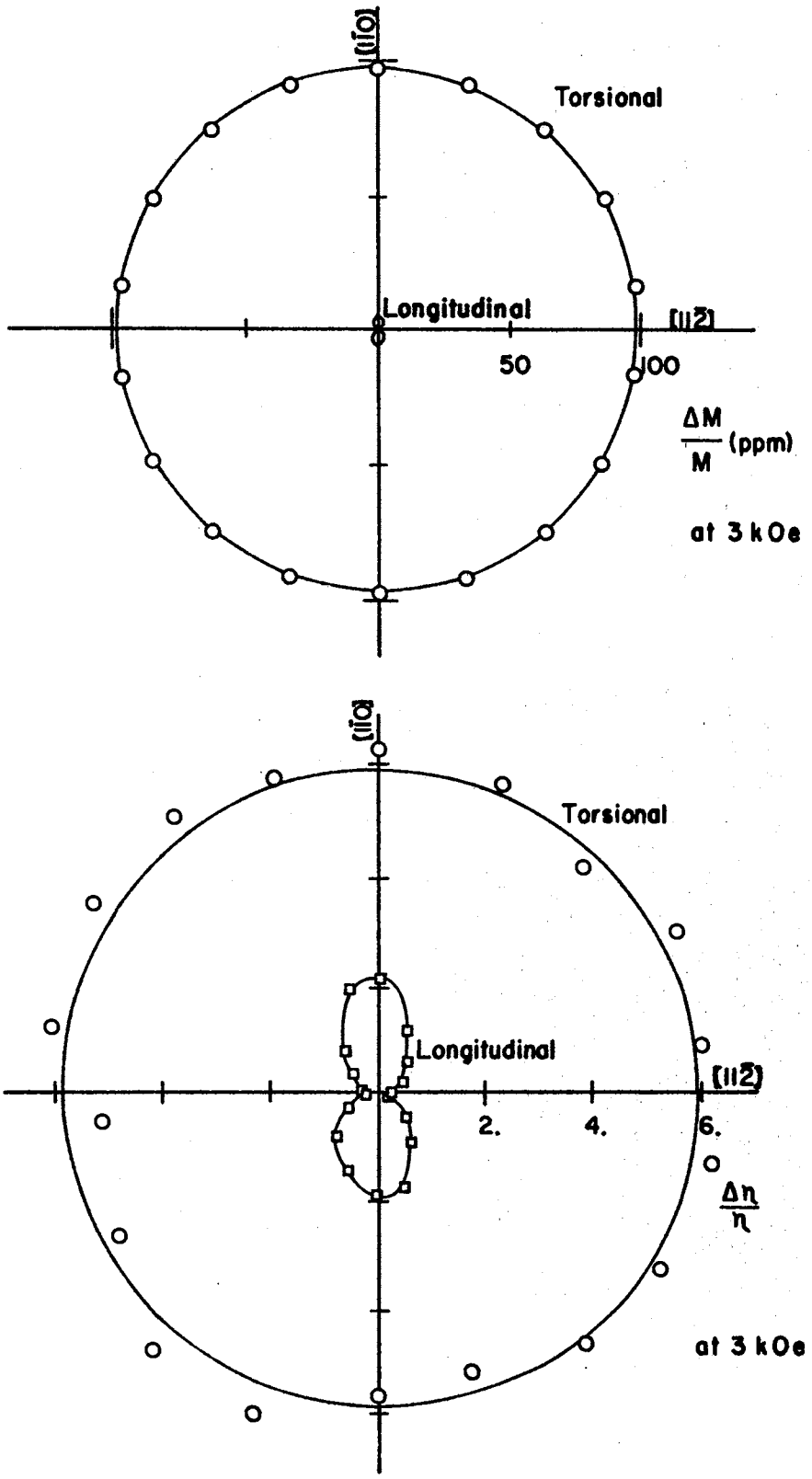

Figure 15. Dislocation Lobes After Deformation

The crystalographic orientation of the lobes for each mode suggest a connection of the anisotropy with dislocations. The torsional lobes were observed with the magnetic field oriented along the [112] direction, while the longitudinal lobes defined the [110] direction. Dislocation theory[148] predicts a static elastic field deformation due to the presence of a dislocation line that is proportional to sin θ, where θ is the angle measured from the dislocation direction. The interaction of this deformation field with the magnetic field is not clear, but appears to be in some way related. The primary slip plane is a wavy (110) for b.c.c. metals,[48] i.e., a (110) jogging to a parallel (110) repeatedly. This sometimes leads to other minor slip planes as defined by the job directions. The stresses related to the predicted deformation field imply a longitudinal stress proportional to sin θ and a torsional stress proportional to cos θ. Since the observed lobes were 90^{o} out of phase with the longitudinal lobes alligned along a [110] direction, the connection between the lobes and dislocations is possible.

An annoying feature is that the [110] directions are three fold in the (111) plane and only one set of lobes was observed along a [110] direction. This suggest that all dislocations in this sample were oriented along one preferred [110] direction when the specimen was grown. While this could be possible, it is not highly probable for the two specimens prepared at different locations by different people using different equipment. Another possibility is that once a dislocation is formed that the associated deformation field allows only parallel dislocations to form. These parallel dislocations are then pinned by interconnecting jogs.

A further implication that dislocations maybe responsible for the

anisotropy is found by looking at the minimum value the longitudinal lobes reach. This value is the theoretical value of the longitudinal mode as described previously. All other values in directions sensing the deformation field are greater due to the presence of dislocations. This is also substantiated by the superconducting data showing a fluctuation effect due to the presence of dislocations in these same samples.[166]

Superconducting State

The superconducting work has been in part already reported for the longitudinal mode,[81] and a theory given to relate the fractional change in elasticity to the normal volume fraction in the mixed state. The use of the elastic parameters to study the superconducting state was substantiated by comparison with the magnetization changes in the superconducting state. The magnetization for Type II materials exhibits a change in slope at H_{C1}, as does the elastic modulus. The loss factor shows no change at this critical field. At H_{C2} the magnetization reaches the normal state magnetization by a nearly asymptotic approach, while the modulus again shows a sharp change in slope. The attenuation in high purity samples also shows a sharp change in slope at H_{C2}, but shows little change in lower purity materials. The magnetic susceptibility is closely related to the fractional change in modulus throughout the superconducting state. The susceptibility is minus one, or diamagnetic, in the superconducting state and changes proportional to the volume of material that returns to the normal state, ending at the normal state value at H_{C2}. The normal state value for Nb is slightly positive, or paramagnetic.[169] Kramer and Bauer[76] have shown that the fractional

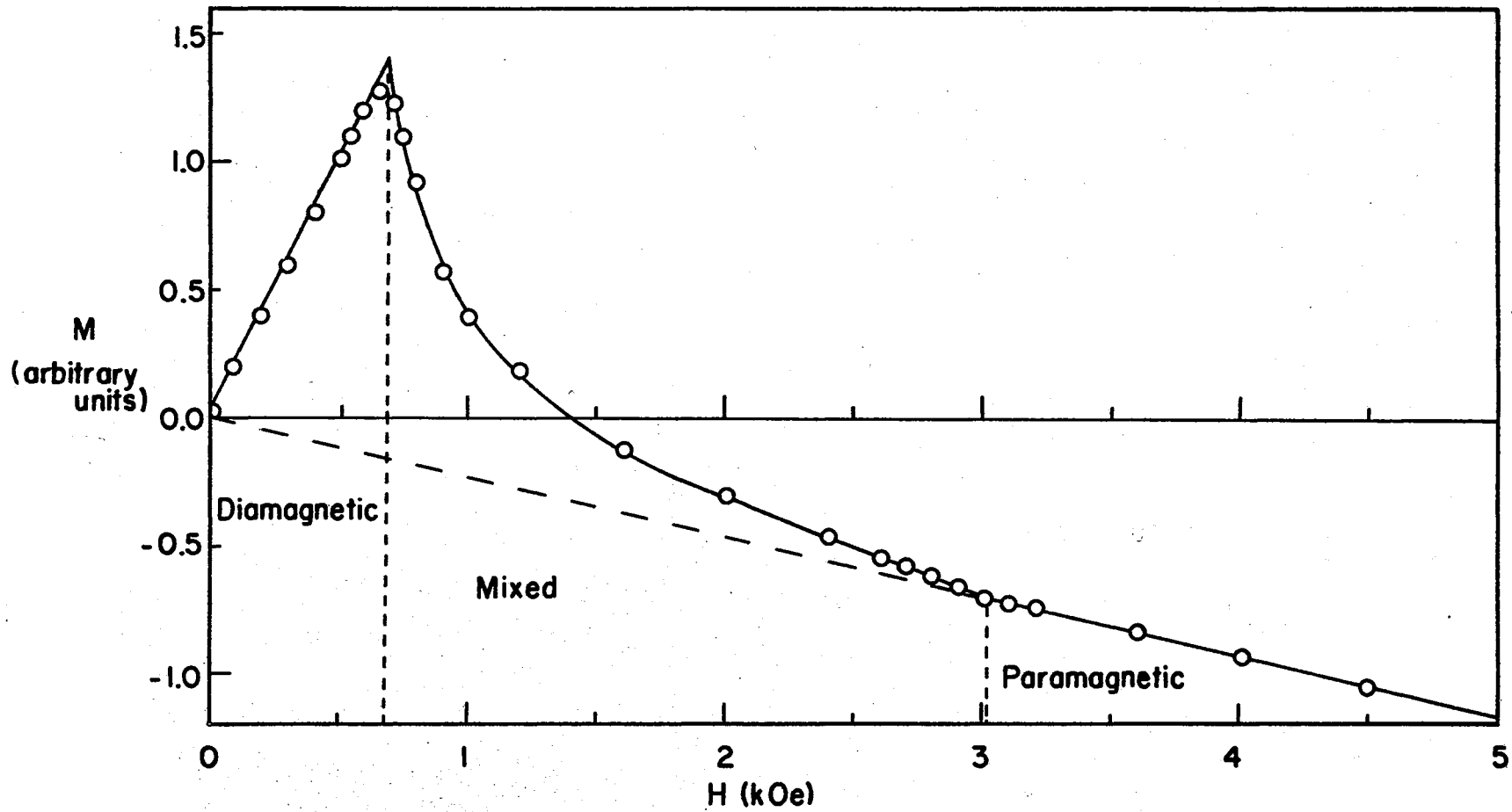

Figure 16. Magnetization at Superconducting Transition

change in modulus curve is analogous to the magnetization curve as a justification for elastic measurements to be used in superconductivity studies. A typical magnetization measurement is shown in Figure 16.

The better known Type I materials have been found to exhibit a linear dependence in modulus throughout the intermediate state.[81] Due to the demagnetization factor of 1/2, the intermediate state is observed in this investigation from $H_c/2$ to H_c. This is in agreement with the laminae model of flux penetration in Type I superconductors and a linear normal volume change between the two end states (Figure 17). The sharp changes in slope are easily recognized as the critical fields in the modulus data. The attenuation data showed no significant behavior, since these samples were not of high purity.

To advance the understanding of the behavior of Type II superconductors was the purpose of this study, and Nb was the principle material investigated. A study of the fractional changes in the elastic parameters as a function of temperature below $4^{\circ}K$ exhibited an internal friction peak in the loss factor around $3.1^{\circ}K$ in agreement with a similar peak reported by Kramer and Bauer[76] (Figure 18). The modulus shows a ripple in this region, also, which is characteristic of internal friction peaks. The modulus generally follows a decreasing slope with decreasing temperature in the superconducting state in agreement with the thermodynamic reasoning that the total change in stiffness across the superconducting state should increase with decreasing temperature below the critical temperature.[5] The normal state stiffness increases with decreasing temperature and approaches zero temperature with zero slope.

The stiffness data for all Type II samples is presented in Figure 19, showing the general features compared between samples. The modulus

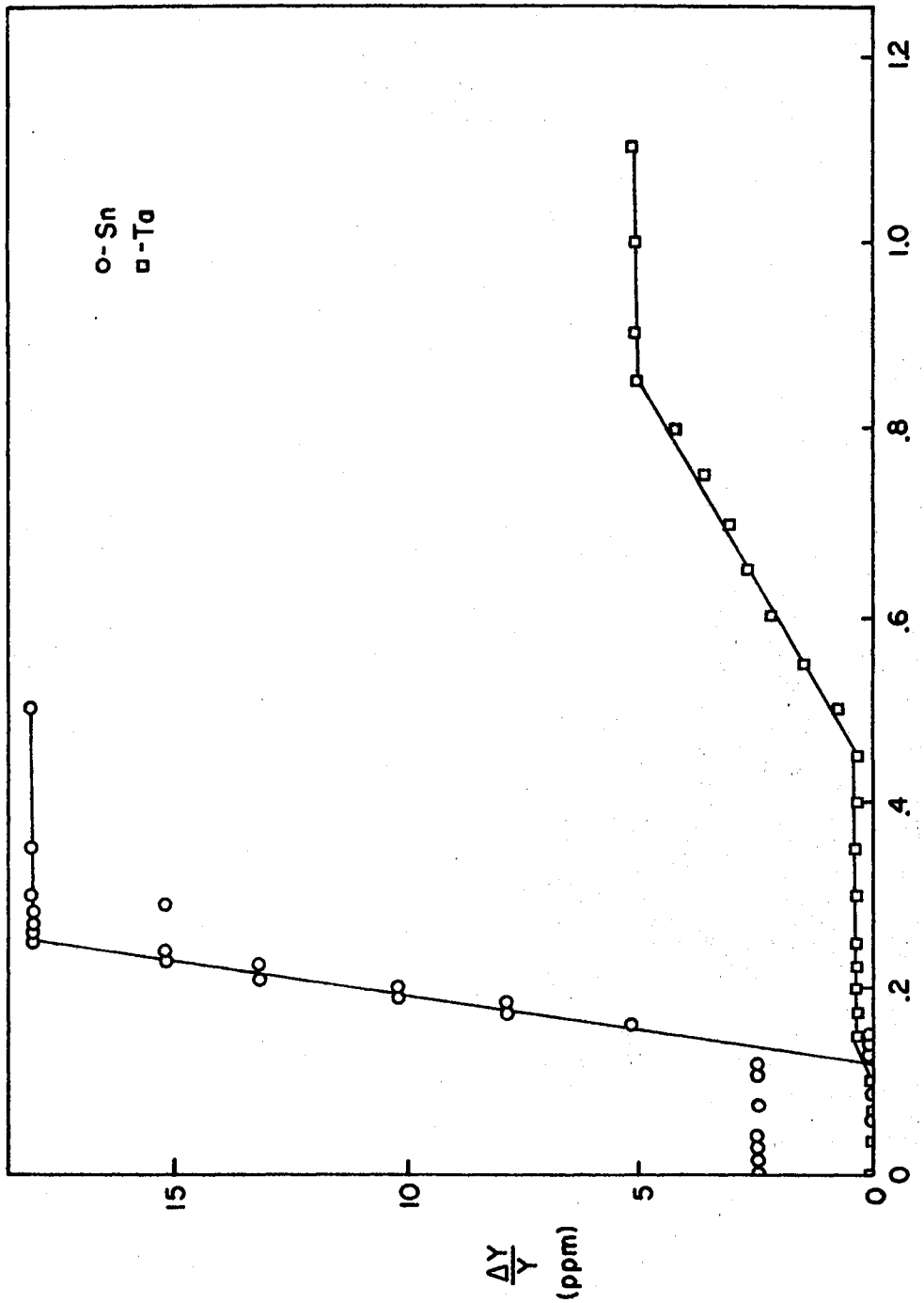

Figure 17. Type I Longitudinal Modulus Transition

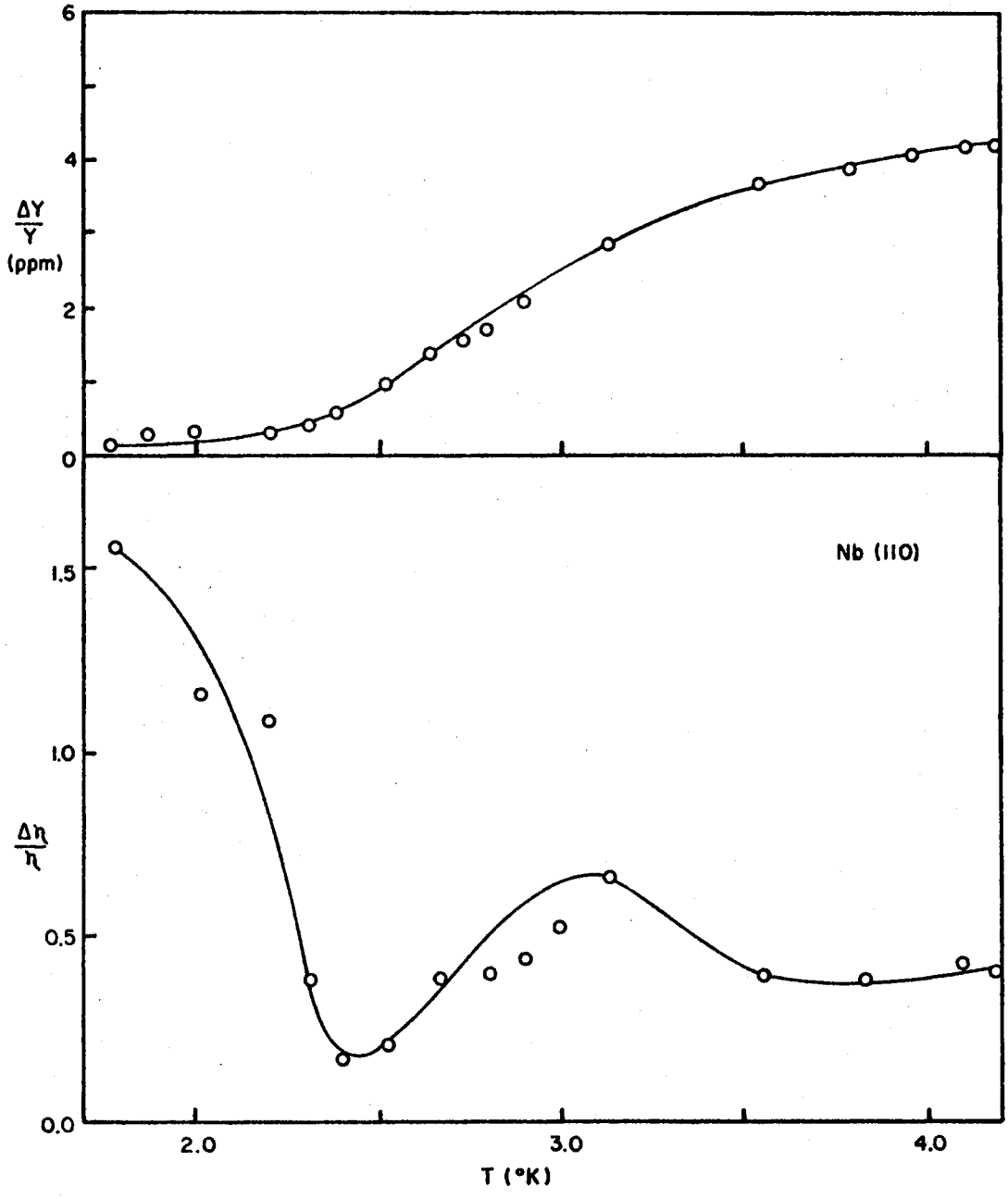

Figure 18. Internal Friction Peak

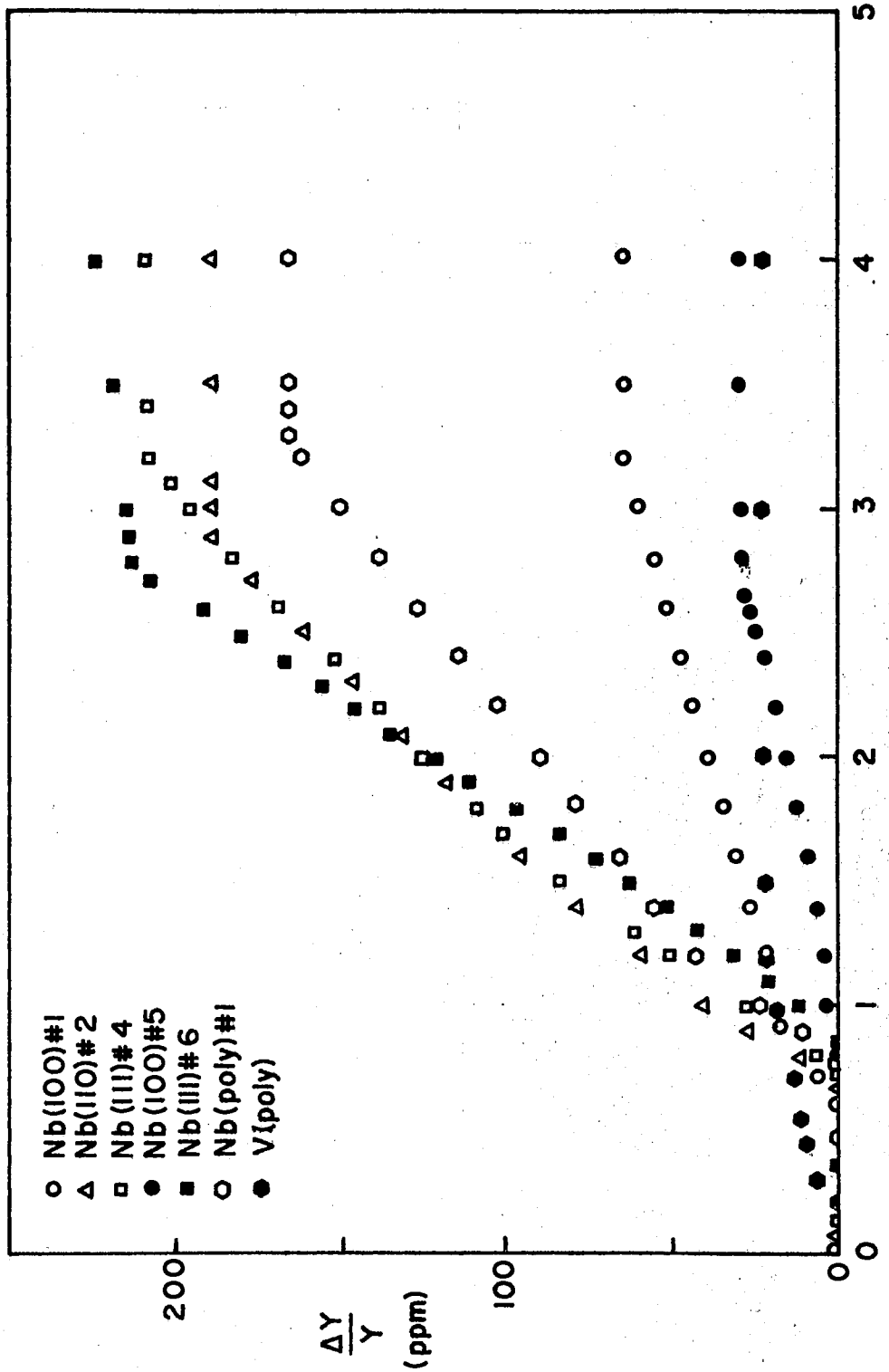

Figure 19. Type II Longitudinal Modulus Transition

remains constant in the superconducting state up to $H_{C1}/2$ at which point magnetic flux penetrates the sample. A rapid rise in modulus is noted in the intermediate state, which joins with a gentler rise in the mixed state. The data is not linear, as in the Type I data, but does reflect a dependence on the normal volume fraction.[81] A return to a nearly constant modulus is characteristic of the longitudinal modulus at H_{C2}. The magnetic field dependence of the stiffness at H_{C2} is so small for this mode that no correction is made for it. An important feature of this data is the residual stiffness after cycling the field above H_{C2} and back to zero field. The residual stiffness indicates the amount of trapped flux and, therefore, gives an indication of the number of flux pinning points in that sample. As the external field decreases and the vortex separation increases,[81] the repulsion between vortices can become less than the attractive pinning forces of imperfections, thus trapping the remaining vortices. The higher residual stiffness of the polycrystalline sample indicates that dislocation and grain boundaries are more effective in trapping vortices than are impurities. The residual stiffness increases as the temperature is decreased and infers that the number of pinning points increases inversely with temperature. The vortex separation and density can be calculated for the observed residual stiffness state and used to give an indication of the dislocation density. Table VII summarizes the important features of this data for each sample.

It seems unusual that the high purity Nb (100) #5 sample exhibited such a small total change in modulus. This small change in stiffness was also found at a lower temperature ($1.8^{\circ}K$) and indicated that it was not associated solely with temperature. Deformation (5%) of the sample did not change the low value appreciably. It was noted that the frac-

TABLE VII

FEATURES OF LONGITUDINAL MODE OF TYPE II MATERIALS

Sample ($T = 4.2^{\circ}K$)	$H_{C1}/2$ (KOe)	H_{C2} (KOe)	$(\Delta Y/Y)_{TOT}$ (ppm)	$(\Delta Y/Y)_{RES}$ (ppm)	Residual Percentage	RRR
Nb (100) #1	0.650	3.20	65.	7.0	11.	30.
Nb (110) #2	0.700	2.90	191.	17.	9.	86.
Nb (111) #4	0.720	3.00	203.	18.	9.	55.
Nb (100) #5	0.800	2.65	26.	8.4	32.	2500.
Nb (111) #6	0.850	2.70	215.	60.	28.	2500.
Nb (poly) #1	1.01	3.40	175.	58.	33.	47.
V (poly) #1	0.180	1.20	20.	3.4	17.	17.

tional change in loss factor decreased just above H_{C2}, which was also as unusual feature in this sepcimen (Figure 20). Since both the small stiffness change and a decreasing loss factor above H_{C2} are unusual for this specimen, they may be caused by the same mechanism. If an internal friction peak occurred for this sample in this temperature range which can be activated by a magnetic field, then the decrease in field dependence of the loss factor could indicate resonant absorption, which is also limiting the stiffness change.

Apart from this unusual occurrence in the total change in modulus of the Nb (100) #5 sample, a dependence of the total change in modulus for the Nb set of samples was sought. Upon comparison of all the associated parameters, a relation was found between the electrical conductivity, or electronic mean free path, and the total change in modulus (Figure 21). It appears that the total change in modulus approaches a limiting value at high conductivities and is approximately linear for low conductivities. Since it is known that the superconducting coherence length follows.[176]

$$\frac{1}{\xi(\ell)} \doteq \frac{1}{\xi_o} + \frac{1}{\ell_e} ,$$

an interpretation relating the superconducting change to the electronic mean free path seems plausible. An analysis of the above equation shows that for high conductivities or long ℓ_e, the coherence length is changed in little or no way by a small change in ℓ_e. At low conductivities where $\ell_e < \xi_o$, the coherence length is dominated by the conductivity and would follow approximately linearly with it. This low conductivity feature was reported earlier when only the low conductivity samples were under

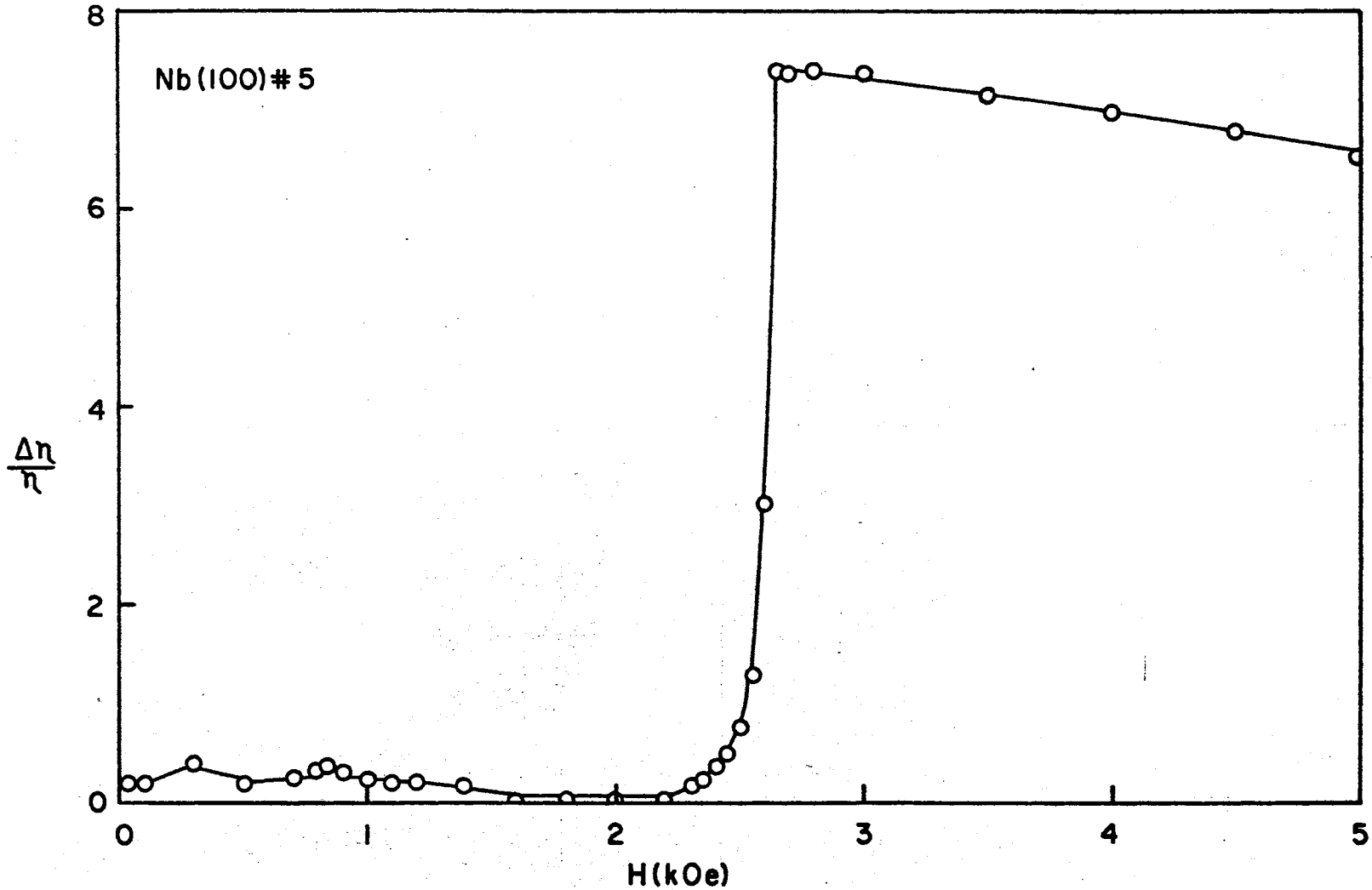

Figure 20. Decreasing Loss Factor Above H_{c2}

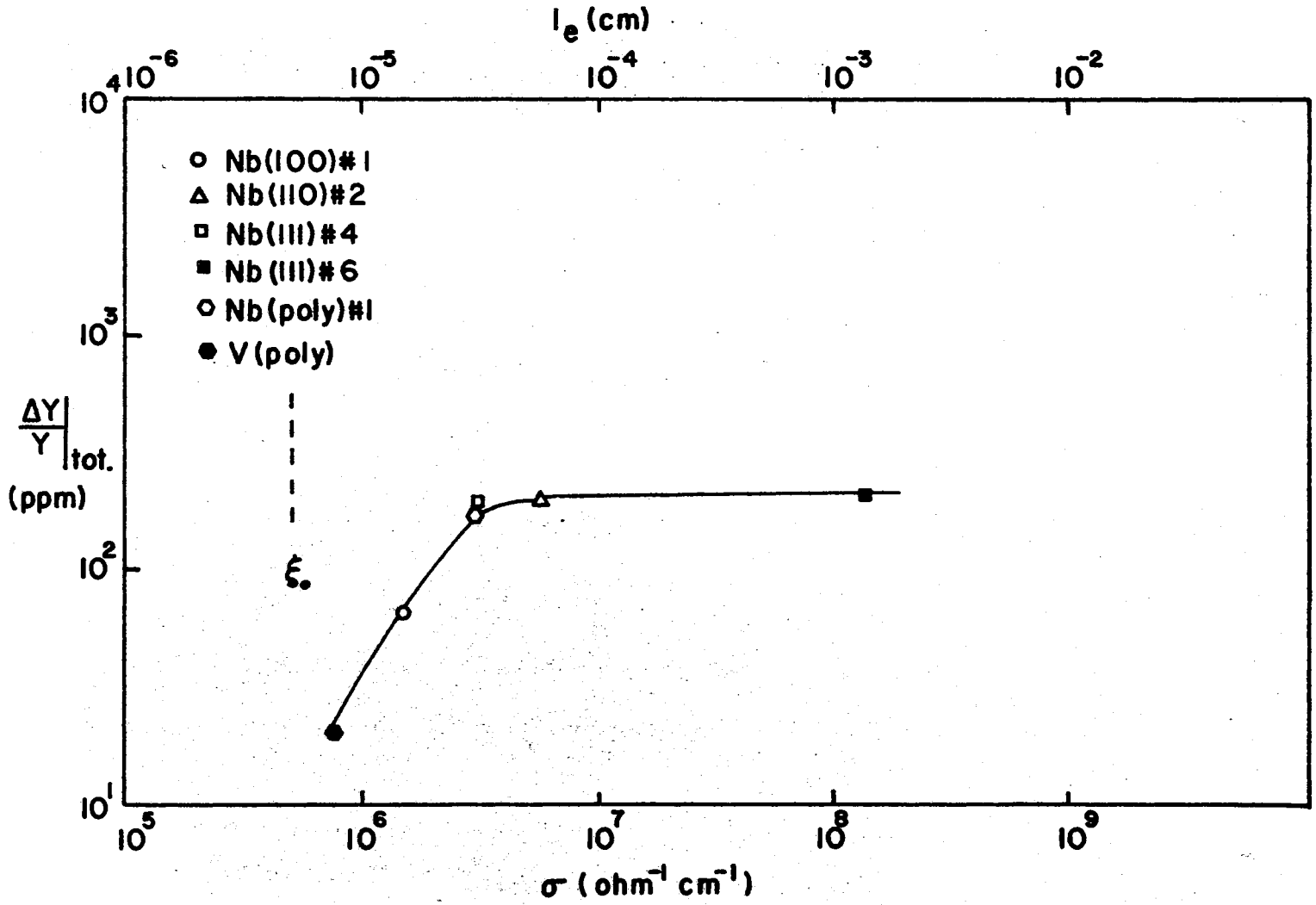

Figure 21. Total Modulus Change Versus Conductivity

study. This might be interpreted that the vortex interactions of the superconducting state cease to be controlled by impurity sights as ℓ_e approaches ξ_o, and that the vortex self-interactions begin to control the modulus change. It should be noted that Nb was particularly sensitive to this situation, since $\lambda = \xi$.[177] Thus, in extreme Type II materials ($\lambda > \xi$), the changes should be limited to smaller values than for Nb as the vortex self-interactions limit the modulus change. Since $\lambda < \xi$ defines a Type I material and this interpretation is limited to the Type II materials, $\lambda = \xi$ is a limiting case in this interpretation.

The fractional change in loss factor was generally not an accurate enough measurement to observe any changes in the superconducting state. This seemed to be a function of purity principally. The loss factor itself could be very low (10^{-7} nepers/radian) and no changes observed, or it could be relatively high and large changes seen (Figure 22). Impurities limit the electronic mean free path and seem to obscure the electronic transition from the superconducting state to the normal state (RRR = 80), even though the characteristic decay time for 60 dB of voltage is several minutes. Thus, the lattice background attenuation is very low. The high purity samples (RRR = 2500) show a large electronic transition, but the electronic attenuation in the normal state is very high and obscures any lattice attenuation features. The combination of both types of crystals leads to much more information about the total attenuation.

The torsional mode measurements have in general agreed with many of the ideas that were presented for the longitudinal mode. The Type I transition is linear for this mode also, as seen in Figure 23, and demonstrates the same general features at the critical field points and

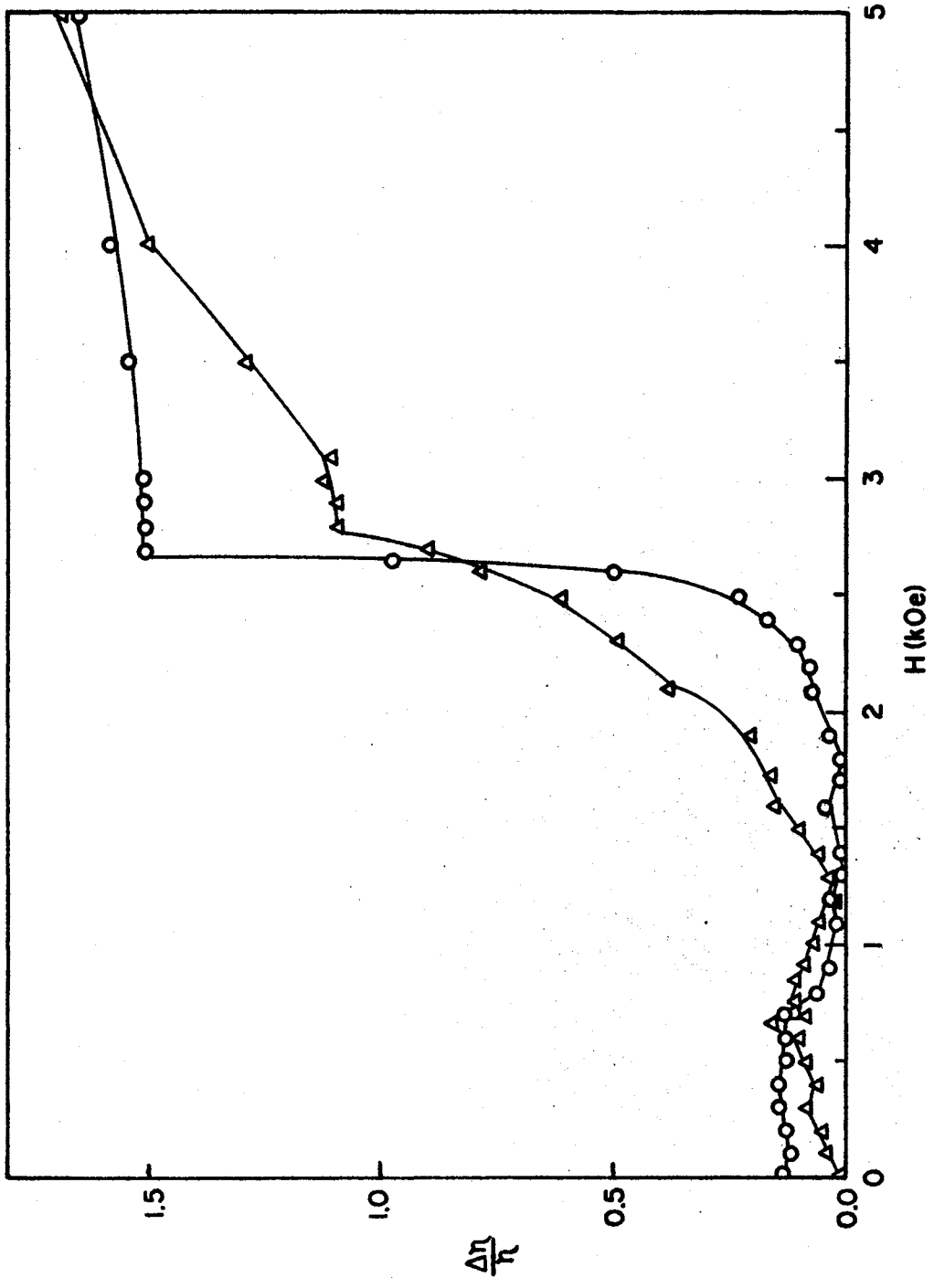

Figure 22. The Electronic Transition

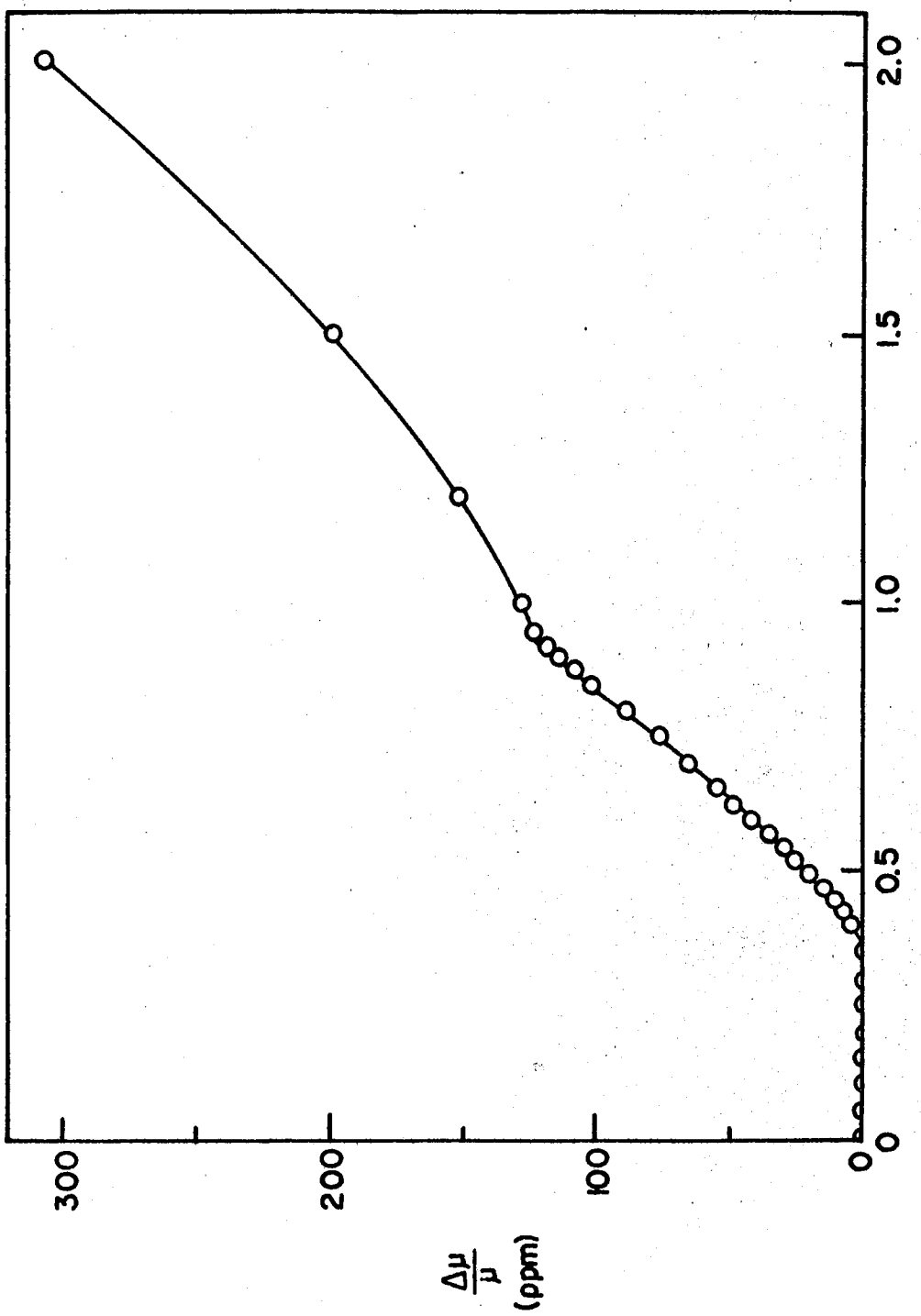

Figure 23. Type I Torsional Modulus Transition

in residual modulus. The behavior above H_{C2} is more strongly field dependent and necessitates a correction for the additional normal modulus at H_{C2}. This correction is accomplished by fitting the upper field data above H_{C2} to the predicted squarred dependence on field by a least squares method and then extrapolating the normal state curve back to zero field. This extrapolated value of modulus change represents the value due only to the superconducting transition. The additional stiffness due to the normal volume fraction is given by

$$\mu = \mu(o) + AH_C^2 ,$$

since the laminae of Type I materials are normal and at local fields of H_C. Since the normal volume is a linear function of field in the intermediate state, the additional stiffness will add a linear function to a linear function and yield again a linear function as was observed experimentally. A is an adjustable parameter.

The Type II (Figure 24) materials exhibited a non-linear field dependence of modulus in the mixed state, but apparently not the same field dependence as the longitudinal mode. The strong field dependence above H_{C2} affected the modulus changes throughout the mixed state since the vortex core was always at H_{C2} and had to be corrected to obtain the total change in modulus due to the superconducting transition alone. The normal state dependence above H_{C2} was extrapolated back to zero field to give the correct total change for the superconducting transition. Also, the normal volume fraction dependence throughout the intermediate state could be determined from the longitudinal data and used to give the additional stiffness of the normal core of vortices in the intermediate region.

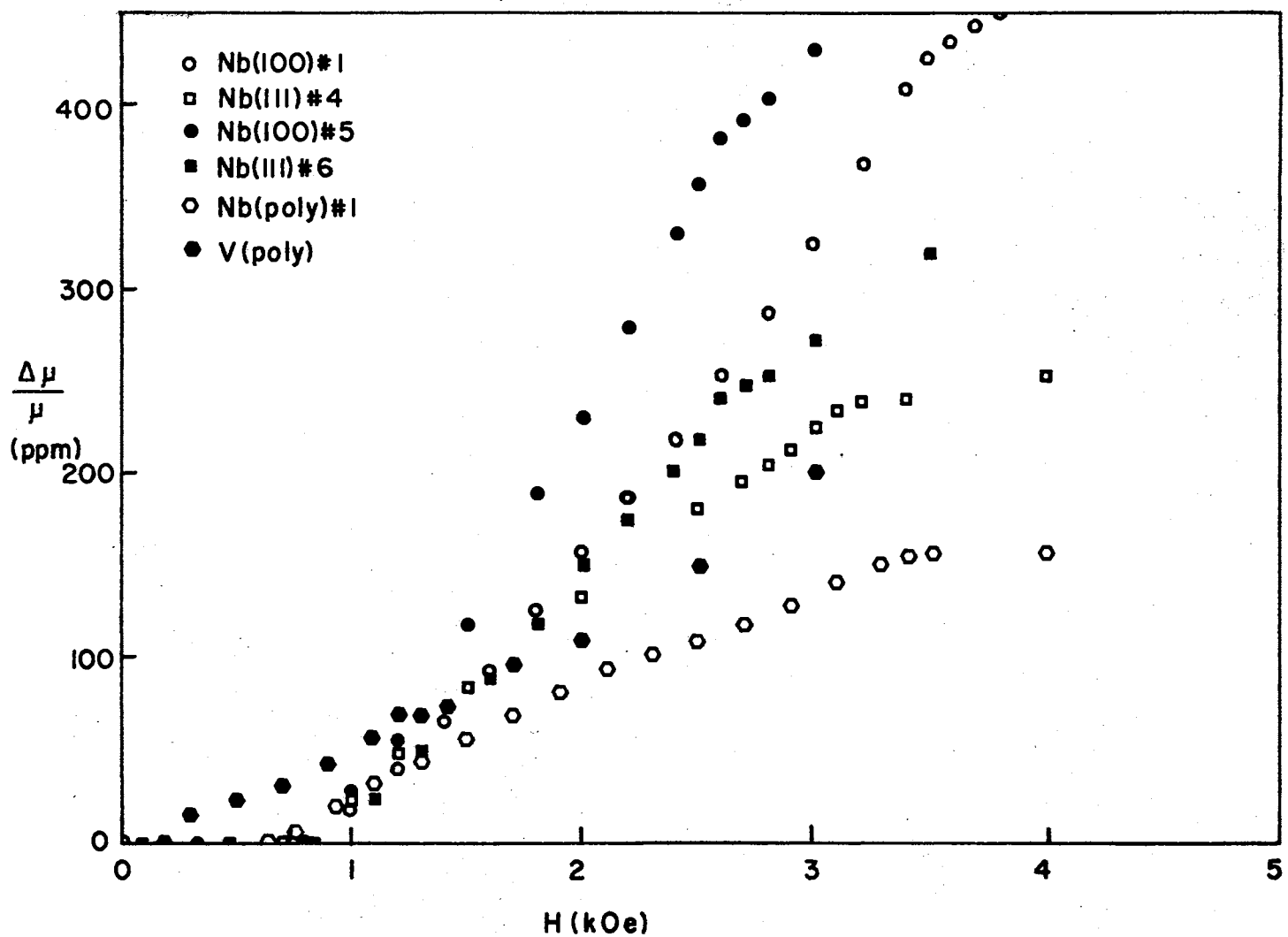

Figure 24. Type II Torsional Modulus Transition

$$\mu = \mu(o) + AH_{C2}^{2}$$

for this region, similar to the Type I materials but at H_{C2}. The modulus of the vortex is a constant, and the total change is affected by the volume of vortices only. Thus, this contribution is dependent on the normal volume fraction, and the total change of the shear modulus is dependent on the normal volume fraction in a way similar to the longitudinal mode. This can be seen by a comparison of the curvature of the data for both modes for samples where the high field data is a small contribution to the total change. The curvature of these graphs follows the same dependence throughout the mixed state, c.f., Nb poly #1. The important details of these plots are included in Table VIII.

TABLE VIII

FEATURES OF TORSIONAL MODE OF TYPE II MATERIALS

Sample ($T - 4.2^{o}K$)	$H_{C1}/2$ (KOe)	H_{C2} (KOe	$(\Delta\mu/\mu)_{TOT}$ (ppm)	$(\Delta\mu/\mu)_{RES}$ (ppm)	Residual Percentage	RRR
Nb (100) #1	0.750	3.40	193.	45.	23.	30.
Nb (111) #4	0.720	3.10	211.	32.	15.	55.
Nb (100) #5	0.850	2.65	234.	75.	32.	2500.
Nb (111) #6	0.850	2.65	130.	31.	24.	2500.
Nb (poly) #1	0.700	3.35	152.	14.	9.2	47
V (poly) #1	0.180	1.20	70.	30.	4.3	17

Notice that Nb (110) #2 sample is omitted from the torsional mode data, since the [110] direction does not have degenerate transverse modes,

and therefore does not support a simple torsional mode like the [100] and the [111] samples. The torsional residual stiffness increases with decreasing temperature as it did for the longitudinal mode, but it was found to be less in magnitude for polycrystalline samples than for the single crystal samples. This suggests that the torsional pinning points are not dependent on dislocation density in the same way as for the longitudinal mode. The total change in modulus did not follow a conductivity dependence as was found for the longitudinal mode.

A comparison of the number of vortices ($N\xi_o^2$) in the mixed state as a function of reduced magnetic field is given in Figure 25 for a high purity and low purity sample and for the longitudinal and torsional modes. The curves for the low purity sample are very similar to the original calculation[81] on the #2 sample, as shown in Appendix B (Figure 40). The reduced field parameter defines only the mixed state magnetic field range, since it is zero at $H_{C1}/2$ and one at H_{C2}. The purity of the two less pure samples is approximately the same, but the RRR of the #6 sample is two orders of magnitude higher. The peak in the number of vortices occurs at a higher reduced field value in the high purity case than in the lower purity case. The departure from the dashed line, which represents a non-expanding vortex, is more rapid for the high purity sample than for the low purity sample This means that the interaction of the vortices is greater at lower fields for the longer mean free path case. For a mean free path much greater than the coherence length the vortices sense each other, or interact, at low fields to reduce the otherwise equilibrium number of vortices and yet maintain a constant energy density. (This interaction of vortices in high purity samples was also suggested in the interpretation of the total longitudi-

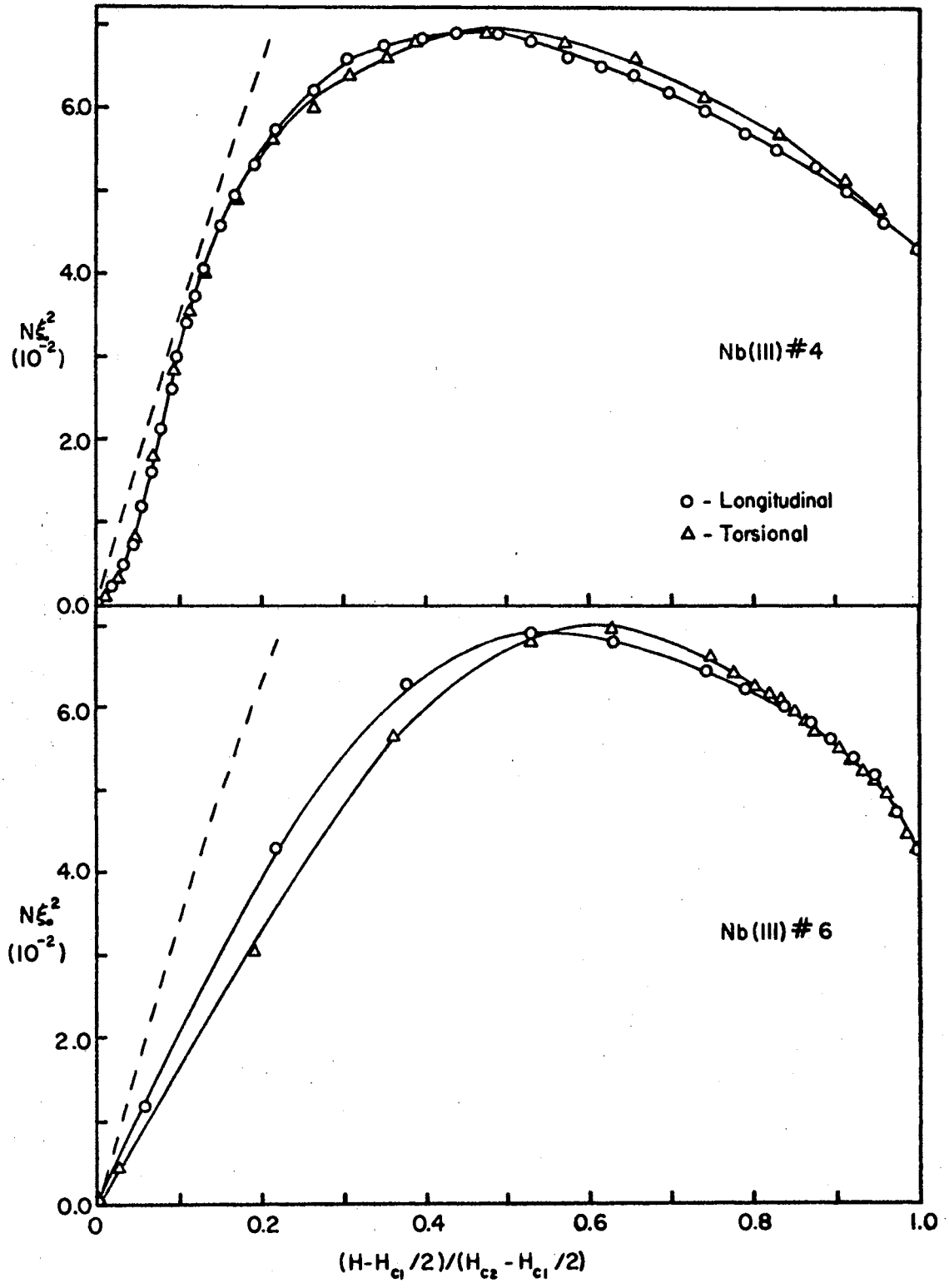

Figure 25. Number of Vortices in Mixed State of Nb

nal modulus change depending on conductivity (Figure 21).) The vortex interaction shifts the maximum of the number of vortices to a higher field value. It should also be noted that the longitudinal and torsional modes are very similar in each case. The longitudinal data peaks at a reduced field slightly below the torsional data, and a small difference is seen between these modes in the centeral range of the figure. This small difference is not sufficient to suggest a different interaction caused by the two modes.

The unusual behavior of the loss factor for the (111) samples proved intriguing. In Figure 26 the change in loss factor exhibits a large jump above H_{C2} which has been connected with a magnetic fluctuation effect via the change in electronic viscosity on dislocation motion.[166] The loss factor can be written as three separate components: (1) the lattice component η_L, (2) the electronic component η_E, and (3) the dislocation component η_D,

$$\eta = \eta_L + \eta_E + \eta_D .$$

The lattice part is subtracted out in the fractional change and the electronic transition occurs at fields $H \leq H_{C2}$. The dislocation part is left at and above H_{C2} and may be affected by transient superconducting pairs slightly above H_{C2}. The fractional change in modulus does not exhibit this effect due to its sensitivity only to the harmonic part of the elasticity and lack of sensitivity for dissipative processes. The modulus data can then be used to determine H_{C2} accurately and simultaneously for the attenuation data. The modulus data did show an anisotropic behavior in the normal state which was associated with dislocations and does exhibit an anisotropic field dependent behavior in

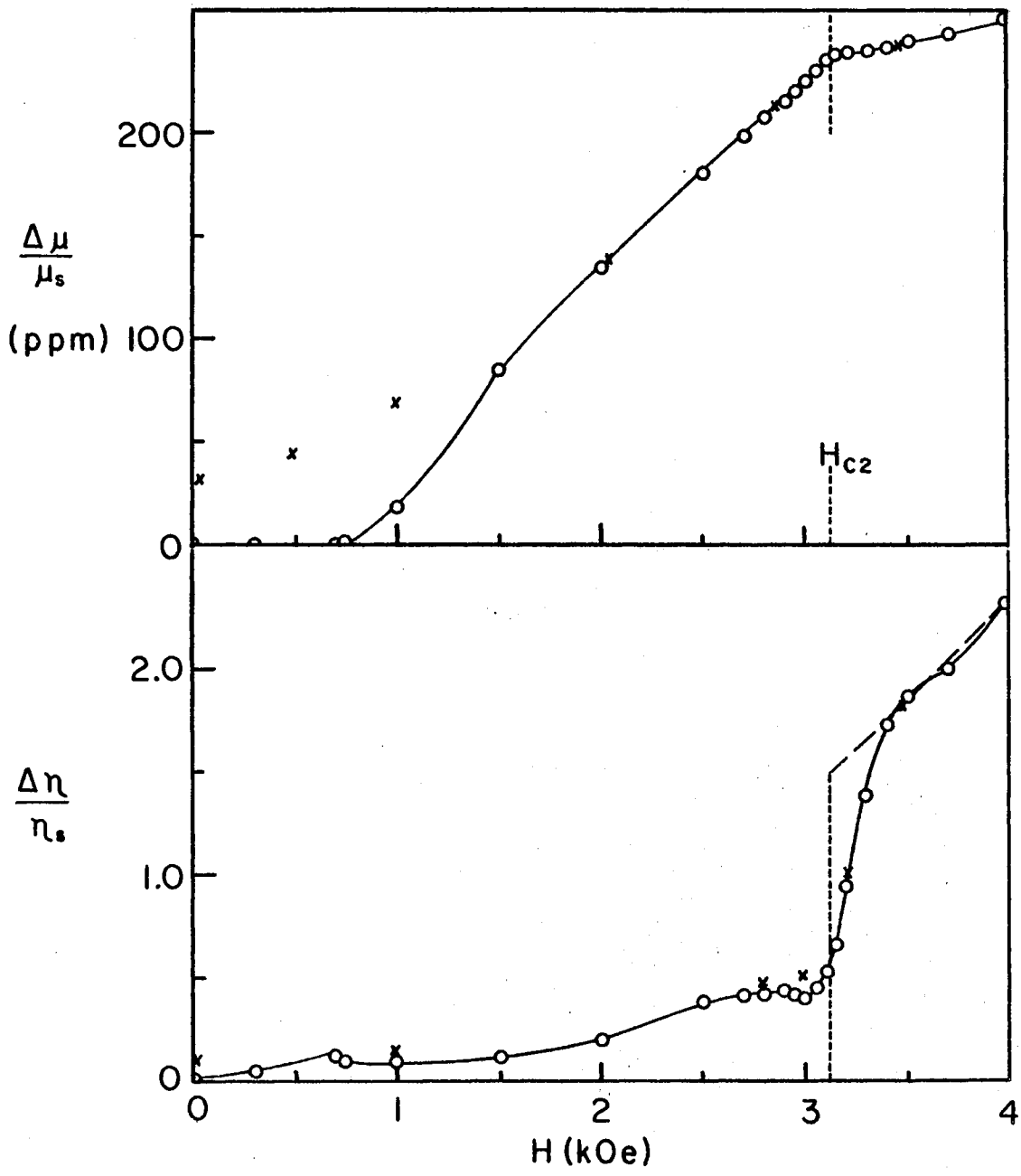

Figure 26. Dislocation Effect in the Loss Factor

the strength of interaction above H_{C2}, i.e., the slope above H_{C2} varies with orientation. Another indication that dislocations may be responsible for this unusual behavior is the observed amplitude dependence of the loss factor (Figure 27). Tittmann and Bommel[153] have shown that the superconducting transition can be quenched by dislocation motion at high strain amplitudes. This coupled with the internal friction peak observation around $3^{o}K$ make dislocations a plausible mechanism to explain this odd effect. The combination of low frequency excitation propagating in the major slip direction for Nb and the impurities obscuring the electronic transition have made this observation sufficiently large that it cannot be overlooked. A high purity sample was tested for this effect as originally received, after quenching from $1000^{o}C$ to room temperature in a few minutes, and after compresional deformations of 0.3% and 1.8% (Figure 28). The enhanced effect as a function of deformation strongly supports the dislocation explanation. Since the longitudinal mode also showed an anisotropic dependence in the normal state, this mode was checked after deformation of 1.8% and also exhibited a jump above H_{C2} (Figure 29). The lower purity sample in the longitudinal mode was not able to be measured due to the increased impurity attenuation at the higher fundamental frequency.

Resistivity

The resistivity data was taken as a means of relating these samples with other worker's samples. It was necessary to use a four-probe apparatus with electrostatic shielding to measure the low resistivity of the high purity samples. A typical plot of resistivity versus magnetic field at $4.2^{o}K$ is given in Figure 30. In the superconducting state the

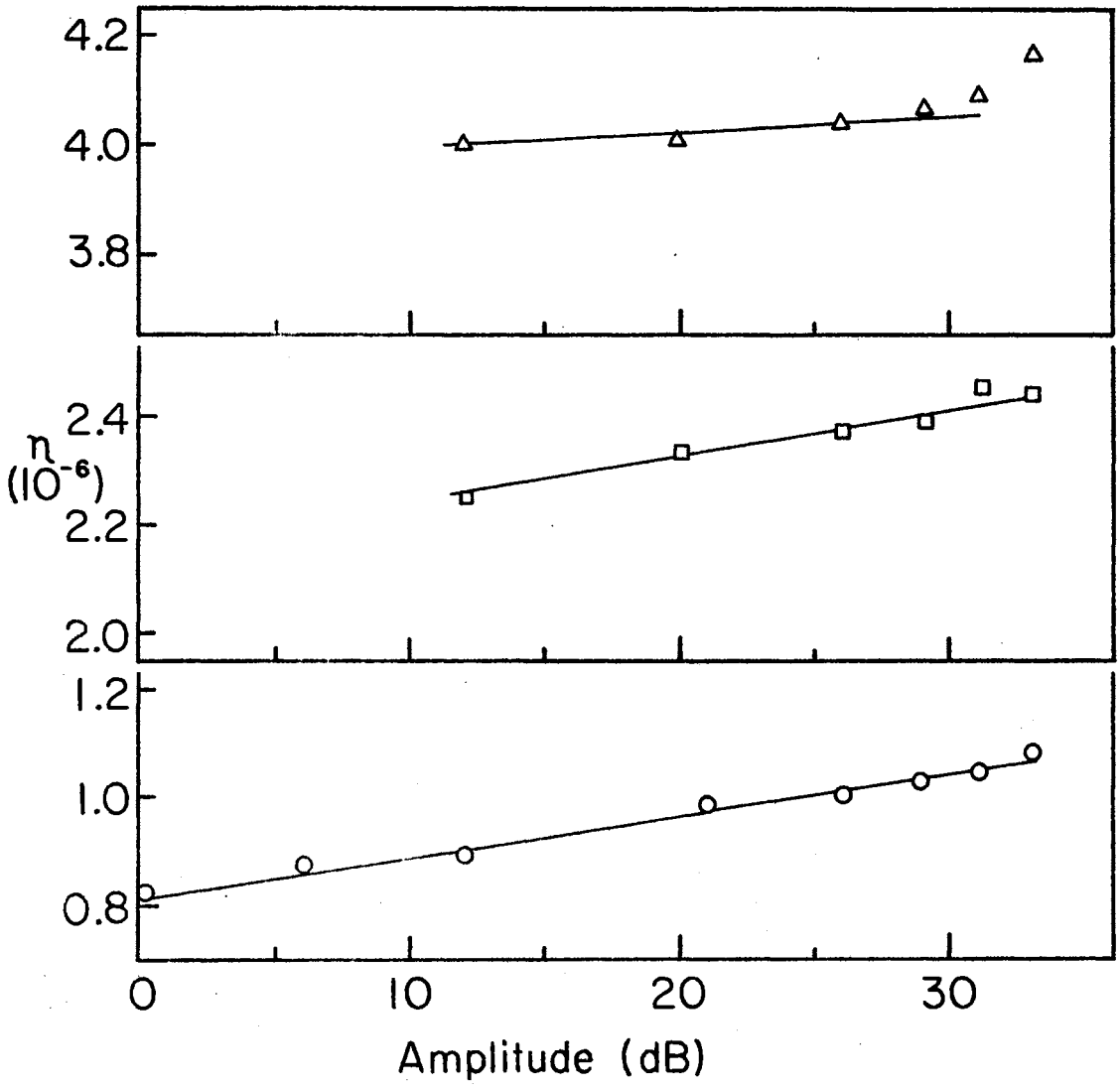

Figure 27. Amplitude Dependence of Loss Factor

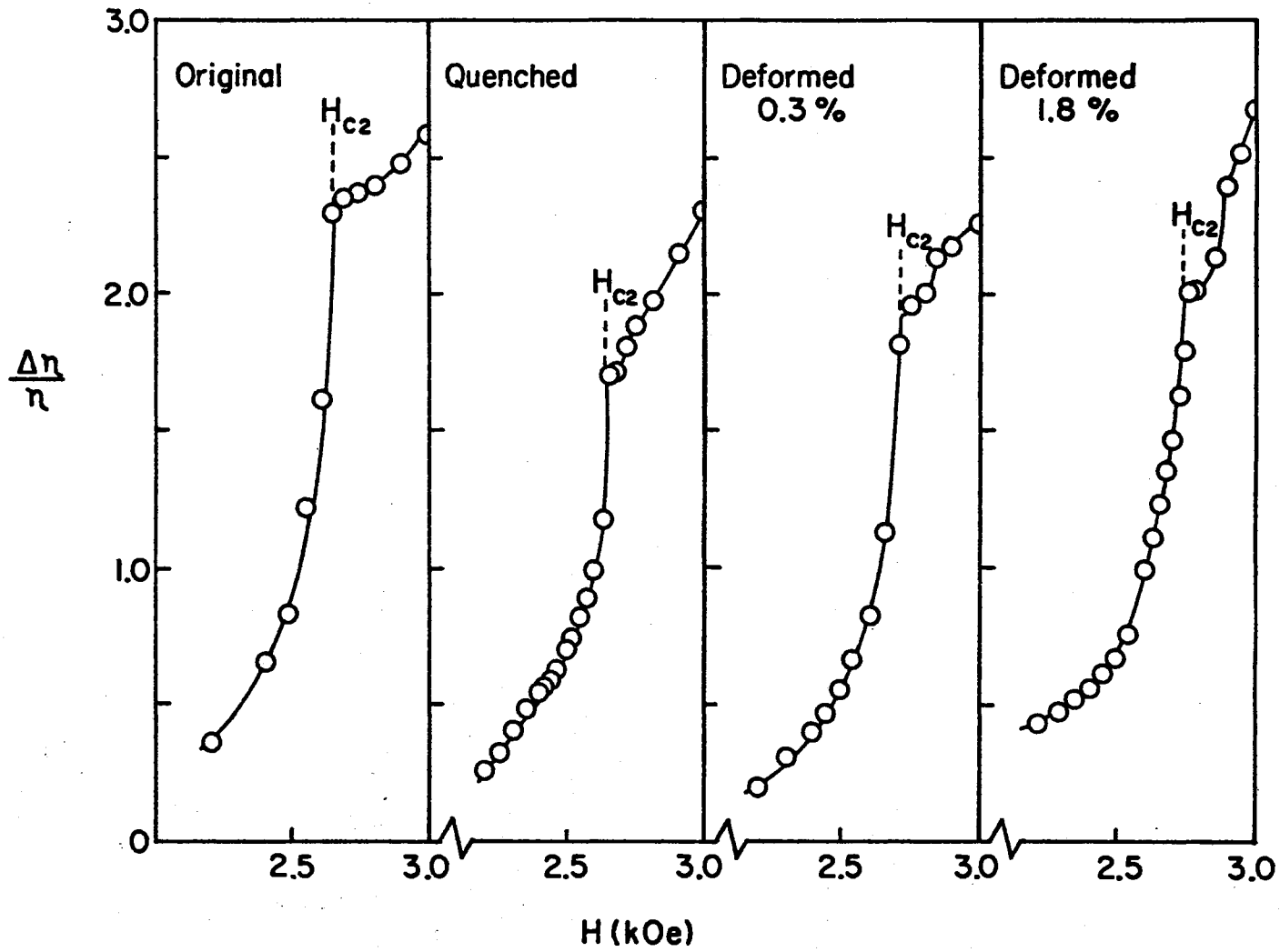

Figure 28. Fluctuation Effect as a Function of Deformation

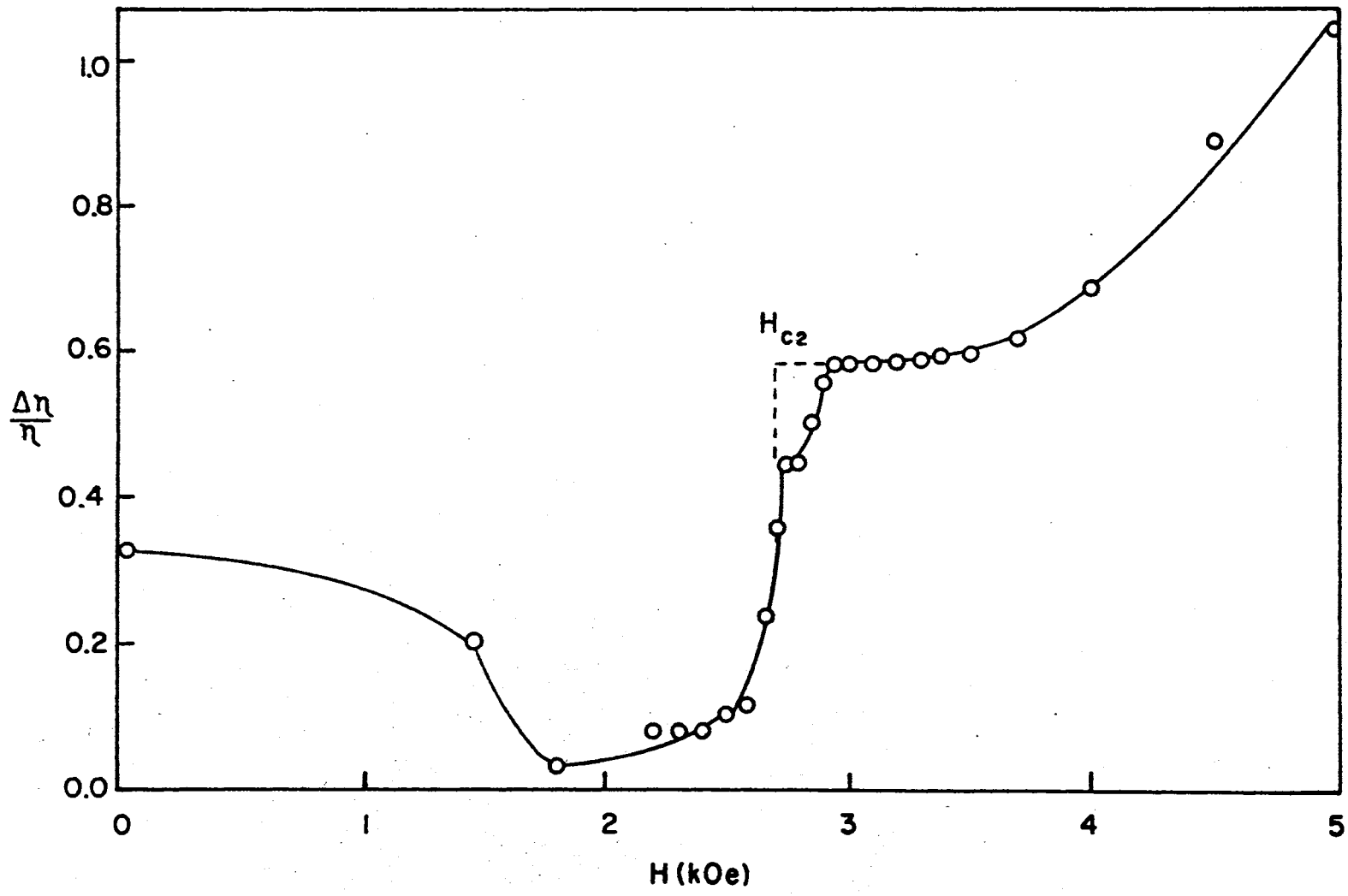

Figure 29. Longitudinal Dislocation Effect

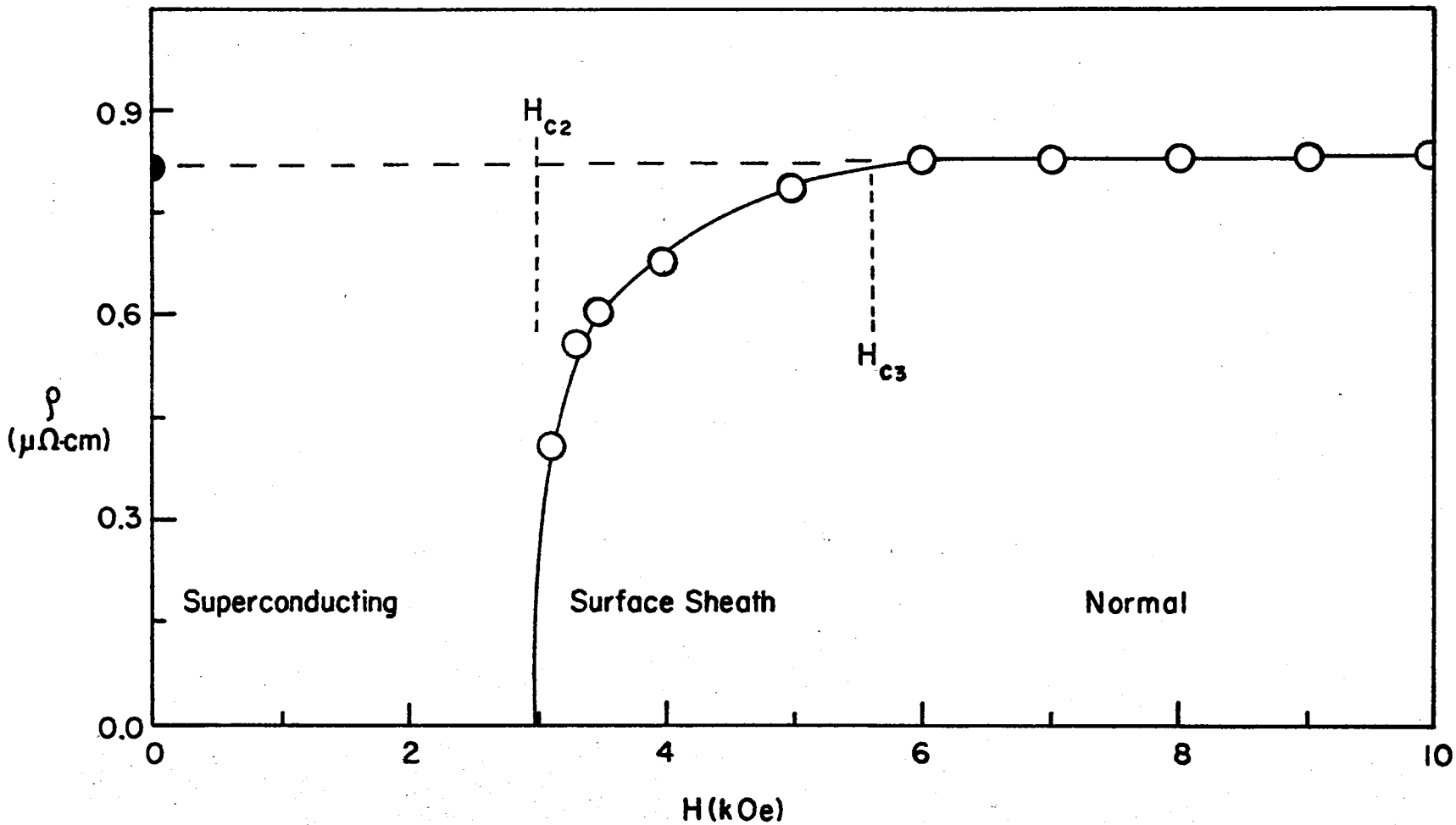

Figure 30. Resistivity at $4^{o}K$

resistivity is zero up to the upper critical field H_{C2}. The gradual return of the resistivity to the normal state is caused by surface superconductivity which is not entirely quenched until $H_{C3} = 1.7H_{C2}$. The high field data (H > 5 kOe) is then extrapolated back to zero field to obtain the residual resistivity that would be present, if the superconducting state did not interfer. The slope of the high field data gives the magnetoresistance of the material. The high purity samples have a very low impurity resistivity and exhibit the magnetoresistance more clearly (Figure 31). The temperature dependence of the resistivity of a high and a low purity specimen is compared to show the effect of dissolved gases, which are believed to be the major impurity (Figure 32).

Table IX gives the important parameters associated with the re-

TABLE IX

COMPARISON OF RESISTIVITY DATA

Sample	$\rho(300)$ ($\mu\Omega$cm)	$\rho(77)$ ($\mu\Omega$cm)	$\rho(4.2)$ ($\mu\Omega$ cm)	$\ell_e(4.2)$ (10^{-5} cm)	RRR	Magneto-Resistance (10^{-5} $\mu\Omega$cm/Oe)	$q_L\ell$ (10^{-5})
Nb (100) #1	19.4	3.59	0.640	1.58	30	----	1.15
Nb (110) #2	15.0	2.58	0.173	5.83	86	----	4.52
Nb (111) #4	18.8	1.93	0.341	2.98	55	----	2.00
Nb (100) #5	17.1	2.82	0.0068	163.	2500	7.2	119.
Nb (111) #6	18.5	3.00	0.0075	136.	2500	9.5	100.
Nb (poly) #1	15.7	2.78	0.335	3.05	47	----	2.37
V (poly) #1	22.5	3.76	1.33	.619	17	----	.384
Ta (poly) #1	14.7	3.24	0.751	1.41	20	----	1.09

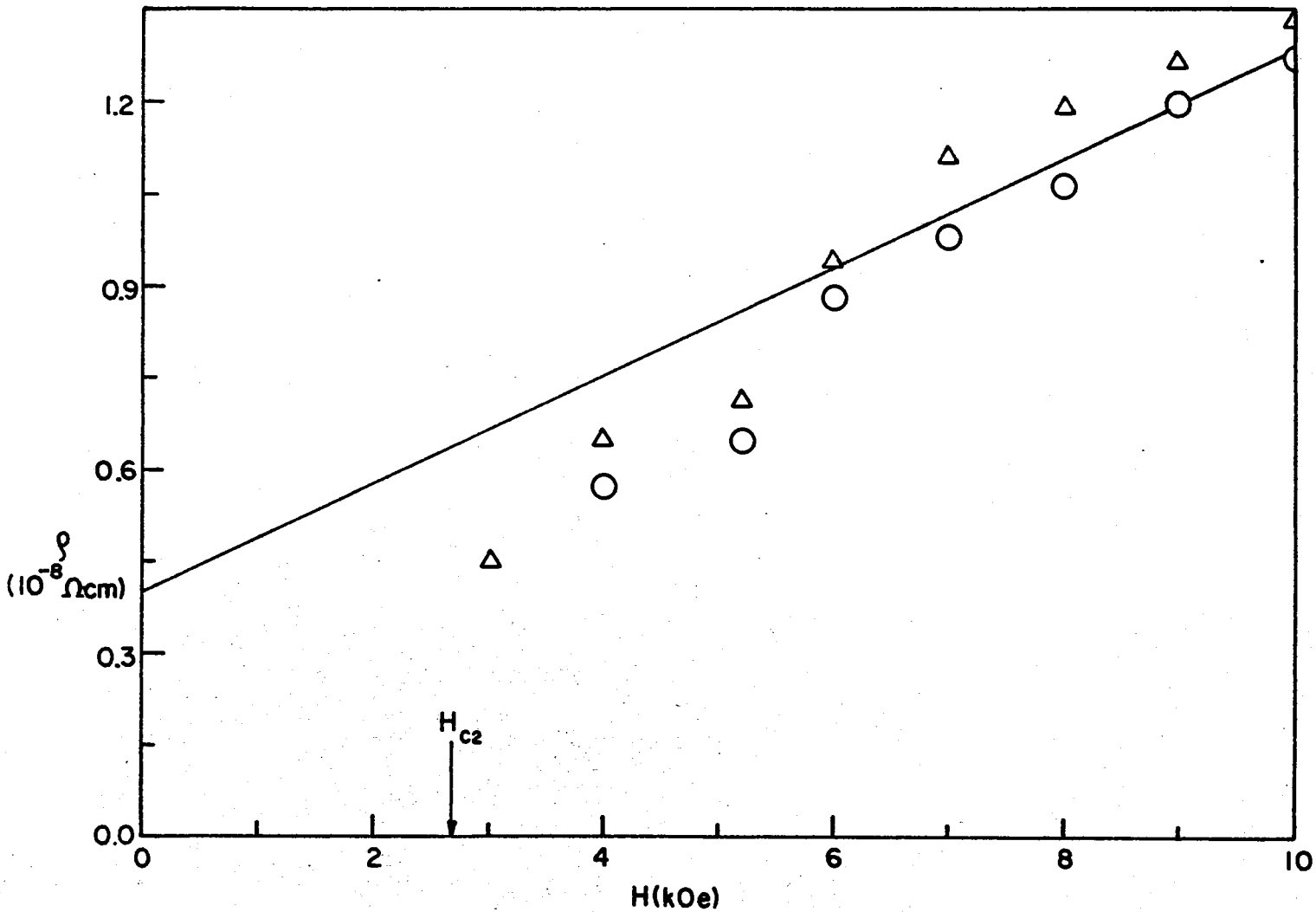

Figure 31. Magnetoresistance

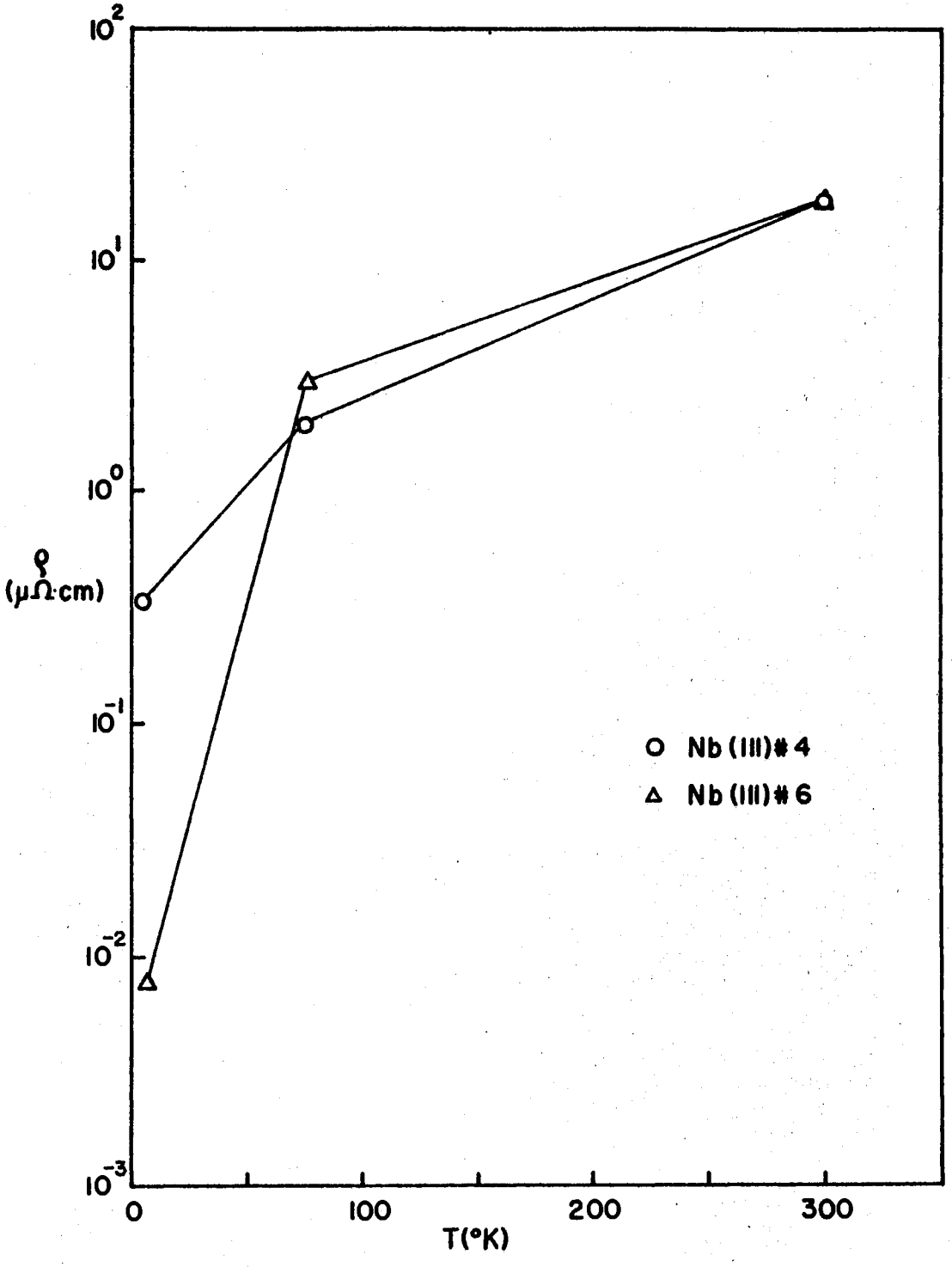

Figure 32. Resistivity Versus Temperature

sistivity data. The electronic mean free path calculation is performed to calculate q_ℓ, the product of the wave vector and the mean free path. For samples with $q_\ell < 1$ the electronic attenuation is proportional to the square of the frequency, while for $q_\ell > 1$ it is proportional to the frequency to the first power. It is a way of comparing data between two samples, just as the residual resistance ratio is directly proportional to the purity of the sample and allows comparison between samples. The high purity samples may be tested in the limit $q_\ell > 1$ by using high frequency acoustic excitation (~ 1 GHz).

Alloys

The alloy samples prepared in this laboratory proved to be insufficient for elastic measurements due to the increased attenuation as a function of impurity. This lowered the Q of the samples so that the accuracy of the measurement was reduced below an exceptable limit. It had been hoped that the alloys would provide a way to change the Landau-Ginzburg parameter, K, and allow a study of the mixed state in one basic metal as a function of K. The loss in Q could be attributed to the crude method of preparation allowing dissolved gases to cause problems similar to those found in Nb. The use of starting material (Pb) from two separate sources may have also caused some inconsistencies. The purity of the Pb-Sn alloys maybe inferred from the 4.2°K resistivity data (Figure 33). The change in sound velocity of different alloys follows a similar curve to the resistivity, or purity (Figure 34). Only the pure Pb sample yielded a sufficiently high Q to make an accurate elastic measurement in the superconducting state. The Pb followed the linear dependence predicted for the intermediate state[81] and agreed with

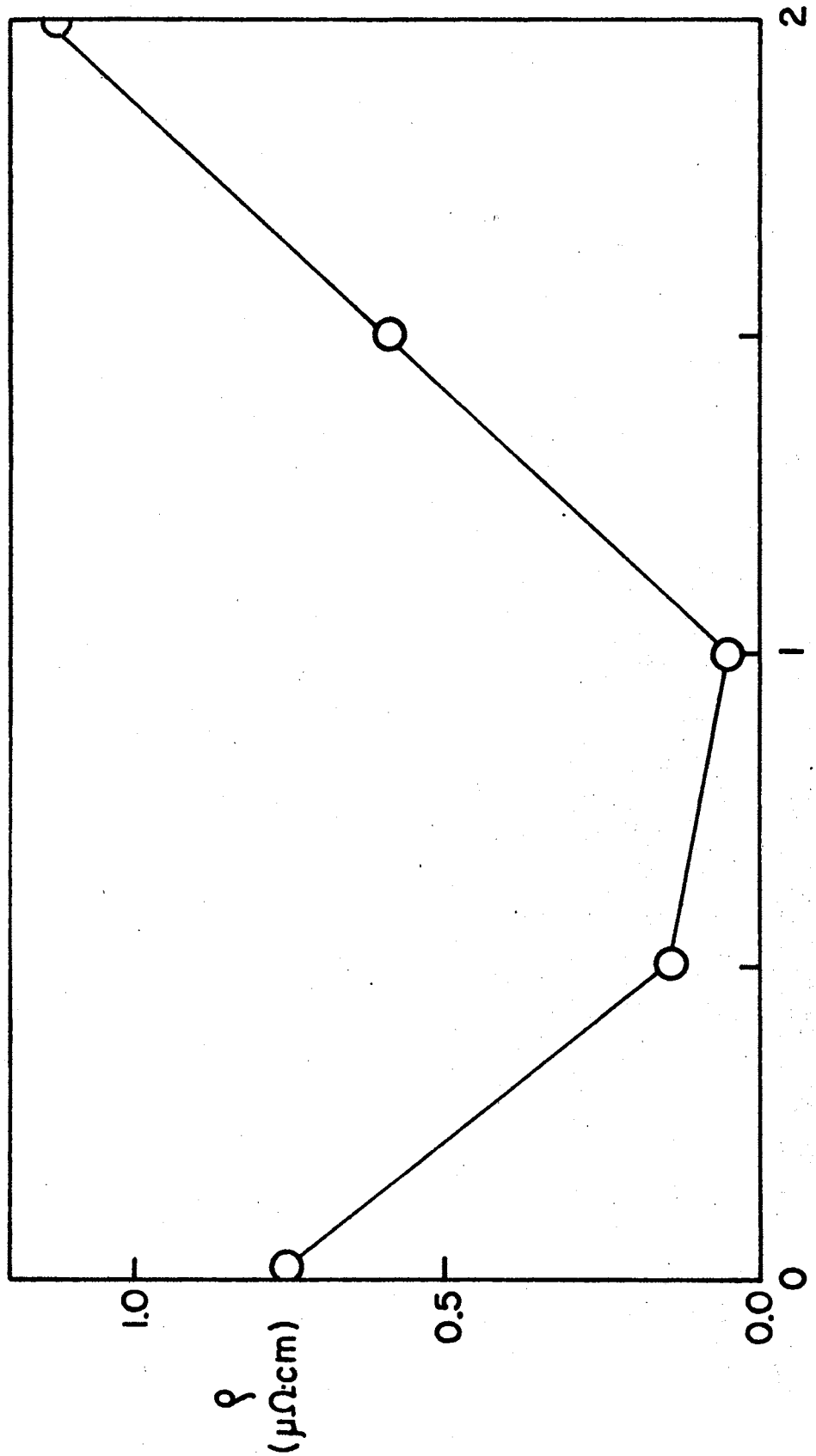

Figure 33. Resistivity of Alloys

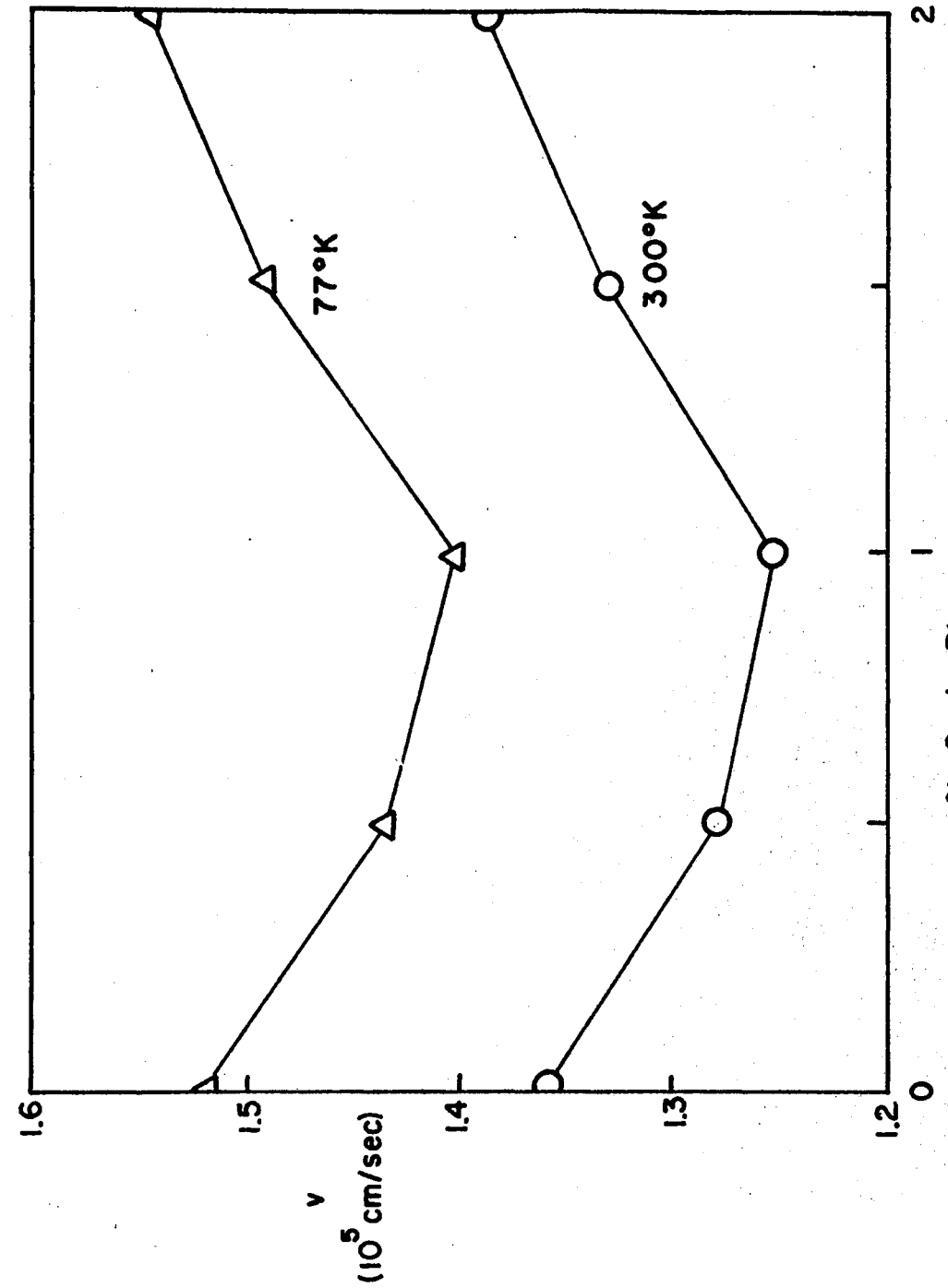

Figure 34. Alloy Sound Velocities

the previously published critical field[64] (Figure 35). The Q of the SnIn alloy system was too low to allow sufficient accuracy in all cases. However, it was found that the impurities did not seem to affect the normal state dependence on the square of the magnetic field for those percentages of alloy tested. Sn was used as an impurity in Pb at 0%, ½%, 1%, 1½%, and 2% levels, while In was used in Sn at 0%, 2%, 16%, and 50% levels. 2% was the limit of solubility of Sn in Pb, but In and Sn may be mixed at any percentage.

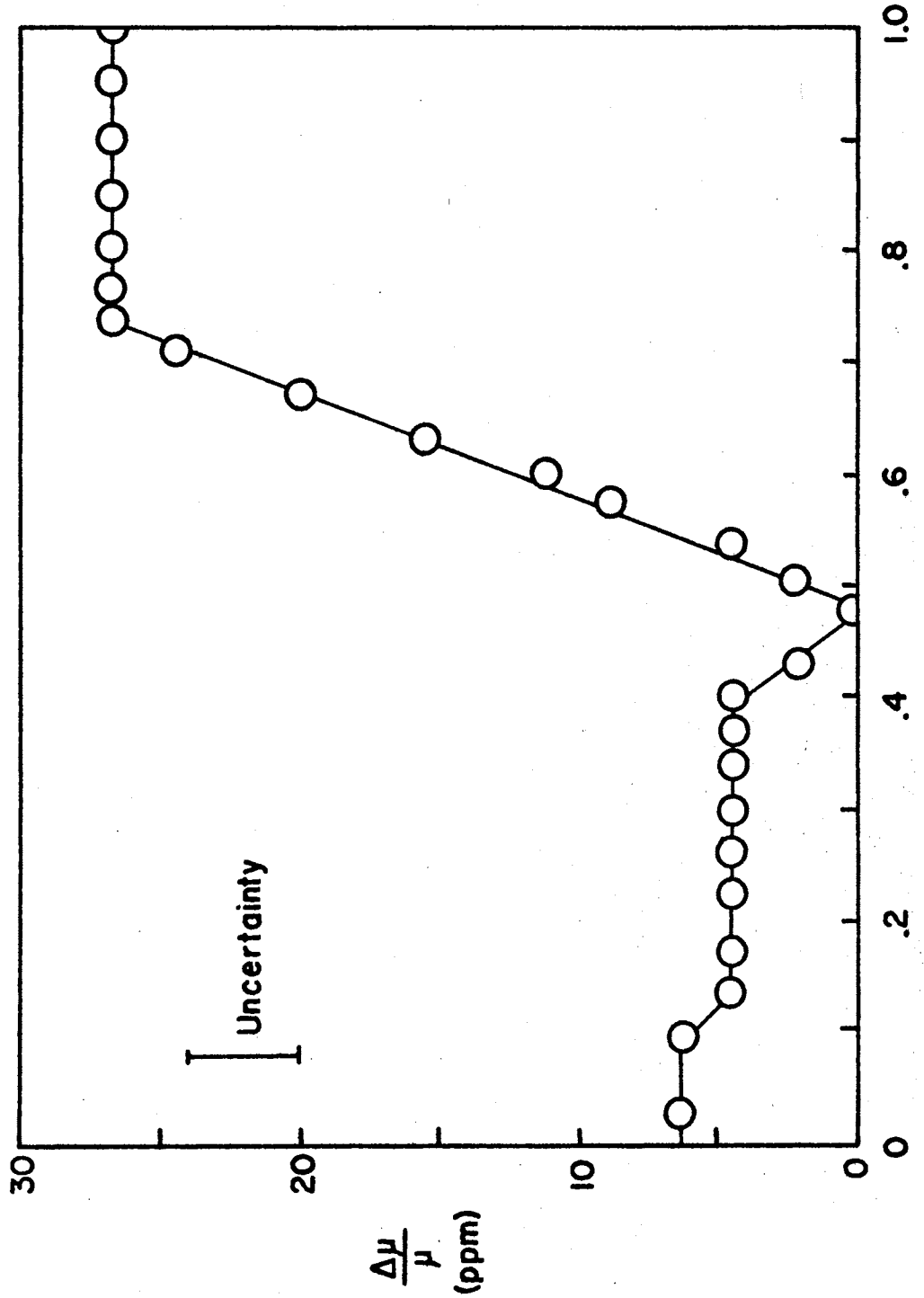

Figure 35. Pb Transition

CHAPTER V

CONCLUSIONS

Normal State Behavior

The low frequency acoustic interaction with a magnetic field in metals has been developed theoretically[60] and found to be in very good agreement with the experiment results for the longitudinal mode. The torsional mode lacks a theoretical explanation, since the proposed theories yield results two orders of magnitude too small compared to the experimental data for the modulus and one order of magnitude too small for the loss factor. The smabl differences between samples may or may not be introduced by a scaling factor.

An unusual effect was found in the normal state anisotropic elasticity of both the longitudinal and torsional modes. The effect of lobes along primary slip planes for the (111) oriented crystals seems to indicate that dislocations are the primary mechanism responsible for the anisotropy. Since only the crystals oriented with the major slip direction parallel to the propagation vector exhibited the effect and since the effect was removed from the torsional mode by severe deformation, dislocations are again a plausible cause. This data in conjunction with the superconducting state data further supports the hypothesis.

Superconducting State Behavior

The low frequency acoustic interaction in the superconducting state

was most interesting in the observed magnetic fluctuations[166] above H_{c2}. The normal state and superconducting state data compliments each other on the hypothesis that dislocations are responsible for the effect. The lower purity sample had less electronic transition observed in the loss factor and defined the fluctuation effect more clearly. A plot of the difference (δ) between the observed field dependence and the theoretical normal state dependence (for Figure 25) in the critical field region shows an initial exponential drop, characteristic of fluctuation phenomenon (Figure 36). If the data is fit to

$$\delta = Ae^{-\alpha h}$$

where $h = (H - H_{c2})/H_{c2}$, α is found to be approximately 10. The normal state is reached when δ returns to zero. The slight overshoot of δ being positive is interpreted as possible resonant absorption as the electronic viscosity increases and the lifetimes of transient Cooper pairs match the period of the oscillating dislocation line. The effect of dislocation density of the fluctuation phenomenon is a subtle hint that dislocations are responsible for the effect. Also, the evidence that only the dissipative part of the complex elasticity reflects the effect is consistent with the electronic viscosity being proposed as the coupling mechanism between the fluctuations and the moving dislocations.

The real part of the elasticity was used to show the dependence of the elasticity on the normal volume fraction of material in the mixed state. While the longitudinal mode data was in general more easily related to the normal volume fraction,[81] the torsional mode data was fit by the same calculation, since the fractional change in modulus was normalized by the total change in modulus. The increased elasticity in

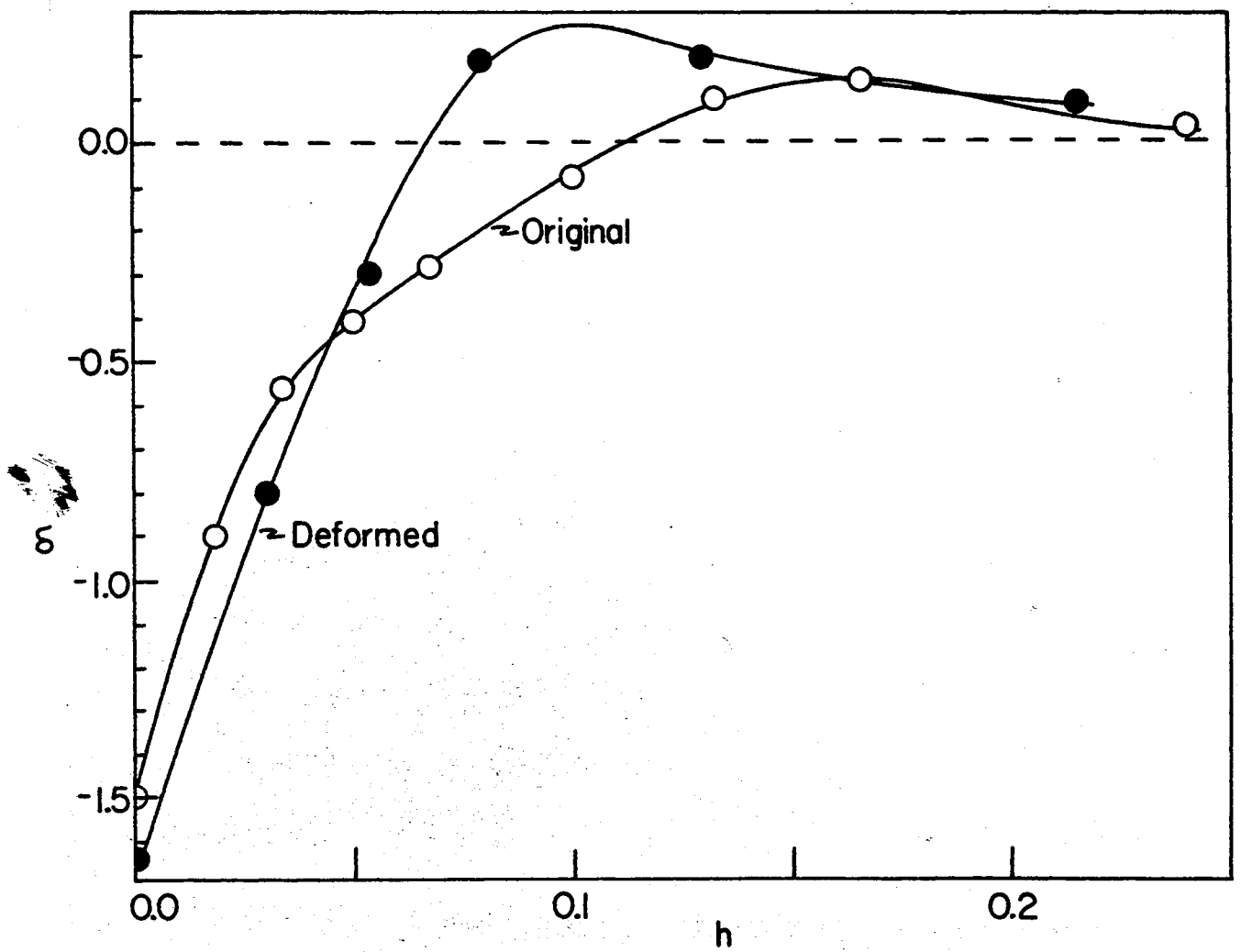

Figure 36. Magnetic Fluctuations

the mixed state due to the normal volume of material in the vortex was taken into account by this normalization. The dependence of the total change in Young's modulus across the superconducting state is speculatively related to the electronic mean free path limiting the vortex interaction in Nb when ℓ_e is greater than the spacing between vortices.

Suggestions for Further Work

There are many possible uses of this apparatus and the procedures for making elastic measurements described in this work. Several continuations of the work on superconductors could be performed, such as the study of a series of samples of vanadium or other Type II material to relate and compare with Nb. The effect of different values of K could be seen, as was attempted in the alloy work. If an alloy of sufficiently high Q could be found, it could yield a very interesting set of data as function of K. It should be pointed out that this bulk property, or lattice type measurement in conjunction with a high frequency (~1 GHz), or electronic type measurement gives much more information than either one could independently.

A study of controlled radiation damage, or deformation damage by other means, in various types of crystals oriented to exhibit the dislocation effect would be most challenging. These internal friction measurements could be studied in many different connections: critical points, phase changes, etc. The extent of this method of studying dislocation motion should be vast and add much knowledge to this field. In connection to this type of measurement, a flexual mode could be generated in cylindrical rods by cutting a small flat area on the side of the sample at its end and used with a capacitive drive as the excitation

coupler.

Another phase transition that may be of interest to study by this internal friction method would be the magnetic saturation of ferromagnetic materials. A trial run for a Ni rod of low purity was made for a longitudinal mode and is presented in Figure 37. The internal friction associated with domain motion in ferromagnetic materials would be a subject of investigation.

Perhaps the most striking possibility of this apparatus would be the investigation of the elastic properties of semiconductors. A full range of elastic data in various doped semiconductors could be easily attained. Since this system of measurement has been produced, it seems that a wide variety of uses for it have developed.

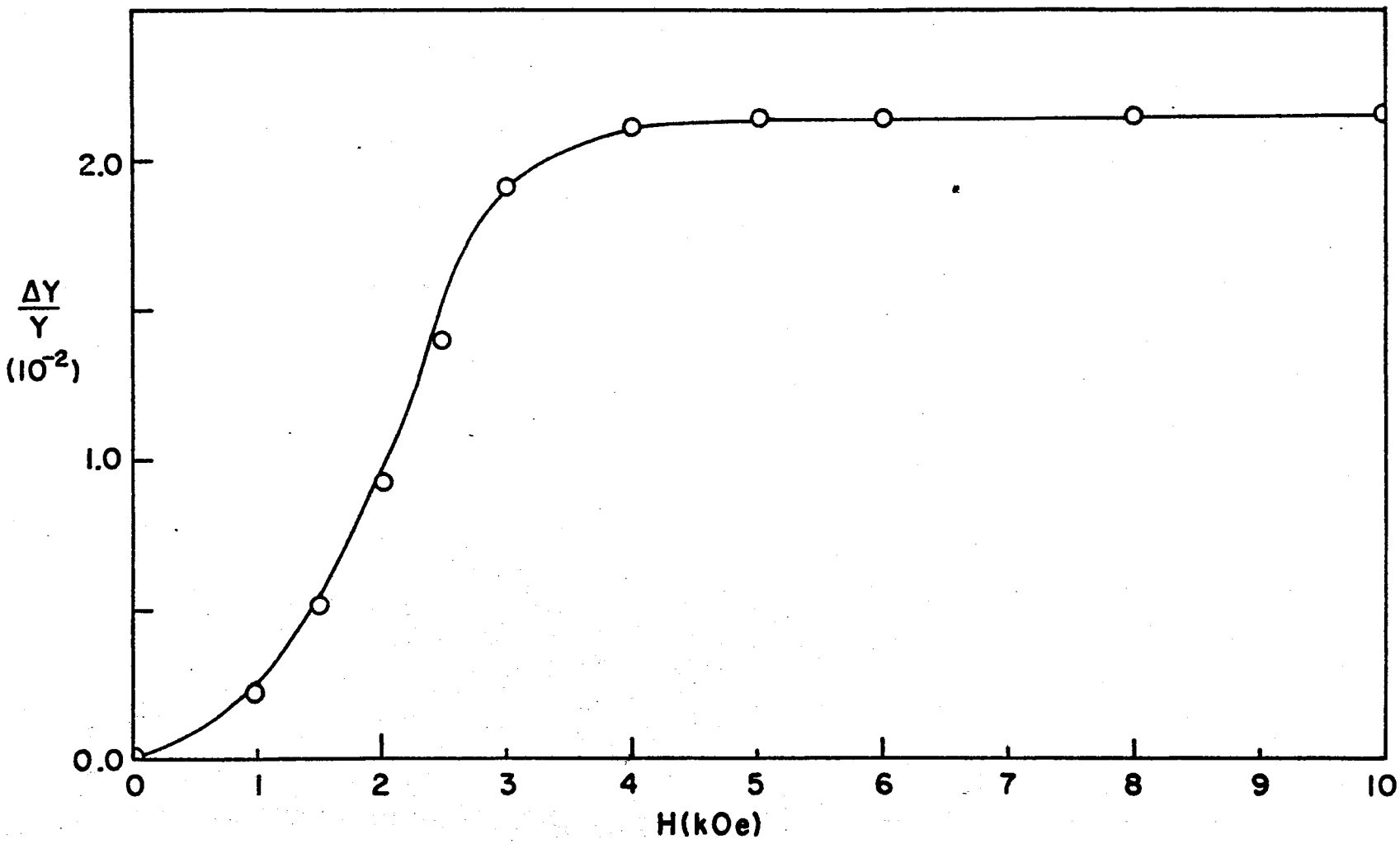

Figure 37. Ferromagnetic Saturation of Ni

BIBLIOGRAPHY

1. J. Bardeen, N. Cooper, and J. Schrieffer. Phys. Rev. 106, (1957), 108, 1175 (1957).

2. C. H. Hinrichs and C. A. Swenson. Phys. Rev. 123, 1106 (1961).

3. E. Hecht and R. W. Genberg. Phys. Rev. Letters 19, 2159 (1967).

4. H. G. Van Buren. Imperfections in Crystals, 2nd ed., Amsterdam: North-Holland (1961).

5. D. Shoenberg. Superconductivity, Cambridge Univ. Press (1952).

6. H. Rohrer. Physica 24, 5152: London (1958).

7. K. Anders, J. L. Olsen, and H. Rohrer. IBM J. Res. and Dev. 6, 84 (1962).

8. W. B. Sampson, P. P. Craig, and M. Strongin. Sci. Am. 216, 114 (1967).

9. H. Kamerlingh-Onnes. Commun. Phys. Lab. Univ. of Leiden 119, 120b, 122b, 124c (1911).

10. H. Kamerlingh-Onnes. Akad. van Wetenschappen (Amsterdam) 14, 113, 818 (1911).

11. W. H. Keesom and J. N. van den Ende. Commun. Phys. Lab. Univ. of Leiden 2196 (1932).

12. W. H. Keesom and J. A. Kok. Physica 1, 175 (1934).

13. W. Meissner and R. Ochsenfeld. Die Naturwissenschaften 21, 787 (1933).

14. W. H. Keesom. Rapp. et Disc. 4e Congr. Phys. Solvay 288, (1924).

15. A. J. Rutgers. Physica 1, 1055 (1934).

16. C. J. Gorter. Arch. Mus. Teyler 7, 378 (1933).

17. C. J. Gorter and H. B. Casmir. Physica 1, 306 (1934).

18. C. J. Gorter and H. B. Casmir. Phys. Z. 35, 963 (1934).

19. J. Gorter and H. B. Casmir. Z. Techn. Phys. 15, 539 (1934).

20. K. Mendelssohn. Proc. Roy. Soc. (London) A152 34 (1935).

21. H. London and F. London. Proc. Roy. Soc. (London) A149, 71 (1935).

22. H. London and F. London. Physica 2, 341 (1935).

23. F. London. Proc. Roy. Soc. (London) A152, 24 (1935).

24. R. B. Pontius. Phil. Mag. 24, 787 (1937).

25. D. Shoenberg. Proc. Roy. Soc. (London) A175, 49 (1940).

26. J. M. Lock. Proc. Roy. Soc. (London) A208, 391 (1951).

27. E. Laurmann and D. Shoenberg. Proc. Roy. Soc. (London) A198, 560 (1949).

28. L. D. Landau. Phys. A. Sowjetunion 11, 129 (1937).

29. F. London. Physica 3, 450 (1936).

30. A. G. Meshkovsky and A. I. Shalinikov. J. Phys. (USSR) 11, 1 (1947).

31. A. G. Meshkovsky and A. I. Shalinikov. J. Exp. Theor. Phys. (USSR) 17, 851 (1947).

32. A. L. Schawlow. Phys. Rev. 101, 573 (1956).

33. B. M. Balashova and Yu. V. Sharvin. Soviet Physics, JETP 4, 54 (1957).

34. H. London. Proc. Roy. Soc. (London) A176, 522 (1940).

35. A. B. Pippard. Proc. Roy. Soc. (London) A191, 370 (1947).

36. V. L. Ginzberg and L. D. Landau. Zh. Eksperim. Theor. Fiz. 20, 1064 (1950).

37. A. A. Abrikosov. Soviet Phys. - JETP 5, 1174 (1957).

38. B. B. Goodman. Phys. Rev. Letters 6, 597 (1961).

39. E. Maxwell. Phys. Rev. 78, 477 (1950).

40. B. T. Matthias, et. al. Science 156, 645 (1967).

41. H. Fröhlich. Phys. Rev. 79, 845 (1950).

42. J. Bardeen. Rev. Mod. Phys. 23, 261 (1951).

43. A. B. Pippard. Proc. Roy. Soc. (London) A203, 210 (1950).

44. A. B. Pippard. Proc. Roy. Soc. (London) A203, 98 (1950).

45. J. Bardeen. Rev. Mod. Phys. 97, 1724 (1955).

46. See for example: M. A. Bionid. A. T. Forrester, M. P. Garfunkel, and C. B. Satterthwaite. Rev. Mod. Phy. 30, 1109 (1958).

47. B. J. Matthias. Progress in Low Temperature Physics, Ed. C. J. Gorter; Amsterdam: North-Holland Pub (1957), Vol. II, p. 138.

48. L. N. Cooper. Phys. Rev. 104, 1189 (1956).

49. N. N. Bogoliubov, V. V. Tolmachev, and D. V. Shirkov. A New Method in the Theory of Superconductivity: New York: Consultants Bureau, Inc., (1959).

50. A. Bohr, B. R. Mottelson, and D. Pines. Phys. Rev. 110, 936 (1958).

51. Y. Nambu. Proc. Midwest Theoret. Phys. Conf., Purdue Univ., April (1960).

52. I. Giaever. Phys. Rev. Letters 5, 147 (1960).

53. R. Doll and M. Näbauer. Z. Phys. 169, 526 (1962).

54. B. S. Deaver and W. M. Fairbank. Phys. Rev. Letters 7, 43 (1961).

55. B. D. Josephson. Phys. Letters 1, 251 (1962).

56. P. W. Anderson. Phys. Today 23, 23 (1970).

57. H. Suhl, B. T. Matthias, and L. R. Walker. Phys, Rev. Letters 3, 552 (1959).

58. G. A. Alers and P. A. Fleury. Phys. Rev. 129, 2425 (1963).

59. S. Rodriguez. Phys. Rev. 130, 1778 (1963).

60. J. Lange. Phys. Rev. 179, 631 (1969).

61. D. P. Seraphim and P. M. Marcus. IBM J. Res. and Dev. 6, 94 (1962).

62. H. B. Hungtington. Solid State Physics, Ed. F. Seitz and D. Turnbull. New York: Academic Press, Inc. (1958), Vol. 7, p. 214.

63. R. Labusch. Phys. Rev. 170, 470 (1968).

64. C. Kittel. Introduction to Solid State Physics, 3rd ed. New York: John Wiley and Sons, Inc. (1966), p. 121.

65. H. Kolsky. Stress Waves in Solids, Dover Pub. Co.: New York (1963).

66. G. A. Alers and D. L. Waldorf. IBM J. Res. and Dev. 6, 89 (1962).

67. G. A. Alers. Physical Acoustics, Ed. W. P. Mason: New York, Aca-

demic Press, Inc.; (1966), Vol. IVA, Ch. 7.

68. H. Bömmel and J. L. Olsen. Phys. Rev. (Letter) 91, 1017 (1953).

69. J. L. Olsen. Nature (London) 175, 37 (1955).

70. J. L. Routbort and H. S. Sack. Phys. Stat. Sol. 22, 203 (1967).

71. A. S. Nowick. Phys. Rev. 80, 249 (1950).

72. J. K. Landauer. Phys. Rev. 96, 296 (1954).

73. B. Welber. J. Acoust. Soc. Am. 27, 1010 (1955).

74. B. Welber and S. L. Quimb. Acta. Met. 6, 351 (1958).

75. D. F. Gibbons and C. A. Renton. Phys. Rev. 114, 1257 (1959).

76. E. J. Kramer and C. L. Bauer. Phys. Rev. 163, 407 (1967).

77. E. J. Kramer and C. L. Bauer. Phys. Status Solidi 22, 199 (1967).

78. P. G. Bordoni. Nuovo Cimento 4, 177 (1947), J. Acoust. Soc. Am. 26, 495 (1954).

79. G. W. Goodrich. (Unpublished M.S. Thesis, O.S.U., 1968).

80. J. Lange and G. W. Goodrich. Bull. Am. Phys. Soc. 13, 1375 (1968).

81. G. Goodrich and J. Lange, Phys. Rev. 188, 728 (1969).

82. H. E. Bömmel. Phys. Rev. (Letter) 96, 220 (1954).

83. W. P. Mason. Phys. Rev. (Letter) 97, 557 (1955).

84. R. W. Morse. Phys. Rev. (Letter) 97, 1716 (1955).

85. W. P. Mason and H. E. Bömmel. J. Acoust. Soc. Am. 28, 930 (1956).

86. M. S. Steinberg. Phys. Rev. 111, 425 (1958).

87. E. Lax. Phys. Rev. 115, 1591 (1959).

88. T. Tsuneto. Phys. Rev. 121, 402 (1961).

89. L. Claiborne and N. Einspruch. Phys. Rev. 132, 621 (1963).

90. N. Tsuda and T. Suzuki. J. Phys. Chem. Solids 28, 2487 (1967).

91. F. B. McLean and A. Houghton. Phys. Rev. 157, 350 (1967).

92. M. Gottlieb, C. K. Jones, and M. Garbuny. Phys. Letters 25A, 107 (1967).

93. J. Lange. J. Phys. Chem. Solids 31, 1693 (1970).

94. M. S. Steinberg. Phys. Rev. 109, 1486 (1958).

95. K. Maki. Phys. Rev. 156, 437 (1967).

96. H. B. Callen. Thermodynamics: New York, John Wiley and Sons, Inc., (1963).

97. R. M. Bozorth and D. M. Chapin. J. Appl. Phys. 13, 320 (1942).

98. R. P. Feynman. Progress in Low Temperature Physics: Amsterdam, North-Holland Pub. (1955), Vol. I.

99. L. Onsager. Nuovo Cimento 6, Supp. 2, 249 (1949).

100. A. L. Fetter, P. C. Hohenberg, and P. Pincus. Phys. Rev. 147, 140 (1966).

101. B. Rosenblum and M. Cardona. Phys. Rev. Letters 12, 657 (1964).

102. C. Caroli and J. Matricon. Phys. Kondes. Materie 3, 380 (1965).

103. D. G. Schweitzer and M. Garber. Phys. Rev. 160, 348 (1967).

104. W. H. Kleiner, L. M. Roth, and S. H. Autler. Phys. Rev. 133, A1226 (1964).

105. U. Essman and H. Träuble. Phys. Letters 24A, 526 (1967).

106. B. Obst. Phys. Letters 28A, 662 (1969).

107. P. G. DeGennes. Superconductivity of Metals and Alloys: New York, W. A. Benjamin, Inc. (1966).

108. E. Maxwell and M. Strongin. Phys. Rev. Letters 10, 212 (1963).

109. M. D. Sherrill. Phys. Letters 24A, 312 (1967).

110. Y. A. Rocher and J. C. Renard. Phys. Letters 25A, 119 (1967).

111. V. P. Galaiko. Soviet Physics - JETP 23, 878 (1966).

112. T. E. Faber. Nature (London) 164, 277 (1949).

113. W. F. Vinen and A. C. Warren. Proc. Phys. Soc. 91, 399 (1967).

114. J. Friedel, P. G. de Gennes, and J. Matricon. Appl. Phys. Letters 2, 119 (1963).

115. J. Bardeen Phys. Rev. Letters 13, 747 (1964).

116. H. O. Lorch. Phys. Letters 17, 196 (1965).

117. G. B. Yntema. J. Appl. Phys. 39, 2514 (1968).

118. M. D. Sherill. IEEE Trans. Mag. MAG-4 324 (1968).

119. R. Leadon. J. Phys. Chem. Solids 28, 1093 (1967).

120. C. P. Bean and J. D. Livingston. Phys. Rev. Letters 12, 14 (1964).

121. R. W. De Blois and W. De Sorbo. Phys. Rev. Letters 18, 499 (1964).

122. B. P. Letellier and Y. A. Rocher. Solid State Commune. 5, 879 (1967).

123. H. Kojima and T. Suzuki. Phys. Rev. Letters 21, 896 (1968).

124. F. A. Otter and P. R. Solomon. Phys. Rev. Letters 16, 681 (1966).

125. A. K. Niessen, J. van Suchtelen, F. A. Staas, and W. F. Druyvesteyn. Phys. Letters 13, 293 (1964).

126. J. Pearl. Phys. Rev. Letters 16, 99 (1966).

127. A. T. Fiory and B. Serin. Phys. Rev. Letters 16, 308 (1966).

128. D. J. Van Ooijen and G. T. Van Gurp. Phys. Letters 17, 230 (1965).

129. L. T. Claiborne and N. G. Einspruch. J. Appl. Phys. 37, 925 (1966).

130. M. R. Wertheimer and J. G. Gilchrist. J. Phys. Chem. Solids 28, 2509 (1967).

131. A. R. Strand, C. F. Hemstead, and Y. B. Kim. Phys. Rev. Letters 13, 794 (1964).

132. H. Suhl. Phys. Rev. Letters 14, 226 (1965).

133. M. Tinkham. Phys. Rev. Letters 13, 804 (1964).

134. M. J. Stephen and J. Bardeen. Phys. Rev. Letters 14, 112 (1965).

135. P. P. M. Meincke. Phys. Letters 29A, 208 (1969).

136. W. W. Webb. Phys. Rev. Letters 11, 191 (1963).

137. E. J. Kramer and C. L. Bauer. Phil. Mag. 15, 1189 (1967).

138. J. Jurisson and R. J. Oakes. Phys. Letters 2, 187 (1962).

139. R. B. Flippen. Phys. Letters 24A, 588 (1967).

140. J. E. Zimmermann and J. E. Mercereau. Phys. Rev. Letters 13, 125 (1964).

141. Y. T. Chou. Acta. Met. 13, 251 (1965).

142. R. Labusch. Phys. Letters 22, 9 (1966).

143. J. Matricon. Phys. Letters 9, 289 (1964).

144. R. Labusch. Phys. Stat. Sol. 19, 715 (1967).

145. P. De Gennes and J. Matricon. Rev. Mod. Phys. 36, 45 (1965).

146. D. Stauffer. Phys. Letters 25A, 540 (1967).

147. P. P. M. Meincke and W. A. Reed. Phys. Rev. 179, 463 (1969).

148. J. Weertman. Elementary Dislocation Theory: New York, Macmillan (1964).

149. J. S. Koehler, Imperfections in Nearly Perfect Crystals : New York, John Wiley and Sons, Inc., (1952), p. 197.

150. A. Granato and K. Lucke, J. Appl. Phys. 27, 583 (1956).

151. R. E. Love, R. W. Shaw, and W. A. Fate, Phys. Rev. 138, A1453 (1965).

152. W. P. Mason, Phys. Rev. 143, 229 (1966).

153. B. R. Tittmann and H. E. Bömmel, Phys. Rev. 151, 178 (1966).

154. A. Hikata and C. Elbaum, Phys. Rev. Letters 18, 750 (1967).

155. H. Kojima and T. Suzuki, Phys. Rev. Letters 21, 896 (1968).

156. G. A. Alers, O. Buck, and B. R. Tittmann, Phys. Rev. Letters 23, 290 (1969).

157. T. S. Hutchinson and A. T. Pawlovicz, Phys. Rev. Letters 25, 1275 (1970).

158. R. E. Glover, Phys. Letters 25A, 542 (1967).

159. M. Strongin, O. F. Kammerer, J. Crow, R. S. Thompson, and H. L. Fine. Phys. Rev. Letters 20, 922 (1968).

160. W. E. Masker and R. D. Parks. Phys. Rev. B1, 2164 (1970).

161. R. V. D'Aierllo and S. J. Freedman. Phys. Rev. Letters 22, 515 (1969).

162. J. P. Gollub, M. R. Beasley, R. S. Newbower, and M. Tinkham. Phys. Rev. Letters 22, 1288 (1969).

163. R. E. Fassnacht and J. R. Dillinger. Phys. Rev. Letters 24, 1059 (1970).

164. L. G. Aslamazov and A. I. Larkin. Phys. Letters 26A, 238 (1968).

165. R. R. Hake, Phys. Rev. Letters 23, 1105 (1969).

166. J. Lange and G. Goodrich (to be pub.).

167. J. F. Guess and G. B. Thurston, "Measurement of the Flexual Response of Beams and Plates." (unpub. Research Contract Report, Oklahoma State University, 1963).

168. R. L. Wegel and H. Walther. Physics 6, 141 (1935).

169. G. Nelson (unpub. M.S. Thesis, Oklahoma State University, 1969).

170. W. Rhodes (unpub. M.S. Thesis, Oklahoma State University, 1968).

171. Kindly supplied by R. Reed, Solid State Division, Oak Ridge National Laboratory.

172. The Spark-Erosion machine was used through the cooperation of R. G. Goodrich at Louisiana State University.

173. The cooperation of Miss Patricia Reiff in preparing the alloy samples is appreciated.

174. J. D. Livingston. Phys. Rev. 129, 1943 (1963).

175. T. Aomine and Y. Shibuya. J. Phys. Soc. of Japan 25, 1289 (1968).

176. B. B. Goodman. Rev. Mod. Phys. 36, 13 (1965).

177. D. K. Finnemore, T. F. Stromberg, and C. A. Swenson. Phys. Rev. 149, 231 (1966).

APPENDIX A

COMPUTER PROGRAMS

Several computer programs were used during the course of this work that need explanation, if further use of them is desired. A program developed for calibration of a thermocouple using three fixed points as calibration points and accurate to $0.5^{o}K$ is explained elsewhere.[79] A program for a least-squares-fit to a quadratic function, one for giving a first order calculation of the interaction between vortices in a superconductor, and another for reducing the actual data to a form compatible with the above calculations were written, also.

The least-squares-fit program (Table X) gives the best fit to a curve of the form,

$$y = AH^2 + b ,$$

where A and b are the constants to be determined along with the mean square deviation. The input data must be of the following form: (1) the first card supplies the date in three columns of three (month, day, year) and (2) the next six cards supply the data in two columns of ten (variable, magnetic field). As many data sets of seven cards may be read as desired at once. A brief review of the least squares fit approach is given below. If the data is assumed to fit a curve of the above form, y is the theoretically predicted value as a function of H, and the actual data value is Y. The mean square deviation σ^2 is defined

TABLE X

LEAST-SQUARES-FIT PROGRAM

```
$JOB   10220,439-62-0806,TIME=10              G W GOODRICH
C      G. W. GOODRICH          LEAST-SQUARES-FIT              2-26-70
       WRITE(6,10)
    10 FORMAT(1H1,60H                A               B            MSQD
      1  SAMPLE,///)
       DIMENSION DN(6), FH(6),  DEL(6)
    11 READ(5,12,END = 90) LX,LY,LZ
    12 FORMAT(3I3)
    20 DO 40 I=1,6
       READ(5,30) DN(I), FH(I)
    30 FORMAT(2F10.0)
    40 CONTINUE
       SN=0.000
       SHSQ=0.000
       SHFO=0.000
       SNHS=0.000
       DO 50 I=1,6
       SN=DN(I) + SN
       SHSQ= (FH(I))**2 + SHSQ
       SHFO=(FH(I))**4 + SHFO
    50 SNHS=(DN(I))*((FH(I))**2) + SNHS
       A=((6.00)*(SNHS) - (SN)*(SHSQ))/((6.00)*(SHFO) - (SHSQ)**2)
       B=((SHFO)*(SN) - (SHSQ)*(SNHS))/((6.00)*(SHFO) - (SHSQ)**2)
       DO 60 I=1,6
    60 DEL(I)=A*(FH(I)**2) + B
       RMSQD=0.000
       DO 70 I=1,6
    70 RMSQD=((DEL(I) - DN(I))**2)/(6.00) + RMSQD
       WRITE(6,80) A, B, RMSQD, LX, LY, LZ
    80 FORMAT(1X,1P3E15.3,'       ',I2,'-',I2,'-',I2,//)
       GO TO 11
    90 STOP
       END
$ENTRY
  9  6 70
 28.0       5.00
 28.8       6.00
 29.5       7.00
 30.3       8.00
 31.5       9.00
 32.7       10.00
$IBSYS
```

a $\sigma^2 = \sum_{i=1}^{n} (y_i - Y_i)^2/n$, where n is the number of data points under consideration. Thus, minimization of σ^2 with respect to A and b yields

$$\sigma^2 = \Sigma(AH_i^2 + b - Y_i)^2/n ,$$

and

$$\frac{\partial\sigma^2}{\partial A} = 0 = (2/n)(A\Sigma H_i^4 + b\Sigma H_i^2 - \Sigma Y_i H_i^2,$$

and

$$\frac{\partial\sigma^2}{\partial b} = 0 = (2/n)(A\Sigma H_i^2 + nb - \Sigma Y_i) .$$

Solving for A and b yields the least-square-fit parameters,

$$A = (n\Sigma Y_i H_i^2 - \Sigma Y_i \Sigma H_i^2)/[n\Sigma H_i^4 - (\Sigma H_i^2)^2]$$

and

$$b = (\Sigma H_i^4 \Sigma Y_i - \Sigma H_i^2 \Sigma Y_i H_i^2)/[n\Sigma H_i^4 - (\Sigma H_i^2)^2]$$

The vortex interactions program (Table XI) was used to calculate some involved interactions as predicted by Goodrich and Lange.[81] Type I superconductors exhibit a linear dependence in the elasticity on the normal volume fraction through out the intermediate state. The calculations below showed that Type II materials depend on the normal volume fraction also, but do not exhibit a linear dependence in the elasticity. The fractional change in elastic modulus can be expressed in terms of the density of vortices (N) and total area of the vortex core (a_c) as

$$\frac{\Delta Y}{Y} = \left[\frac{\Delta Y}{Y}\right]_{TOT} Na_c$$

TABLE XI

VORTEX INTERACTIONS PROGRAM

```
$JOB    10220,439-62-0806,TIME=10              G W GOODRICH
C       G W GOODRICH       VORTEX INTERACTIONS          06-06-69
   50 READ(5,68)X,D,DELTA
   68 FORMAT(3F10.0)
      WRITE(6,63)
   63 FORMAT(1H1,75H       INCREMENT      SEPARATION          RADIUS
     1 Y RATIO          N/AREA,/)
      N=1
      L=1
   69 S= EXP(2.00/X)
      T= EXP(-2.00*D/X)
      Y= ALOG(2.00*X/((1.00+D-1.00/(1.00+D))*(S/(S-T))))
      R= 2.000+2.00*D+Y
      Z= ((2.000+2.00*D)**2)/(R**2)
      AN= 1.00/(R**2)
   74 IF(N-50)77,77,66
   77 IF(L-10)71,71,72
   71 WRITE(6,70)D,Y,R,Z,AN
   70 FORMAT(1X,4F15.3,F15.4)
      L= L+1
      N= N+1
      D= D+DELTA
      GO TO 75
   72 WRITE(6,73)D,Y,R,Z,AN
   73 FORMAT(1X,/,1X,4F15.3,F15.4)
      N= N+1
      L= 2
      D= D+DELTA
   75 IF(Y)76,76,69
   66 N= 0
      WRITE(6,67)
   67 FORMAT(1H1,75H       INCREMENT      SEPARATION          RADIUS
     1 Y RATIO          N/AREA,/)
      GO TO 72
   76 STOP
      END
$ENTRY
  0.72      0.01       0.01
  0.88      0.01      0.01
  1.00      0.01      0.01
  5.000     0.1       0.1
  10.00     0.1       0.1
$IBSYS
```

A model[81] of the vortex incorporates a normal core of diameter twice the coherence length ($2\xi_o$) and a magnetic field $H_{c2} = \phi/4\xi_o$, where ϕ is the quantum of flux. The magnetic field decreases exponentially into the superconducting region over a penetration depth (λ) according to London to a value H, determined by the external field, $H(r) = H_{c2}e^{-4/\lambda}$. At H_{c1} the vortices are isolated and non-interacting, but as H is increased greater H_{c1} the cores approach each other and the magnetic field overlap of nearest neighbors increases, resulting in an expanded vortex to maintain an energy density of $H_c^2/8\pi$. The field in the core must remain at H_{c2} to remain normal and the flux in the core becomes

$$H_{c2}\,\xi^2 = H_{c2}\,\xi_o^2 + \int H(r)da_c ,$$

where ξ is the expanded radius of the core.

To simplify the calculation and retain the essential features of the interaction, a model of the vortex is assumed with a square cross-section of side 2ξ. Evaluating the integral and solving the resulting transcendental equation leads to

$$(1 + \Delta\xi' - \frac{1}{1 + \Delta\xi'})(\frac{e^{-z/K}}{e^{-zK} - e^{-z\Delta\xi_o/K}}) = 2e^{-d/\xi_o K} ,$$

where K is the Landau-Ginsburg parameter, $\Delta\xi'$ is the fractional change in size of the vortex, and d is the separation between neighboring vortex boundaries.

The program solves this transcendental equation for various K as a function of d. It also computes the change in normalized size of the vortex as a function of a reduced magnetic field between $H_{c1}/2$ and H_{c2}.

The density of vortices (number per unit area) is given by

$$N = 1/[(2\xi_o)(H\Delta\xi') + d]^2 ,$$

while the area of the core is given by

$$a_c = 4\xi_o^2 (1 + \Delta\xi')^2 ,$$

thus, giving the fractional change in modulus as

$$\frac{\Delta Y}{Y} = [\frac{\Delta Y}{Y}]_{TOT} \; 4\xi_o^2 (1 + \Delta\xi')^2/[(2\xi_o)(1 + \Delta\xi') + d]^2 .$$

This result is then applied to the observed field dependence of the elasticity to obtain the size (ξ) and the density (N) of the vortices as a function of magnetic field. Within the limit of the accuracy of the vortex model, the elasticity can be used to determine the size, separation, and density of vortices throughout the mixed state.

The program requires an input of K, d, and an increment of d in three columns of ten to do these calculations. It prints increment, d, ξ, $[\Delta Y/Y]/[\Delta Y/Y]_{TOT}$, and density.

The data reduction program (Table XII) is used to reduce the experimental data to a form compatible with the theoretical calculations above. Given the total change in stiffness, H_{c1}, and H_{c2}, the program calculates for each stiffness and magnetic field point,

$$[\Delta Y/Y]/[\Delta Y/Y]_{TOT}$$

and

$$(H - H_{c1}/2)/(H_{c2} - H_{c1}/2) .$$

The input must be in the form of two card sets, the first set being one

TABLE XII

DATA REDUCTION PROGRAM

```
$JOB   10220,439-62-0806,TIME=10              G W GOODRICH
C      G W GOODRICH DATA REDUCTION   07-08-69
       J = 1
   50  READ(5,68)YTOT,XHC1,XHC2
   68  FORMAT(3F10.0)
   62  N=1
       L=1
       WRITE(6,65)
   65  FORMAT(1H1,20H      Y RED      H RED,/)
       GO TO 61
   60  IF(N-50.0)63,63,62
   63  IF(L-10.0)61,61,64
   64  L=1
       WRITE(6,66)
   66  FORMAT(1X,/)
   61  READ(5,67)Y,XH
   67  FORMAT(2F10.0)
       XHRED = (XH - XHC1)/(XHC2 - XHC1)
       YRED = Y/YTOT
       WRITE(6,69)YRED,XHRED
   69  FORMAT(1X,2F10.3)
       N = N + 1
       L = L + 1
       IF(YRED-1.00)60,70,70
   70  IF(J-8)80,90,90
   80  J = J + 1
       GO TO 50
   90  STOP
       END
$ENTRY
  190.00    630.       3150.
  0.00      630.
  1.50      680.
  2.50      700.
  6.50      750.
  12.50     800.
  26.50     900.
  39.50     1000.
  61.00     1200.
  79.50     1400.
  97.00     1600.
  106.00    1720.
  119.50    1910.
  135.50    2100.
  148.00    2300.
  162.00    2510.
  176.00    2700.
  181.50    2800.
  186.00    2900.
  188.00    3000.
  189.00    3100.
  190.00    3150.
$IBSYS
```

card giving in three columns of ten, $[\Delta Y/Y]_{TOT}$, $H_{c1}/2$, and H_{c2}, and the second set giving the experimental points in two columns of ten, $\Delta Y/Y$ and H. The program on vortex interactions coupled with this one were used to generate the curves[81] in Figures 38-40.

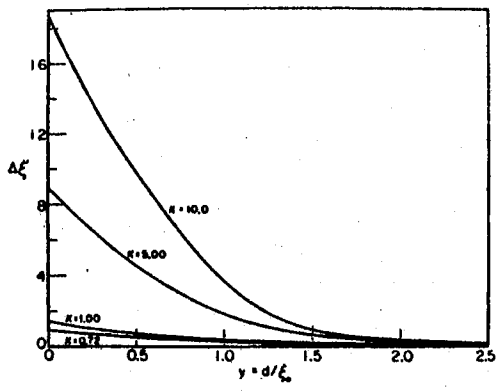

Figure 38. Fractional Change in Size of Vortex Versus Separation

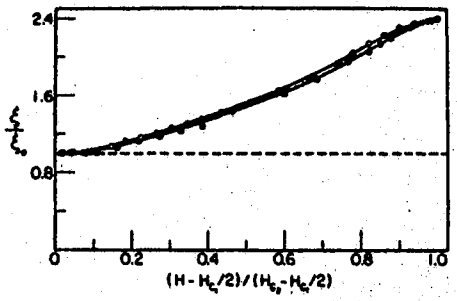

Figure 39. Expansion of Vortices in Mixed State

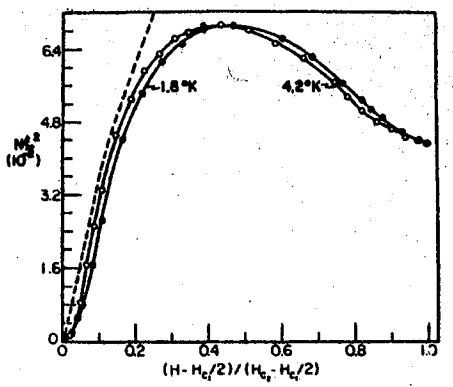

Figure 40. Number of Vortices in Mixed State

APPENDIX B

TABLE XIII

Symbols

a_c = vortex core area

A = least-squares-fit parameter

b = least-squares-fit parameter

B = magnetic field

c = speed of light in a vacuum

C = elastic constant

d = separation between vortices

D = curve fit parameter

e = electronic charge

E = curve fit parameter

f = frequency

F = force

$\bar{g}$ = dislocation line vector

H = magnetic field intensity

i = $\sqrt{-1}$

I = mass per unit area

J = current density

K = Landau-Ginzburg parameter

ℓ = electronic mean free path

L = longitudinal

λ = penetration depth

Λ = Lame constant

m = magnetization

m_e = rest mass of the electron

M = modulus of elasticity

n = least-squares-fit data count

N = density of vortices

η = acoustic loss factor

ν = Poisson's ratio

p = mass density

P = pressure

ρ = electrical resistivity

q = wave vector

Q = acoustic quality factor

ξ = coherence length

R = resistance

S = stiffness constant

σ = electrical conductivity

TABLE XIII (Continued)

Σ = stress

t = relaxation time

T = transverse

τ = strain

T_c = critical temperature

μ = shear modulus

v = velocity of sound

v_f = Fermi velocity

V = volume

$\bar{w}$ = Burgess vector

ω = angular frequency

x = wavelength

y = theoretical Young's modulus

Y = experimental Young's modulus

Z = acoustic impedance

* = complex quantity

VITA

Gary Wayne Goodrich

Candidate for the Degree of

Doctor of Philosophy

Thesis: LOW FREQUENCY ACOUSTIC INTERACTIONS IN SUPERCONDUCTORS

Major Field: Physics

Biographical:

Personal Data: Born in Dallas, Texas, July 15, 1944, the son of Mr. and Mrs. Hale C. Goodrich; married on August 26, 1967, to Patricia Anne Davison.

Education: Graduated from C. E. Byrd High School, Shreveport, Lousiaina, in May, 1962; attended Centenary College, Shreveport, Louisiana, during the summer of 1962; received the Bachelor of Arts and Bachelor of Science degrees from the University of Texas in Austin, Texas, in 1966 with majors in physics; completed requirements for the Master of Science degree in physics at Oklahoma State University in May, 1968, and the Doctor of Philosophy degree in physics at Oklahoma State University in May, 1971 as a National Science Foundation research assistant; became a member of Signa Pi Sigma, physics honorary fraternity, Phi Kappa Phi, honorary fraternity, and Sigma Xi, honorary research fraternity, while at Oklahoma State University.

Professional Experience: Seismic Technician, Western Geophysical Company of America, Summer 1964; Computer Operator, United Gas Company, Shreveport, Louisiana, Summer 1965; Summer Development Program, Texas Instruments, Incorporated, Summers 1966 and 1967; Graduate Teaching Assistant, Physics Department, Oklahoma State University, 1966-1967; Research Assistant, Physics Department and National Science Foundation, Oklahoma State University, 1967-1970.